Ultrafast Dynamics of Vibrational Polaritons Probed with 2D-IR Spectroscopy

by

Rong Duan

A dissertation submitted in partial fulfillment
of the requirements for the degree of
Doctor of Philosophy
(Chemistry)
in the University of Michigan
2022

Doctoral Committee:

Professor Kevin J, Kubarych, Chair
Professor Hui Deng
Professor Eitan Geva
Professor Jennifer P. Ogilvie

Rong Duan

drong@umich.edu

ORCID iD: 0000-0003-1077-8134

Dedication

To my family

Acknowledgements

"Science is the belief in the ignorance of experts."

-Richard P. Feynman

This thesis could not be done without the guidance and support of many.

First, I would like to express my greatest gratitude to Professor Kevin Kubarych for his dedication, guidance, and support. I will be a lost boat on the ocean of polariton without him served as the lighthouses. Polariton is a new field for me and the group, but I have never felt lonely in my journey of studying it because of his support. He has the greatest enthusiastic and no fear of revealing the physics rules of every interesting system we studied. And that has inspired me along my journey. He has been supportive through all stages of this Ph.D. from brainstorm research ideas to finalize this dissertation.

I would like to acknowledge my committee, Professor Hui Deng, Professor Eitan Geva and Professor Jennifer Ogilvie for providing insights and suggestions. I would like to address my special thanks to Professor Ogilvie. For the most of time I have been working in the joint lab between her and Prof. Kubarych, she provides the warmest kindness and welcomes me as part of her group. I also would like to thank for her guidance especially during the time when I must make decision for my life after graduate school. And I would like to thank both Prof. Ogilvie and Prof. Hui for being great woman scientists I always look up to.

I would like to thank Professor Yin Song and Dr. Joseph Mastron for *ad hoc* mentorship, help, countless conversations, and scientific insights. It has been a great pleasure to work with them. I have learnt a lot of practical skills which become essential for successfully collecting and analyzing data for my research.

I would like to thank both former and current group members, Joseph Meadows, Vivian Crum, Dr. Laura Kiefer, Dr. Kimberly Daley, Dr. Lindsay Michochi, Dr. Ved Roy, and Dr Peter Eckert for their kindness support during this pandemic and invaluable suggestions for this entire time.

I would like to thank all the talented and diligent group members from Ogilvie’s group, Riley, Rhiannon, Ariba, Dr. Stephanie, Hoang, and Dr. Yogita for being responsible and nice coworkers.

I would also like to thank all my peers and friends, with special thanks to Yanbing Zhou, and Zoey Niu who provide me with kindness friendship and selfless support.

Finally, I would like to thank my dad, my mom, my aunt and my grandparents for their encourage, understanding and support. And I would like to thank Haisu Ju for being a significant person and best friend in my life for the past three years. And his unconditional love and encourage helps me through many dark moments in graduate school.

Table of Contents

Dedication ii

Acknowledgements iii

List of Tables viii

List of Figures ix

Abstract xx

Chapter 1 Introduction 1

1.1 Light controlled chemical reaction 1

1.2 Cavity controlled chemistry 2

1.3 Controversy about polariton controlled chemical reaction 6

1.4 Ultrafast spectroscopy’s job 7

1.5 Dissertation outline 8

Chapter 2 Background: Experimental Method: 2D-IR 10

2.1 Basic theory of nonlinear spectroscopy 11

2.1.1 linear spectroscopy 11

2.1.2 Nonlinear spectroscopy 12

2.1.3 Feynman diagrams and nonlinear pathways for a 2-level system 14

2.2 2D-IR 17

2.2.1 2D-IR and its spectroscopy signature 17

2.2.2 Pump-probe geometry apparatus 21

2.2.3 Collinear geometry apparatus 27

2.3 Summary 29

Chapter 3 Vibrational Polariton 30

3.1 Understanding polaritons 30

3.1.1 Basic theory 30

3.1.2 Fabry Perot cavity 34

3.1.3 Dispersion relation of polaritons 36

3.1.4 Dark modes 38

3.1.5 Orientational and spatial coupling 40

3.1.6 Dynamics relaxation 41

Chapter 4 Direct Comparison of Amplitude and Geometric Measures of Spectral Inhomogeneity Using Phase Cycled 2D-IR 43

4.1 Introduction 43

4.2 Experimental methods 48

4.3 Experimental methods 49

4.3.1 Vibrational assignment using DFT, FTIR and 2D-IR for MCMT 49

4.3.2 Using Phase Cycling to Separate Rephasing and Nonrephasing Spectra 50

4.3.3 Comparison of Inhomogeneity index and CLS method without intraband coherence. 52

4.3.4 Comparison of Inhomogeneity Index and CLS methods with intraband coherence 53

4.3.5 Comparison of effect of analysis region on the inhomogeneity index and CLS methods 56

4.4 Conclusions 58

4.5 Supporting information 60

4.5.1 Normalized Linear FTIR Spectrum of MCMT 60

4.5.2 DFT calculation of MCMT in 1-propanol 60

4.5.3 Simulation of FFCF in the Presence and Absence of Intraband Coherence 61

4.5.4 Simulated Inhomogeneity Index with Different Vibrational Anharmonicity 62

4.5.5 Simulated Inhomogeneity Index with Different Integration Regions 63

4.5.6 Fourier Filtering Coherences out of the Inhomogeneity Index 63

4.5.7 Comparison of $W(CO)_6$ in Two Different Solvents 66

Chapter 5 Isolate Polaritonic 2D-IR Transmission Spectra 68

5.1 Introduction 68

5.2 Background correction presented by other people 69

5.3 Isolate pure polariton spectra experimentally 72

5.4 Conclusion 81

5.5 Supporting information 82

5.5.1 Illustration of spatial distribution of polariton eigenmodes 82

5.5.2 Experimental method: 2D-IR spectrometer and cavity fabrication 83

5.5.3 Effect of spectral diffusion on long-time estimate of the uncoupled 2D-IR background 84

5.5.4 Detailed background subtraction process 85

5.5.5 Coherence maps for $\omega_2 = -41$ cm^{-1} 86

5.5.6 Estimate of cavity lifetime 87

5.5.7 Fitting results for several peaks in the 2D spectrum 87

5.5.8 Calculation of molecule numbers in the cavity 88

Chapter 6 Investigation of the dynamics of dual modes polaritons probed with collinear geometry 2D-IR 89

6.1 Introduction 89

6.2 Experimental method 91

6.3 Vibrational assignment 93

6.4 Conclusion 96

Chapter 7 Conclusion and Outlook 97

7.1 General conclusion and outlook 97

Bibliography 100

List of Tables

Table 2-1. Phase cycling scheme to separate rephasing and nonrephasing spectra 25

Table 2-2. Phase cycling scheme to isolate the 2D-IR absorptive signal from unwanted interference 28

Table 4-1. Mode frequency list**:**... 61

Table 5-1. Table for fitting parameters. Waiting time dependent population dynamics of peaks A, D, E, and F (as labeled in Fig. 4) from the as-measured cavity, filtered bare molecule, and residual spectra.. 88

List of Figures

Figure 1-1.Pictures were taken from reference 8 and reference 7. (A) a typical schematic diagram to do OCT with feedbacks (B) use optimal phase control to specifically directional chemical rection to one direction vs the other 2

Figure 1-2.Picture taken from reference 10. Energy diagram representation of VSC................. 3

Figure 1-3. Picture adapted from reference 18. Examples of the hybrid cavity. (a) A schematic of a 0D hybrid cavity with a SWG mirror. (b) Top-view SEM image of a fabricated 0D cavity with a SWG of 5 mm35 mm in size. 0D, zero-dimensional; SEM, scanning electron microscopy; SWG, subwavelength grating 4

Figure 1-4: Few examples to demonstrate VSC change chemistry. (A) from reference 10, by strongly coupled the PNPA hydrolysis reaction's solvent, EtOAc's carbonyl bond with cavity, the reaction rate changed significantly. (B) from reference 20, hydrolysis reaction's kenetic increased by strongly coupled O-H stretch with cavity. (C) From reference 12 strong coupling changed the selectivity of two silyl bonds cleavage reaction 5

Figure 2-1. Feynman Diagram. A generalized Feynman diagram with two solid lines representing the ket (left) and bra (right) sides of the density matrix. Light interacting with the system is represented by the arrows pointing from ket side (+**k**) or from bra side (-**k**). The density matrix will evolve from bottom to top with the respect to time. The G(t) represents the super operator that evaluates the dynamic information. 15

Figure 2-2. Feynman pathways for rephasing and nonrephasing. The left two Feynman diagrams represent rephasing pathways and the right two Feynman diagrams represent two nonrephasing pathways. In the R_1 and R_3 diagrams, the population evolves in ground state and in R_2 and R_4, the population evolves in the first excited state. 16

Figure 2-3. 2D-IR pulse sequence. The first and the third pulse create a superposition (coherence) between states and the second pulse creates a coherence. 17

Figure 2-4. Model 2D-IR spectrum for a simple three level system. The anharmonicity between the first and second excited state can directly access from detection axis difference between ground state bleach (GSB, red) and excited state absorption (ESA, blue) 18

Figure 2-5. When two modes have the same linear spectrum, 2D-IR can help determine if these two modes are coupled with each other (bottom) or not (top) through cross peaks. 19

Figure 2-6: Spectral diffusion's signature in a 2D-IR spectrum. Molecules in different solvent environments will experience different frequencies, which causes absorption linewidth to be broadened inhomogeneously (left). In 2D-IR inhomogeneous linewidth and homogenous linewidth can be distinguished spectrally. The diagonal linewidth is inhomogeneous linewidth and the antidiagonal linewidth is homogeneous linewidth (right). 20

Figure 2-7. coherence map for rephasing pathways 21

Figure 2-8. Different 2D-IR apparatus geometries. From left to right: boxcars geometry, rephasing and nonrephasing will show up at different phase matching positions; pump probe geometry, rephasing and nonrephasing will show up in the same direction traveling along with

$\mathbf{k_3}$; Collinear geometry, the signal travels with the same directions as pump probe geometry but has a different polarization than the pump. 22

Figure 2-9. LUMOS pump-probe geometry set up. 24

Figure 2-10. Set-ups in LUMOS. From Song et. al. showing the different layouts for different color 2D spectroscopy experiments located in LUMOS. 26

Figure 2-11. Essential parts of the collinear set 2D-IR set up. The probe's polarization is rotated by a half wave plate(HWP) from parallel polarization to perpendicular polarization. Two polarizers 27

Figure 3-1. Lorentzian model simulated absorptive and refractive index and transfer matrix way of simulating polariton transmission spectrum 32

Figure 3-2. (A) A Fabry Perot cavity with two examples of confined standing wave modes; decomposition of the incident wave vector into $k_{\perp}$ and $k_{//}$. (B) Transfer matrix simulated transmission and reflection mode in the frequency domain. (C) The dispersion relationship between $k_{//}$ and frequency. 35

Figure 3-3. polariton dispersion curve. When there is zero detuning, the frequency different is called Rabi Splitting. 37

Figure 3-4. polariton energy levels. (A) one molecule mode and one cavity mode coupling will result in two polariton modes. (B)two molecule modes and one cavity mode will result in the same two polariton modes and one cavity mode which has the same frequency as the molecule mode 38

Figure 3-5. Eigenstate distribution of several molecule states coupled with one cavity mode ... 39

Figure 3-6. Taken from reference 75[75]. A demonstration of how coupling rate being affected by spatial distribution of the longitudinal mode. (a) selectively chose PMMA position at Z1-Z5. (b) strong coupling rate depends on mode volume.. 41

Figure 4-1. Methylcyclopentadienyl manganese tricarbonyl (MCMT) structure (A) and the 2D-IR spectrum in 1-propanol solution at t_2 = 0 ps (B). The anharmonicity of each mode is 18 cm^{-1}. 48

Figure 4-2. Methylcyclopentadienyl manganese tricarbonyl (MCMT) 2D-IR spectra at 1 ps waiting time obtained using phase cycling to separate the rephasing and nonrephasing Liouville space pathways. From top to bottom: real part, absolute value; from left to right: rephasing, nonrephasing and absorptive spectra, respectively. Notice that for the real and imaginary columns, red (low temperature color) represents ground state bleaching (GSB) and stimulated emission (SE), and blue (high temperature color) represents excited state absorption (ESA) 51

Figure 4-3.2D-IR spectrum of tungsten hexacarbonyl in 1-propanol at 0.4 ps waiting time (left), and (right) comparison of the FFCF obtained from the CLS versus that found with the II. The two methods yield the same FFCF decay dynamics. The FFCF extracted with the CLS method (arbitrary units) has been scaled to match the normalized FFCF extracted with the II method. .. 52

Figure 4-4. FFCFs for Cp'Mn(CO)$_3$ in 1-propanol obtained using the inhomogeneity index (II) and center line slope (CLS) with integration regions of various sizes for the lower frequency degenerate asymmetrical stretch band. (A) Absolute value of nonrephasing (top) and rephasing (bottom) spectra for the antisymmetric band at t_2 = 1 ps. Different colored boxes indicate the integration regions: 35x61 points (blue), 15x31 points (cyan), and a single point (black). (B) FFCFs for the asymmetrical band with the different integration regions. The y intercept of the calculated FFCF is influenced by the spectral anharmonicity (see discussion in the SI). (C) Absorptive 2D-IR spectra of the asymmetric band at various waiting times with the analyzed peak region indicated (34, 14 and 4 points, corresponding to purple, blue, and cyan). (D) FFCFs calculated from the CLS show the consequence of using differently sized analysis regions. (E) Comparison of FFCF obtained from CLS (blue) and II (red); reducing the coherence contribution in the II with a Fourier filter (see SI) is shown in black. The FFCF extracted with the CLS method (arbitrary units) has been scaled to match the normalized FFCF extracted with the II method.. 53

Figure 4-5. FFCFs for Cp’Mn(CO)$_3$ in 1-propanol obtained using the inhomogeneity index (II) and center line slope(CLS) with integration regions of various sizes for the high frequency symmetrical stretch band. (A) Absolute value of nonrephasing (top) and rephasing (bottom) spectra for the symmetric band at t_2 = 1 ps. Different colored boxes indicate the integration regions: 20x41 points (blue), 10x17 points (cyan), a single point (black). (B) FFCFs for the symmetric stretch band with the different integration regions. In addition to the size of the integration region, the FFCF obtained from the II method is modulated by intraband coherence oscillations. (C) Absorptive 2D-IR spectra of the symmetric band at various waiting times with the analyzed peak region indicated (19, 9 and 5 points, corresponding to purple, blue, and cyan). (D) FFCFs calculated from the CLS of the different analysis regions for the symmetric band. Coherent oscillations contribute to these FFCFs as well. (E) Comparison of FFCFs obtained from CLS (blue) and II(red); reducing the coherence contribution in the II with a Fourier filter (see SI) is shown in black. The FFCF extracted with the CLS method (arbitrary units) has been scaled to match the normalized FFCF extracted with the II method. 54

Figure 4-6. Calculated II and CLS with the response function of a three-level system. Different colors represent different integration box sizes and corresponding norm. FFCF; pink, blue, green represent large, medium and small integration box sizes. The black dashed line represents the FFCF calculated by CLS method. The FFCF traces calculated using different integration box sizes have a different y-intercept but similar decay constants. 55

Figure 4-7. Normalized linear spectrum for MCMT molecule in 1-propanol. Blue curve is the normalized FTIR spectrum and purple curve shows the second derivative spectrum. 60

Figure 4-8. Simulation of 2D spectra and FFCF in the presence and absence of intraband coherence. A) Simulated 2D spectrum with superposed CLS. B) FFCF calculated using II and CLS methods almost perfectly agree in the absence of coherent modulations. C) With modulations arising from intraband coherence, the II and CLS calculated FFCF response differ. The CLS exhibits smaller amplitude modulations, consistent with our experimental findings. .. 61

Figure 4-9. simulated II corresponding with different anharmonicity values 50,100,150,200,250 cm^{-1}. 62

Figure 4-10. Simulated II with different integration sizes compared with CLS 63

Figure 4-11. Full sequence of steps (described in the text) for Fourier filtering the nonrephasing signal in MCMT. We filter the complex amplitude, hence the high-frequency and low-frequency coherences appear at opposite signs due to the difference in the frequency difference in the t_2-dependent field-free Green function propagator. 64

Figure 4-12. Fourier transform of the complex nonrephasing t2-dependent signal amplitude for the two fundamental transition of MCMT. The 2022 cm^{-1} appears with a positive frequency whereas the 1936 cm^{-1} peak appears at a negative frequency (though its amplitude is quite low). 65

Figure 4-13. Comparison between the FFCFs obtained with and without filtering, as well as the two FFCFs obtained from the inhomogeneity index. 66

Figure 4-14. (left) Absorptive 2D-IR spectra of $W(CO)_6$ in butyl acetate and dimethyl formamide. (right) Normalized FFCFs obtained using the CLS and II methods. In the butyl actetate, where the line shape exhibits a particularly simple form, the two FFCFs agree without any scaling. In DMF, like the example of propanol in the main manuscript, there is a more complex shape along the detection axis for the fundamental transition, the FFCF obtained using the CLS needs to be scaled by a factor of more than 3 to overlap the FFCF from the II. 67

Figure 5-1. **(A)** Simulated 2D-IR absorptive response characteristic of sodium nitroprusside (SNP) based on the work of Khalil *et al*. **(B)** Polariton 2D-IR spectrum parameterized using the energy levels reported in Grafton *et al*. Note that the features corresponding to ground state bleach and excited state absorption have signs opposite to those of the absorptive bare molecule response. **(C)** Bare molecule response filtered by the polariton transmission (taken from data in Ref. 38). **(D)** Sum of the filtered background and the polariton response. 71

Figure 5-2. (A) Linear absorbance (red) of 2-mM $W(CO)_6$ in butylacetate in a standard cell, and transmission (green) of 40 mM $W(CO)_6$ in butylacetate in a resonant cavity (mirror reflectivity = 92%). Polariton bands are at 1956 and 1997 cm^{-1}; the bare molecule band is at 1977 cm^{-1}. **(B)** Absorptive 2D-IR spectrum of the cavity response (color) superimposed on the bare molecule response (gray), showing the significant overlap of the v=1 to v=2 excited state absorption and the lower polariton. Linear responses are shown along each axis for reference. **(C)** Absolute value rephasing, nonrephasing and absorptive 2D-IR spectra for the cavity; the signals are obtained using a 6 phase cycling scheme (SI). **(D)** Normalized frequency fluctuation correlation functions (FFCFs) for the LP diagonal (left) and the UP diagonal both indicate coherent modulation due to the nonrephasing contribution. The LP diagonal shows a pronounced spectral inhomogeneity that decays on the same time scale (2.4 ps) as the bare molecule measured outside of a cavity. This apparent spectral diffusion is due to the overlapping uncoupled background 2D-IR response.. 73

Figure 5-3. (A) Absorptive bare molecule 2D-IR obtained using 40 mM $W(CO)_6$ in butylacetate with a 6 μm pathlength cell (uncoated, 3-mm CaF_2 windows). All sets of three 2D spectra are shown for the same three waiting times (0.8, 1.5, and 30 ps). Dynamic changes of the line shape are due to spectral diffusion. **(B)** Absorptive 2D-IR response filtered by the polariton transmission (shown in Fig. 2A). **(C)** Measured absorptive 2D-IR spectra of the full cavity response (40 mM $W(CO)_6$ in butylacetate with a 25 μm pathlength; mirror reflectivity is 92%). **(D)** Background subtracted response (cavity – filtered bare molecule) shows the spectral signatures of the polaritonic ladder expected for an anharmonic oscillator coupled to a single harmonic cavity mode.. 74

Figure 5-4. (A) Measured full cavity response (left), filtered bare molecule (middle), and subtracted residual (cavity – filtered bare molecule) at a waiting time of 0.8 ps. **(B)** Polaritonic ladder deduced from the 30 ps residual spectrum (shown in Fig. 3D, right). Gray arrows indicate transitions involving the uncoupled and dark states (D_1, D_2); bold arrows depict transitions between polariton states (LP, UP, LP_2, MP, and UP_2). **(C)** Waiting time dependence of the two diagonal (peaks C and B) and two main cross peaks (peaks A and D) as indicated in Fig. 4A. Peak A shows essentially negligible contributions from the uncoupled background, whereas the LP diagonal, peak E, shows a pronounced background contribution due to the uncoupled background. For peaks A, B and D, data are shown as moving averages (dark lines) and raw measured data (light lines); window sizes are 10 for peaks A and D, and 3 for peak F. 78

Figure 5-5. (A) Coherence map for the nonrephasing response shown at a frequency cut of +41 cm^{-1}. Because we analyze the complex rephasing spectrum, the coherence for the UP diagonal appears at positive frequency, whereas the LP diagonal appears at –41 cm^{-1} (negative frequency coherence maps are shown in the SI). **(B)** The rephasing coherence map at +41 cm^{-1}, shows the upper left cross peak oscillates (the lower right cross peak oscillates with a frequency of –41 cm^{-1}). **(C)** Full waiting time dependence of the UP diagonal peak for the rephasing (blue) and nonrephasing (red) responses. **(D)** Absolute square Fourier transform amplitude of the rephasing response at the LP/UP cross peak indicates a single peak at 41 cm^{-1}, with a width of roughly 15 cm^{-1}, corresponding to an exponential dephasing of ~3 ps (assuming a Lorentzian spectrum). .. 80

Figure 5-6: Eigenvector distribution of a polariton in a cavity. The blue line shows the squared modulus of the molecular part of the polariton eigenvector (i.e. $|c_j|^2$). Near the mirrors, there is little participation from molecules in both the polariton and dark state eigenvectors. In the regions of higher cavity mode field, there are dark states and the polariton states. 82

Figure 5-7.(A) Transmission spectrum (data extracted from Ref. 56) used to filter the simulated 2D-IR response. **(B)** 2D transmission filter. **(C)** Simulated early waiting time (t_2) absorptive 2D-IR spectrum resembling the results of Khalil et al. for sodium nitroprusside. **(D)** Simulated late waiting time 2D-IR spectrum. **(E)** Filtered early time 2D-IR spectrum. **(F)** Filtered late-time 2D-

IR spectrum. **(G)** Late time, filtered 2D-IR spectrum subtracted from the early-time filtered 2D-IR spectrum. **(H)** Same difference spectrum plotted using the convention where the excitation and detection axes are swapped (for easier comparison with Ref. S5). 84

Figure 5-8. Using the FFCF of the LP to find the weighting parameter. (A) Waiting time dependence of the idealized FFCF of the LP band (yellow) obtained by subtracting the fitted molecule background (red) from normalized cavity LP normalized FFCF (blue). (B) $t_2 = 0$ comparison using the waiting time dependent FFCF from the filtered bare molecule (blue), bare molecule (yellow), and cavity LP (yellow). (C) Shifting the cavity FFCF forward by 300 fs and adding an offset of 0.12 to show that the LP FFCF is correctly timed. (D) Varying the weighting parameter gives a squared, average LP residual after 2 ps that reaches a minimum near 350 (arbitrary units). (E) The LP FFCF obtained by subtracting the weighted bare-molecule spectrum at each waiting time shows the elimination of spectral diffusion. 85

Figure 5-9.Coherence maps (absolute value amplitude) for the rephasing and nonrephasing signals at a coherence frequency of -41 cm^{-1}. 86

Figure 6-1. collinear geometry setup and angle dependent measurement. (A) diagrammed layout for the setup. (B) picture of the real setup (C) demonstration of angle dependent measurement 92

Figure 6-2. linear spectra, transfer matrix way of calculated dispersion curve and polariton demo. (A)(B)linear spectra at angle 1,2. red: probe transmission of the polariton; blue: polariton linear transmission spectrum calculated by using transfer matrix; (C) sample; (D) calculated dispersion curve using transfer matrix 93

Figure 6-3. dynamic information for UP region of polariton 1. (A)2D spectrum of the polariton of angle 1 at 10ps (B) 2D spectrum of the polariton of angle 2 at 10ps (C)LP1UP1 cross peak dynamics. (D)UP1UP1 cross peak dynamics 94

Figure 6-4. Energy ladder until the second manifold for angle 1(left) and angle 2(right). The grey line is for dark states. 95

Abstract

Polaritonic chemistry—controlling chemical reactions by strongly coupling light modes with resonant reactant vibrational transitions—is a rapidly developing field. This fundamentally new approach to modifying chemical reaction rates and product yields promises to enable direct manipulation of chemical free energy surfaces, remotely controlled by external optical cavities. The strongly-coupled light-matter hybrid is referred to as “vibrational polaritons,” and understanding the mechanisms of this new type of chemical control method will be essential in defining the scope of manipulation available to develop of new reactions or discover novel materials for quantum information processing. Two-dimensional infrared (2D-IR) spectroscopy is a powerful tool to access vibrational structural dynamics, including population transfer and relaxation, as well as frequency fluctuations, and is thus ideally suited to the study of vibrational strong coupling systems. This dissertation focuses on how to use 2D-IR to understand basic polariton energy level structure and the time-dependent processes that occur following ultrafast excitation of light-matter hybrid polaritons.

The use of a pulse shaper based 2D-IR apparatus has many advantages over alternative methods of implementing 2D-IR. Using a phase-cycling approach, it is demonstrated here that both “geometric” and “amplitude” based methods to obtain vibrational spectral diffusion dynamics are effectively equivalent. Both methods are applied to various organometallic complexes which serve as useful dynamical probes of solvation. The two analysis methods are essentially identical but manifest coherent, inherently non-equilibriium dynamics differently.

One of the challenges in obtaining the polariton response using 2D-IR is a persistent bare molecule (i.e. non-polaritonic) background contribution. In real-world planar Fabry-Pérot cavities, not all of the molecules are coupled with the cavity, and due to the small vacuum Rabi

splitting separating the lower and upper polariton states, there is an unavoidable 2D-IR signal due to the bare molecules. This background obfuscates the energy level assignment and dynamical information readout of the polaritons. This dissertation first demonstrates that this background contribution, which is present in most 2D-IR spectra published in the literature, is due to the uncoupled 2D-IR spectrum, and second, provides a means of suppressing the background by subtracting it from the measured cavity spectra.

The nature of the hybrid polaritonic states is altered by changing the frequency of the cavity, which can be done either by modifying the length or by adjusting the angle of the incident light beam used for spectroscopy. Most of the ultrafast IR experiments done previously are based on probing the zero-detuning polariton level pairs. However, the contribution of different parts of energy dispersion is also worth investigating. To be able to use the angle-tuning approach with 2D-IR spectroscopy, it is possible to implement a fully collinear geometry to avoid complications from non-collinear beam geometries while changing the angle of cavity relative to the incoming beams. As an illustration of the benefits of using a fully-collinear geometry, an example is presented where two different vibrational modes are coupled to two different modes of the same optical cavity. These so-called dual-mode polaritons exhibit cavity-detuning-dependent relaxation dynamics.

Chapter 1 Introduction

1.1 Light controlled chemical reaction

Chemical reactions are at the core of chemical and biological processes. Activation barriers largely determine the rates and free energy differences give equilibrium constants and yields. There are some commonly used macroscopic techniques to predict and control chemical reactions that can be categorized into either controlling its kinetic energy or its potential energy. Some commonly used methods include adding a catalyst to lower the activation energy, changing the solvent system to modify solvent and solute interaction, and alternating the temperature and concentration to increase or decrease the probability of collision. Over the past several decades, the development of lasers has introduced a new hope of achieving reaction selectivity by using a light to selectively break and form new chemical bonds.

There have been multiple attempts at using lasers to selectively guide reaction outcomes. One of them was to use a monochromatic laser which has the same frequency as specific chemical bond's local mode frequency to selectively break a bond[1]. While this seems like a straightforward approach, intramolecular vibrational energy redistribution (IVR)[2] at room temperature, a process for energy distribution among different coupled molecular vibrational modes, is much faster than the bond breaking time scale, and so IVR occurs before the energy can be used for breaking the bond. The more coupled vibrational modes inside a system, the more severe the IVR effects this method. When the selectivity is lost, using a laser is the identical to using a thermal source. Chemical reactions under cryogenic temperatures can help to reduce the effect of IVR but this is not practical to generalize to all chemical reactions.

Another method that was proposed to control reaction pathways is called optimal control theory (OCT)[3-5]. This theory was evolved from pump-dump excitation method[6] and predicts that the reaction's selective final state will be reached by carefully applying a shaped laser pulse which has an optimal amplitude and phase. The electric field of the optimal laser pulse is iteratively calculated using Schrödinger's equation. One of the example shows in **Figure 1-1B** is using OCT change the relative yield of excited Br* for the process: I + Br* ⟵ IBr ⟶ I + Br[7].

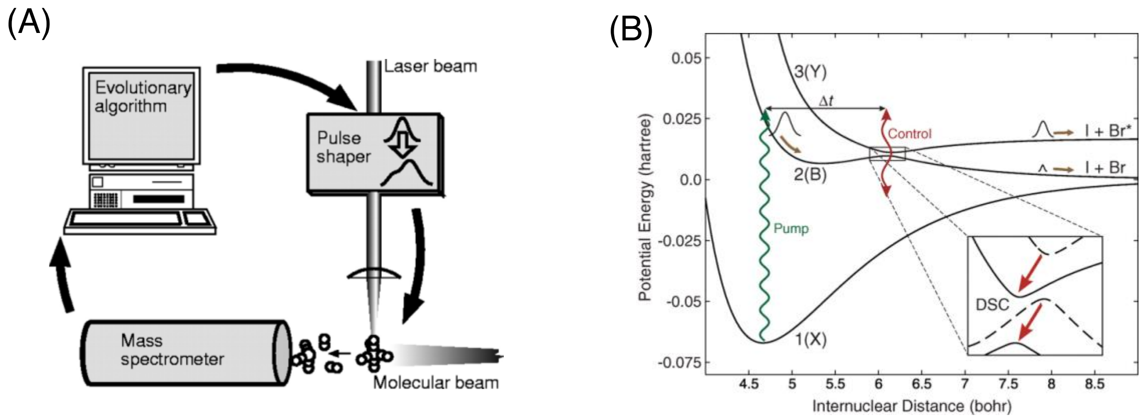

Figure 1-1. Pictures were taken from reference 8 and reference 7. (A) a typical schematic diagram to do OCT with feedbacks (B) use optimal phase control to specifically directional chemical rection to one direction vs the other

OCT proved successful for atomic and small molecular systems but fails for large molecular systems due to the lack of accuracy of the potential energy surface feedback. The improved version of OCT generates a 'perfect' shaped pulse by requiring feedback from the experiment signal to train the pulse shape by a genetic algorithm[8] (**Figure 1-1A**). Unfortunately, this method also suffers from the energy dissipated via IVR, and worse, is limited by extremely fast decoherence which randomizes the phase of the evolving wavepacket.

1.2 Cavity controlled chemistry

Recent work by Ebbesen and others have shown a new way to control a chemical reaction's reactivity and selectivity at room temperature, by using vibrational strong coupling (VSC)[9-14]. The most common way is to strongly couple light cavity modes with one or more reactant molecule's vibrational modes which are associated with bond breaking. This strong coupling results in a quasiparticle system that shares certain properties of both light and matter. This quasiparticle system is called a vibrational polariton. A detailed discussion about vibrational polariton can be found in chapter 3.

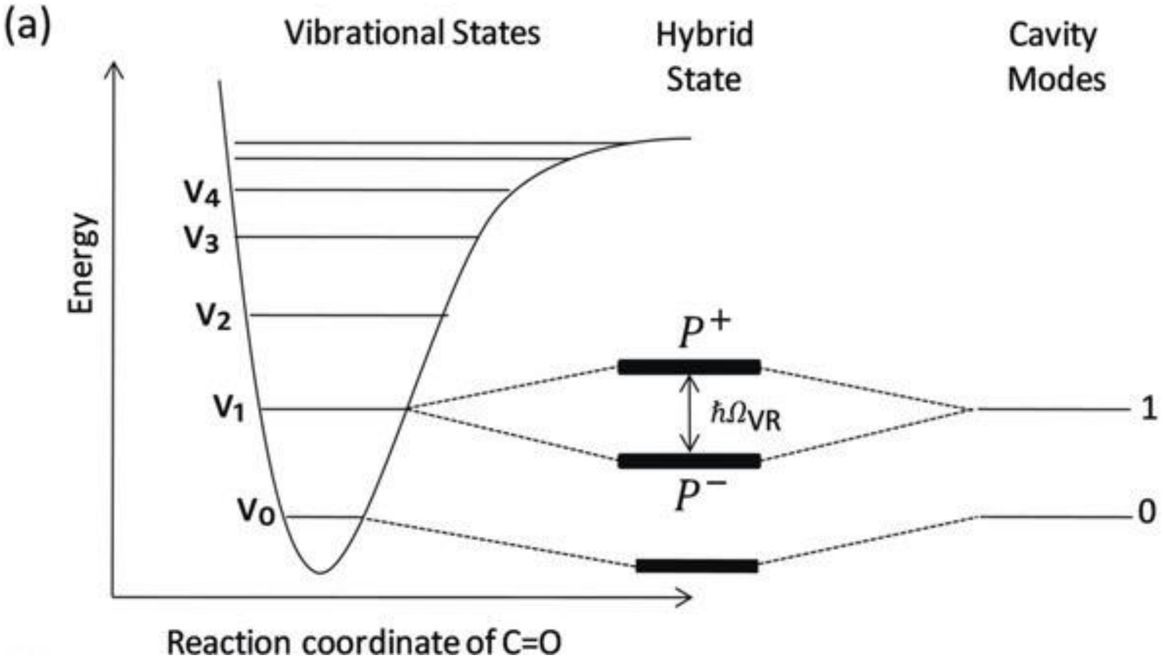

Figure 1-2.Picture taken from reference 10. Energy diagram representation of VSC

Polaritons are nothing new in physics; researchers have successfully achieved strong coupling using a single Rydberg atom and cavity under extreme conditions many years ago[15, 16]. Using collective quantum wells and high reflective dielectric-based distributed Bragg reflectors, one can achieve strong coupling at room temperature in a microcavity[12, 17, 18]. Because strong coupling is composed of a mixture of particle and light properties, there are some new fascinating characteristics that arise, including adopted light properties such as low effective mass, bosonic statistics and dispersion. This area of research is still active, with the hope that one can use a polariton system to achieve ambient temperature Boson Einstein condensate lasers[19].

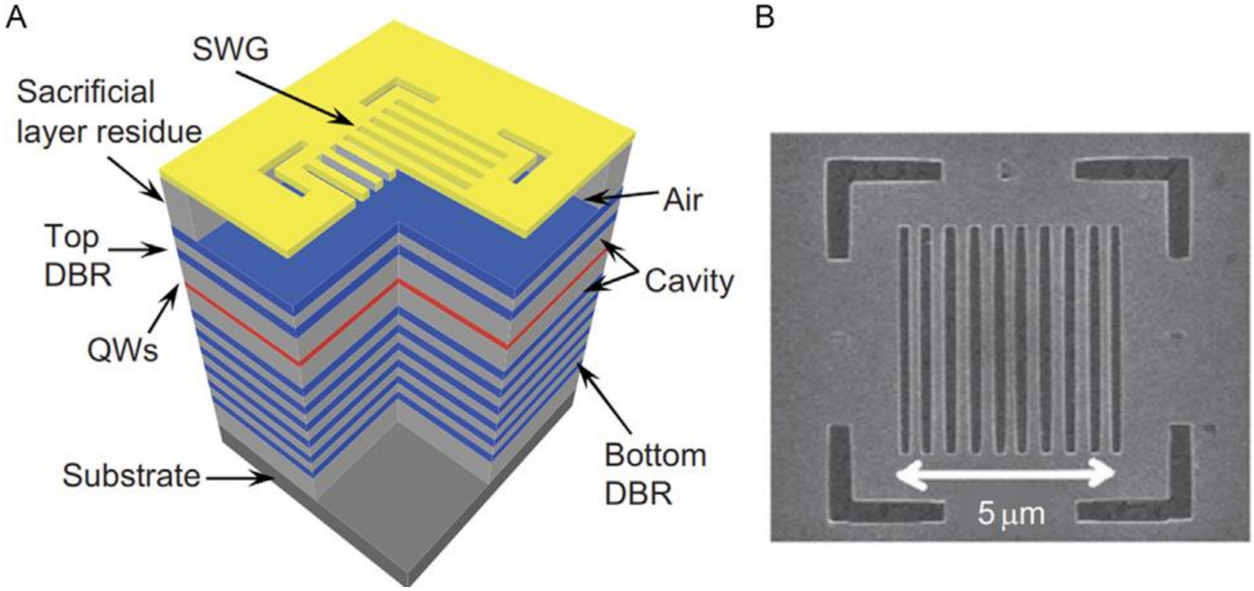

Figure 1-3. Picture adapted from reference 18. Examples of the hybrid cavity. (a) A schematic of a 0D hybrid cavity with a SWG mirror. (b) Top-view SEM image of a fabricated 0D cavity with a SWG of 5 mm35 mm in size. 0D, zero-dimensional; SEM, scanning electron microscopy; SWG, subwavelength grating

Chemists have focused on understanding how the properties of polaritons alter chemical reactions and dynamics, recently showing by VSC, that electron transfer reactions can either be enhanced[20, 21] or suppressed[22-24]. Because a single vibrational mode on one molecule has a low oscillator strength, VSC is usually achieved by collectively coupling an ensemble of molecule modes to the cavity. In practice, this collectivity requires high concentrations, in the 10s to 100s of millimolar (mM) range, which can be quite a bit higher than, for example, one would use with a catalyst. One of the examples is demonstrated by Hiura[20] to use VSC to alter the kinetics for hydrolysis experiment (**Figure 1-4B**). By coupling with H-O stretch mode of water, they were able to significantly achieve enhance of this chemical reaction rate.

Another aim of current research is to generate strong coupling using standard reactant concentrations. This is accomplished by coupling the cavity mode with a vibrational mode of the reaction solvent that has a similar frequency as the reactant's vibrational mode to tilt the reaction kinetics. This allows concentration of the chemical reaction to remain unchanged but the 'unnecessary' reaction part, the solvent, has a high concentration and is strongly coupled with the cavity. One such experiments demonstrated by the Ebbesen group shows that by coupling the cavity to the solvent's (ethyl acetate) C=O mode, the hydrolysis of PNPA's reaction rate increases by more than one order of magnitude (**Figure 1-4A**)[10].

Having demonstrated the ability to change the rate of certain reactions using VSC, some experiments have also been reported that claim to change the selectivity of one chemical reaction under strong coupling. One exemplary example is also from Ebbesen's group (**Figure 1-4C**). They used a silane derivative reactant which can undergo two silyl bonds cleavage reactions[14]. By

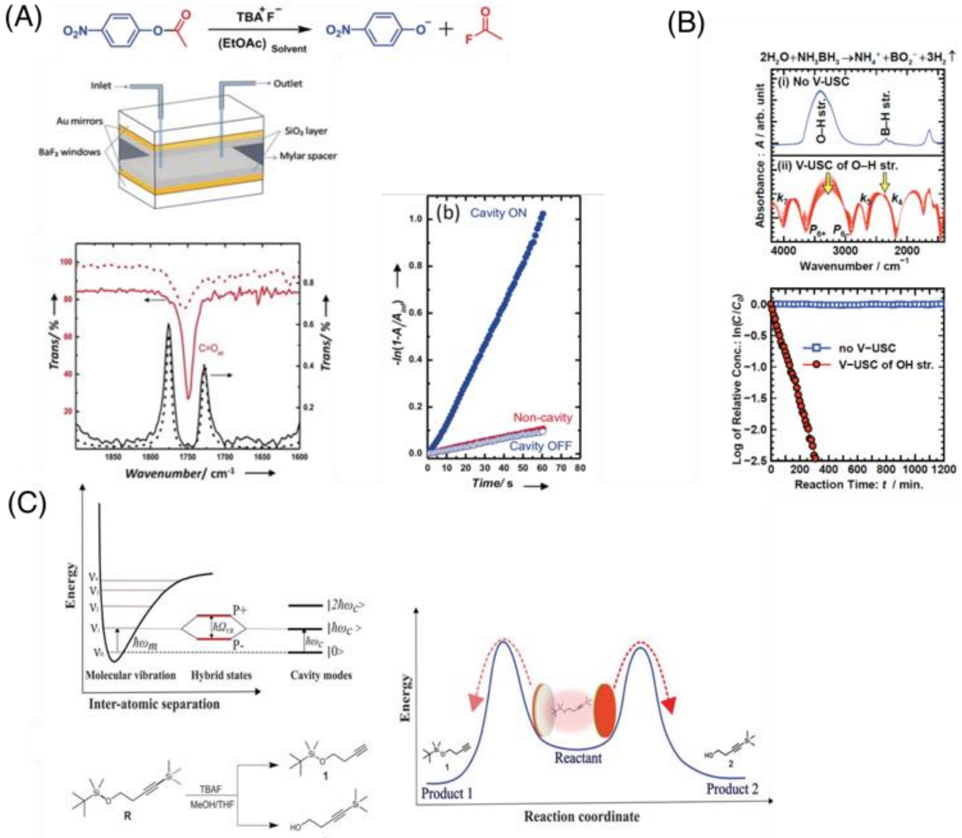

Figure 1-4: Few examples to demonstrate VSC change chemistry. (A) from reference 10, by strongly coupled the PNPA hydrolysis reaction's solvent, EtOAc's carbonyl bond with cavity, the reaction rate changed significantly. (B) from reference 20, hydrolysis reaction's kenetic increased by strongly coupled O-H stretch with cavity. (C) From reference 12 strong coupling changed the selectivity of two silyl bonds cleavage reaction

coupling with different vibrational modes of the silane derivative (Si-O, Si-C, Si-CH_3), the chemical reaction's kinetics can be slowed down differently, thus altering the product distribution under what would typically be called "kinetic control."

1.3 Controversy about polariton controlled chemical reaction

Despite the potentially enormous breakthrough of using VSC to selectively steer reactions towards desired products, there has been some debate regarding reproducibility. For example, Giebink's group recently reported a failure in an attempt to repeat Hiura's cyanate ion hydrolysis strong coupling experiment[25]. And recently, Xiong's group reported another failure to repeating Ebbesen's PNPA hydrolysis reaction[26]. These failed attempts may result from some important experimental factors not being reported. Theoreticians have been working on understanding the mechanism behind VSC controlled chemical reaction, and there are many questions if strong coupling is necessary for, or even capable of, modify chemical reactions. From the theory perspective, there is no strong evidence showing that the reaction barrier has been modified by VSC[27, 28]. There are also a theory suggests the upper polariton (UP) can provide a 'free' energy boost[13] because of it having a higher energy than the vibration mode of its origin. Many theoreticians attempt to use different theories to explain why strong coupling can modify chemical reactions[28-30], but until now, no universal comprehensive explanation exists as of now.

In addition, even the simple properties of a VSC system need demand significant efforts to characterize. In solid state polariton systems, a quantum well can be placed at a certain location[31-34] , can have a certain transition dipole orientation along x-y direction, and because its periodic structure, there are sub-bands in momentum space ($k_{//}$ dependent) that can couple with the cavity's modes. While vibrational polaritons are typically implemented in the liquid phase (or randomly in a film), the coupling rate is more complex and can be determined by many other factors such as orientational and the spatial distribution.

1.4 Ultrafast spectroscopy's job

In general, the rate constant change is used as an important way to characterize the effectiveness of the strong coupling for chemical reaction. Indeed, rate constant is an important and straightforward measurement to describe a change of chemical reaction. But unfortunately, rate constant only provides insights of average information. There are many important microscopic dynamic factors that can contribute to this parameter, including how collisions happen between molecules, how molecules exchange energy with the environment, and how the chemical bonds break and form. Answering those questions would provide more detailed information towards understanding how VSC changes a chemical reaction, and luckily, ultrafast spectroscopy can provide such insight. Not only are the light pulses used to do the measurements on fs or ps time scales, which match the time scales as the microscopic movements, but also important dipole-dipole interaction dynamic information can be deduced by measuring the nonlinear response function. Even though not all chemical reaction can be studied using ultrafast spectroscopy, a model system could provide insights in terms of understanding how strong coupling plays the role in alternating chemical reaction. So, most of the work in this dissertation is focused on using ultrafast spectroscopy to correctly understand dynamic information of vibrational polariton with the hope to tackle the mechanisms behind selectivity and reactivity of VSC controlled chemical reactions. Chapter 2 will cover a detailed description on multidimension spectroscopy in general.

Initial attempts to understand the ultrafast dynamics have been made using pump-probe and 2D-IR spectroscopies, mostly reporting on the population dynamics investigation using a vibrational polariton toy model, a metal carbonyl compound with one or several degenerate vibrational modes coupled with a mode from a Fabry Perot cavity. The typical choice is Tungsten hexacarbonyl[35, 36 37]and nitroprusside[38]. Their 2D spectra in general shared the same features; They have also investigated the relaxation dynamics of polariton modes and found that two components contribute to the relaxation dynamics, the faster component is the light cavity decay, and the slower decay is the reservoir decay which is consist with the previous fundings from QW polaritons[39]. They have also find evidence of polariton to reservoir energy transfer[35]. Another interesting demonstration shows that by coupling to the same cavity mode, intermolecular transfer can be turned on for the previous uncoupled modes[37].

However, as a relatively new system to be studied by ultrafast spectroscopy, there are some open fundamental questions about the experiment itself. Specifically, what does 2D-IR spectra measure, a mixture or just polariton? Why does the polariton spectrum shape look odd compared with other normal systems? Can multidimensional spectroscopy be treated perturbatively in general? What is the contribution of other $k_{//}$ other than when only measuring the polariton when detuning is zero? And most importantly, how does VSC contribute change in the chemical dynamics? This thesis will focus on addressing and answering some of these pertinent questions.

1.5 Dissertation outline

This dissertation first discusses the fundamentals of the experimental method, 2D-IR, this spectroscopy method is used for the vibrational polariton studies in the rest of this dissertation. That Chapter starts from a comparison with linear spectroscopy and some theoretical explanations to describe why multidimensional spectroscopy is necessary to understand dynamical information. Some basic and important spectral and dynamic features and observables that result from a typical

2D-IR experiment is introduced. Finally, two different 2D-IR experimental apparatus implemented to understand different polariton features are described in detail.

Chapter 3 will focus on reviewing basic knowledge of polaritons, including their origin and signature properties. Next is a discussion of the theoretical background of polariton systems and some important light properties that get adopted by polariton system including dispersion relationship. Finally, there is a discussion about dark states, spatial and orientational coupling.

Chapter 4 will provide a direct comparison of using geometric and amplitude way to extract spectra diffusion for two group of molecules. $W(CO)_6$ represents the simplest case, a highly symmetric system with 3 degenerate IR modes and MCMT represents a system that can have fast IVR across different modes. This will set the ground for using amplitude method to extract polariton spectra diffusion information.

Chapter 5 will present on using polariton only nature to help correct polariton 2D spectra from bare molecule background; including the correction method and the discuss about necessity about background correction.

Chapter 6 will focus on using collinear geometry 2DIR set up to understand different parts of energy dispersion of a dual mode polariton.

Chapter 2 Background: Experimental Method: 2D-IR

Though widely used in a broad range of chemical contexts, linear optical absorption spectroscopy has numerous limitations related to the inherent averaging and lack of direct access to dynamics, interactions and structure. Nonlinear spectroscopy can provide avenues to circumvent these limitations, but there is a signficant added degree of complexity, which has limited the wide adoption of ultrafast, nonlinear methods, especially multidimensional methods.

There are many different nonlinear spectroscopy techniques avalable to advance our understanding of dynamical phenomena in chemistry. One major category focuses on understanding molecular dynamics includes transient absorption (TA), transient grating, pump-probe and multidimensional spectroscopy. 2D-IR has assumed a prominent role among multidimensional approaches due to the chemically intuitive information available by virtue of measuring the third-order response function. Fourier transforming the detected signal produced when the delay between the two ultrafast pump pulses are scanned introduces a new excitation frequency axis which enables straightforward anaylsis of the decay of frequency correlations as well as energy transfer beween vibrational modes. Two-dimensional lineshapes make it possible to separate homogenous and inhomognous linewidths qualitatively and quantitatively.

This chapter will primarily discuss the theory behind 2D-IR, the principle spectral signatures, and the optical experimental apparatus. Understanding the theory behind linear and nonlinear spectroscopy is essential to understand the benefits as well as some limitations in using 2D-IR to understand vibrational polariton dynamics. There are some useful tools throughout the process including the time evolution of the density matrix, perturbation theory, light-matter interactions, etc., which can all be found in other well-written literatures and books[40-45]. Nevertheless, the salient aspects that we specifically rely upon are summarized here.

2.1 Basic theory of nonlinear spectroscopy

2.1.1 linear spectroscopy

The interaction between light and matter resuts in an induced polarization which can be described by a response function that is linear in the appllied electric field. The applied field polarizes the material and induces a dipole moment. Based on Maxwell's equations, the dipole moment is a source for the electric field radiation. In the time domain, the output polarization, P, is the result of the convolution between the molecular response function and the light input:

$$P^{(1)}\ (t) = \int_{-\infty}^{\infty} R^{(1)}(t-\tau)E(\tau)d\tau \tag{2.1}$$

In this equation, $P^{(1)}(t)$ is the linear polarization, $R^{(1)}(t)$ is the first order response function of the material and $E(t)$ is the input electric field. The linear response function has the property of causality, which means no output can occur before the interaction with light, and it only depends on the time difference, $t-\tau$. This causality results in the well-known Kramers-Kronig relation. There are several ways to calculate the first order response function of a material, such as the classical Lorentz oscillator model, or quantum mechanical perturbation theory. The total Hamiltonian can be separated into two parts, system and the weak interaction between system and the light, in which the μ_I is the interaction dipole moment operator.

$$\hat{H} = \hat{H}_0 + \hat{H}_I = \ \hat{H}_0 - \mu_I E \tag{2.2}$$

The linear response function can be derived by solving the quantum Liouville equation:

$$R^{(1)}(t) = \frac{i}{\hbar} Tr\big([\mu_I(t), \mu_I(0)]\rho_{eq}\big) \tag{2.3}$$

Here, ρ_{eq} is the 0th order expansion of the density operator, which is also the equilibrium Boltzmann distribution of the initial state. The induced polarization can be extracted from the linear spectrum, but that information cannot be used to go backwards to determine the dipole-dipole correlation, or, within the Kubo model, the frequency fluctuation correlation function. That is the principal limitation that motivates the development of nonlinear spectroscopy, to understand the dynamical information of the system that is buried in the 1D lineshape.

2.1.2 Nonlinear spectroscopy

In general, the light field intensity does not have to be high to induce the polarization in the linear regime, but this is not necessarily true in nonlinear spectroscopy. In nonlinear spectroscopy, to be able to drive a nonlinear response, it often requires relatively high intensity light (but still within the perturbative regime) to interact with the system more than once at different time delays or several light fields that are physically separated into different time delays.

The polarization can be expanded into a power series:

$$P(t) = P^{(1)}(t) + P^{(2)}(t) + P^{(3)}(t) + \cdots \tag{2.4}$$

Since 2D-IR is a third order nonlinear process, this chapter will only focus on the third order induced polarization. Generally, the third order polarization can be represented as:

$$P^{(3)}(t) = \int_0^\infty d\tau_3 \int_0^\infty d\tau_2 \int_0^\infty d\tau_1 R^3(t-\tau_1, t-\tau_2, t-\tau_3) E(\tau_1) E(\tau_2) E(\tau_3) \tag{2.5}$$

Classically, the above relationship can be derived from using an anharmonic oscillator model to describe the nonlinear response, the additional term ηx^2 is introduced to represent the nonlinearity[46]:

$$m(\ddot{x} + \gamma \dot{x} + \omega_0^2 x + \eta x^2) = -eE(t) \tag{2.6}$$

This model is analogous to the basic physics needed to understand the nonlinear optical processes that we use frequently to generate mid-IR light from an 800 nm Ti:sapphire laser, but for the purposes of understanding molecular spectroscopy, the molecule's response function essentially charts the evolution of the molecule's density matrix, in which the diagonal elements represent populations while the off-diagonal elements represents coherences. The induced polarization P(t) can be described in terms of the expectation value of the dipole operator:

$$P(t) = Tr\big(\mu_I(t)\rho_I(t)\big) \tag{2.7}$$
$$= Tr\left(\mu_I(t)\rho_I^{(0)}(t)\right) + Tr\left(\mu_I(t)\rho_I^{(1)}(t)\right) + Tr\left(\mu_I(t)\rho_I^{(2)}(t)\right) + Tr\left(\mu_I(t)\rho_I^{(3)}(t)\right) \ldots$$

The $\rho_I(t)$ is the interaction picture density operator, and the *n*th order of its expansion term is represented as $\rho_I^{(n)}(t)$. So, the induced third order polarization can be described using a power expansion of the density matrix.

$$P^{(3)}\,(t) \propto \int_0^\infty d\tau_3 \int_0^\infty d\tau_2 \int_0^\infty d\tau_1 E(\tau_1)E(\tau_2)E(\tau_3) Tr([[[\mu_I(t-\tau_1-\tau_2 - \tau_3), \mu_I(t-\tau_1-\tau_2)], \mu_I(t-\tau_1)], \mu_I(0)]\rho_{eq}) \tag{2.8}$$

In which, the third order response function is:

$$R^{(3)}(t) \propto Tr([[[\mu_I(t-\tau_1-\tau_2-\tau_3), \mu_I(t-\tau_1-\tau_2)], \mu_I(t-\tau_1)], \mu_I(0)]\rho_{eq} \tag{2.9}$$

The third order response function has the same causality and time invariance properties as the linear response function. Mathematically, the causality and time invariance are enforced by the commutation product between the density operator and dipole operator.

After expanding the commutators and invoking the time invariant features of the response function, there will be four independent terms that represent the sequential dipole-dipole interactions. In subsection 2.1.3 we will see that we need different phase matching conditions to separately extract information from the various contributions to the response function.

$$R^{(3)}(\tau_1,\tau_2,\tau_3) \propto \sum_{\alpha=1}^{4}[R_\alpha(\tau_3,\tau_2,\tau_1) - R_\alpha^*(\tau_3,\tau_2,\tau_1)] \tag{2.10}$$

$$R_1 = < \mu_I(\tau_1)\mu_I(\tau_1+\tau_2)\mu_I(\tau_1+\tau_2+\tau_3)\mu_I(0)\rho_0 >$$

$$R_2 = < \mu_I(0)\mu_I(\tau_1+\tau_2)\mu_I(\tau_1+\tau_2+\tau_3)\mu_I(\tau_1)\rho_0 >$$

$$R_3 = < \mu_I(0)\mu_I(\tau_1)\mu_I(\tau_1+\tau_2+\tau_3)\mu_I(\tau_1+\tau_2)\rho_0 >$$

$$R_4 = < \mu_I(\tau_1+\tau_2+\tau_3)\mu_I(\tau_1+\tau_2)\mu_I(\tau_1)\mu_I(0)\rho_0 >$$

2.1.3 Feynman diagrams and nonlinear pathways for a 2-level system

Thus far, we have only described a general third order response. Experimentally, three sequential light pulses induce these third order polarizations, so the light electric field polarization, and phase, will be central to influencing the signal's polarization and phase.

In general, the light's electric field in the time domain can be represented as:

$$E(r,t) = E_o(t)e^{i(-\omega t + k\cdot r + \phi)} \tag{2.11}$$

in which the ω is the frequency of the field, **k** is the wave vector and ϕ is the additional phase.

Double-sided Feynman diagrams are useful for characterizing how different wavevectors modify system eigenstates in different excitation pathways. Feynman diagrams have several essential parts that need to be introduced (Fig.1). The two vertical lines represent the ket (left) and bra (right) side of the density operator. Going from the bottom to the top represents the time evolution direction. Arrows that point to the right represents the light waves with positive **k** vector and the opposite direction represents its complex conjugate, having a negative **k** vector. Incoming arrows represent absorption while outgoing arrows represents emission. **G(t)** represents the Green's function that evolves the system under the influence of the system Hamiltonian with a phenomenological damping factor (defined below):

$$G(t)\rho_{ij} = e^{-i\omega_{ij}\tau-\Gamma_{ij}\tau}\rho_{ij} \tag{2.12}$$

In which ω_{ij} is the frequency difference between the two states i and j and Γ_{ij} is the damping factor while propagating; when $i = j$, $1/\Gamma_{ii}$ represents the population relaxation rate and $1/\Gamma_{ij}$ is the dephasing rate for the coherence when $i \neq j$.

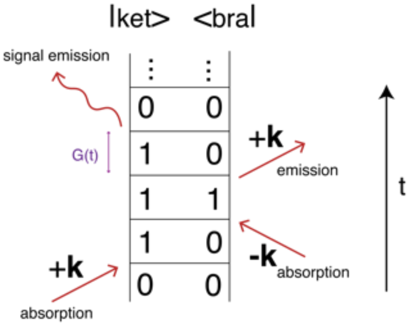

Figure 2-1. Feynman Diagram. A generalized Feynman diagram with two solid lines representing the ket (left) and bra (right) sides of the density matrix. Light interacting with the system is represented by the arrows pointing from ket side (+**k**) or from bra side (-**k**). The density matrix will evolve from bottom to top with the respect to time. The G(t) represents the super operator that evaluates the dynamic information.

There are $2^3 = 8$ different phase matching conditions that can contribute to the third order signal because there are three field interactions (at third order in perturbation theory). For 2D-IR, there are typically recorded two phase matching conditions, referred to as rephasing ($-\mathbf{k}_1+\mathbf{k}_2+\mathbf{k}_3$) and nonrephasing ($\mathbf{k}_1-\mathbf{k}_2+\mathbf{k}_3$). The name rephasing comes from the fact that with this wave vector sequence, the phase acquired in τ_1 is reversed in τ_3 due to the frequency reversal. And the nonrephasing signal evolves with the same frequency in the two coherence periods. The rephasing pathway's 'echo' contains the inhomogeneous linewidth broadening information while the nonrephasing data give access to that pathway. Hence, the difference between the two is a direct readout of the spectral inhomogeneity in the system as a function of time. **Figure 2-2** shows the typical pathways for both rephasing and nonrephasing for a two level system:

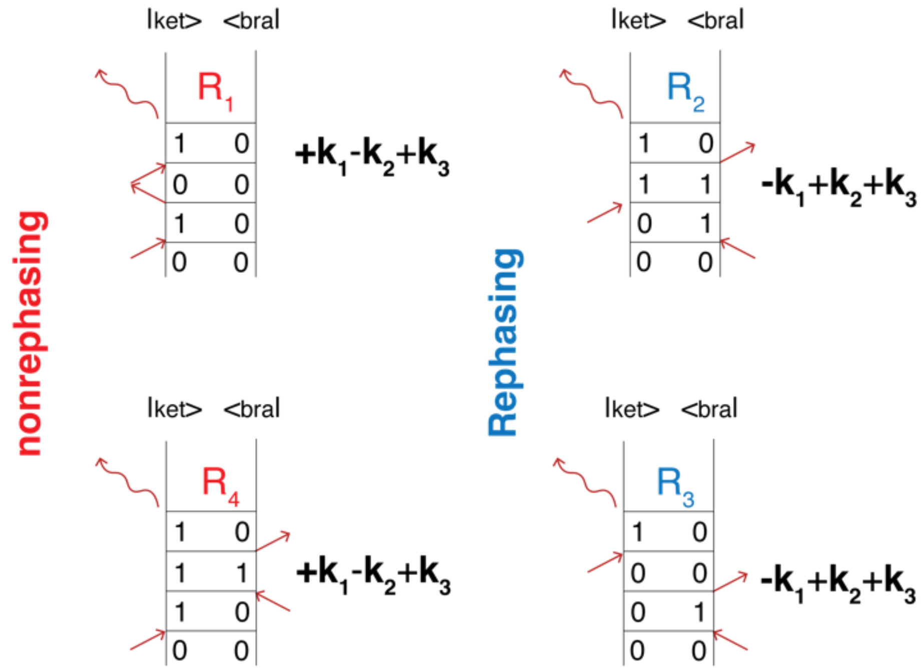

Figure 2-2. Feynman pathways for rephasing and nonrephasing. The left two Feynman diagrams represent rephasing pathways and the right two Feynman diagrams represent two nonrephasing pathways. In the R_1 and R_3 diagrams, the population evolves in ground state and in R_2 and R_4, the population evolves in the first excited state.

By considering the dynamic evolution, for each interaction, the four third-order response functions can be rewrite in terms of the oscillation frequency ω, decay rate Γ and dipole moment μ:

$$
\begin{aligned}
R_1 &\propto \mu_{01}^4 e^{-i\omega_{01}\tau_1} e^{-\Gamma_{01}\tau_1} e^{-\tau_2\Gamma_{00}} e^{-i\omega_{01}\tau_3} e^{-\tau_3\Gamma_{01}} \\
R_2 &\propto \mu_{01}^4 e^{+i\omega_{01}\tau_1} e^{-\Gamma_{01}\tau_1} e^{-\tau_2\Gamma_{11}} e^{-i\omega_{01}\tau_3} e^{-\tau_3\Gamma_{01}} \\
R_3 &\propto \mu_{01}^4 e^{+i\omega_{01}\tau_1} e^{-\Gamma_{01}\tau_1} e^{-\tau_2\Gamma_{00}} e^{-i\omega_{01}\tau_3} e^{-\tau_3\Gamma_{01}} \\
R_4 &\propto \mu_{01}^4 e^{-i\omega_{01}\tau_1} e^{-\Gamma_{01}\tau_1} e^{-\tau_2\Gamma_{11}} e^{-i\omega_{01}\tau_3} e^{-\tau_3\Gamma_{01}}
\end{aligned}
\qquad (2.13)
$$

2.2 2D-IR

The rest of this chapter will focus on 2D-IR spectroscopy in a ground state three level system.

2.2.1 2D-IR and its spectroscopy signature

Figure 2-3 shows a pulse sequence in the time domain (without any spatial distribution). The first pulse creates a coherence between the ground and the first excited state with frequency ω_{01}, the second pulse creates a population at the first excited state (or ground state) with dephasing rate Γ_{11} or Γ_{00} along the second waiting time τ_2, the third pulse creates another coherent state after interacting with the system, and finally, the signal will emit afterwards at a time delay τ_3.

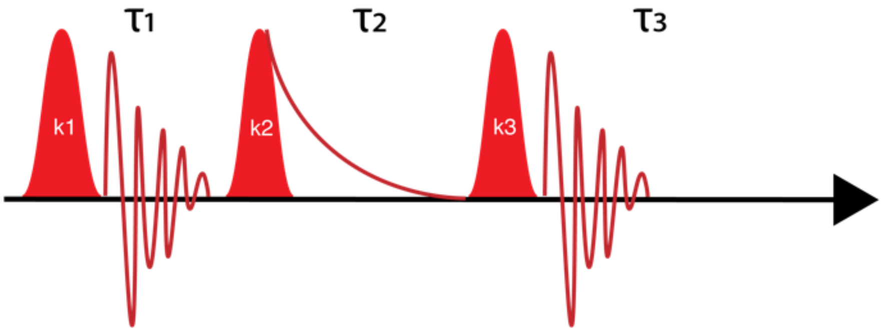

Figure 2-3. 2D-IR pulse sequence. The first and the third pulse create a superposition (coherence) between states and the second pulse creates a coherence.

Usually, one 2D spectrum is an amplitude map of information from two coherence periods τ_1 and τ_3 in frequency domain (**Figure 2-4**). The first frequency axis, usually called excitation axis, can be generated from Fourier transform τ_1, and the detection axis can be directly obtaining from spectrometer. And the 2D experiment is the combination of 2D spectra at a series of different τ_2.

The most commonly referred benefits of using 2D-IR to access third order nonlinear response functions can be summarized into direct access to anharmonicity, direct access to coupling among multiple vibrational modes, and direct access to different line broadening mechanisms. Also, vibrational energy redistribution and vibrational relaxation can be retrieved by analyzing the diagonal and off diagonal peak's amplitude changing as a function of delay τ_2.

Figure 2-4 shows that how the 2D spectrum looks like with a simple three level system; After the system excited using the two excitation pulses, the probe pulse can either create a ground state bleach (red) or an excited state absorption (blue). The frequency different between these two states along the detection axis is a straightforward signature for anharmonicity between the first and the second excited state. The peak at the diagonal resembles the linear spectum. The feature has been used in the polariton analysis to determine the energy ladder.

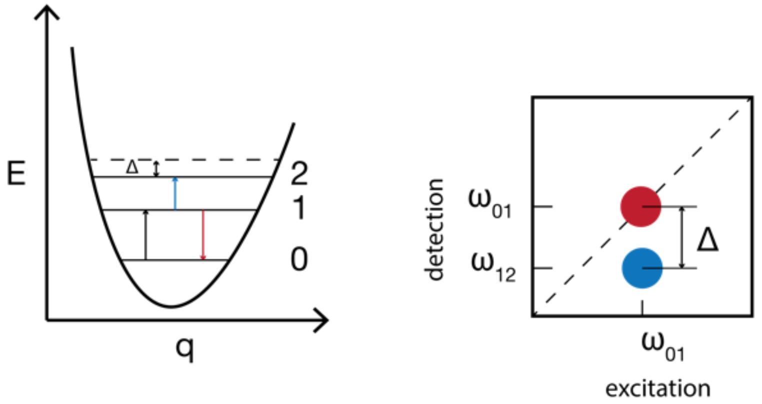

Figure 2-4. Model 2D-IR spectrum for a simple three level system. The anharmonicity between the first and second excited state can directly access from detection axis difference between ground state bleach (GSB, red) and excited state absorption (ESA, blue)

2D-IR can also provide additional information about modes coupling within the same molecule or chemical exchange two different species. In linear spectroscopy, the spectra will look the same for a two modes system no matter the two modes are coupling together or not (**Figure 2-5**). 2D-IR can help to resolve this dilemma. If the two vibrational modes are coupled together or sharing a common ground state, then there will be a cross peak that arises from exciting one mode frequency (ω_a) and detecting with another frequency (ω_b) and of course, another cross peak rises with excite ω_b and detect ω_a. This information could be useful in terms of understanding structure of a system and can also be used to distinguish two mixtures.

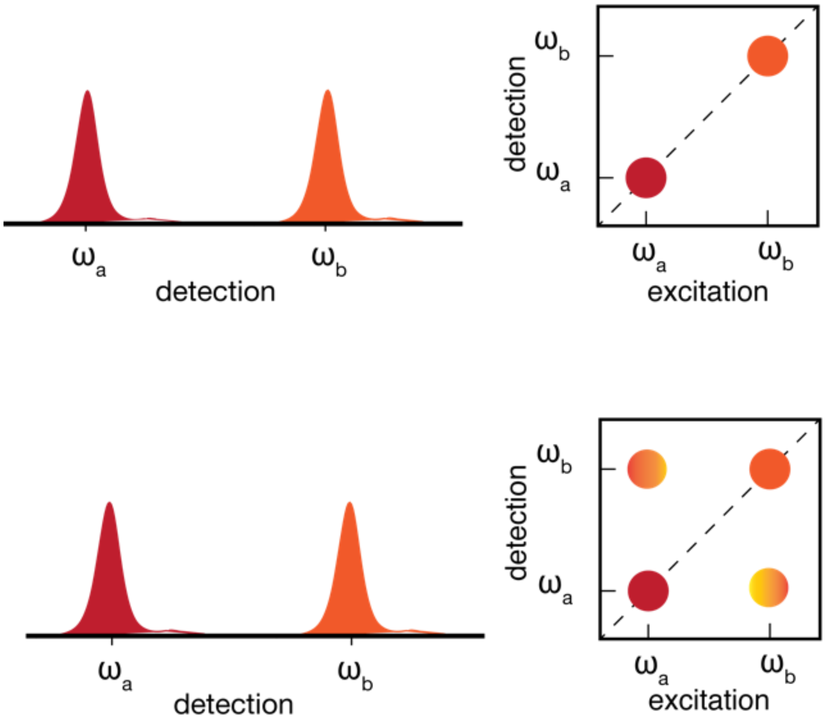

Figure 2-5. When two modes have the same linear spectrum, 2D-IR can help determine if these two modes are coupled with each other (bottom) or not (top) through cross peaks.

In the condensed phase, system and bath interaction mechanisms, like hydrogen bonds or Coulomb interactions can affect the fluctuation of energy eigenmode. Therefore, when molecules experience different environments, the eigenstate fluctuation will have different dephasing time. This is referred to as spectra diffusion. In a 2D spectrum (**Figure 2-6**), this appears as the diagonal linewidth[31, 47-52]. The ensemble of molecules will always be homogenously broadened by Doppler effect, population relaxation, pure dephasing, orientational relaxation and etcetera, which appears as the off-diagonal linewidth. Ideally, the spectra diffusion information can be extracted by fitting the diagonal peaks into a Kubo line shape function[53]. However, this is not practical because the peak shape can be distorted by multiple different mechanisms. Usually, we obtain line broadening information by analyzing how the center line slope of peaks in absorptive spectra change with τ_2 or how normalized amplitude difference of peaks between absolute rephasing and nonrephasing spectra changes with τ_2. The comparison between these two will be explained in detail in Chapter 4.

And as we will discuss this in Chapter 3, the upper and lower polariton modes are immune to inhomogeneous broadening. And we use this feature to help with polariton 2D spectra correction from the background.

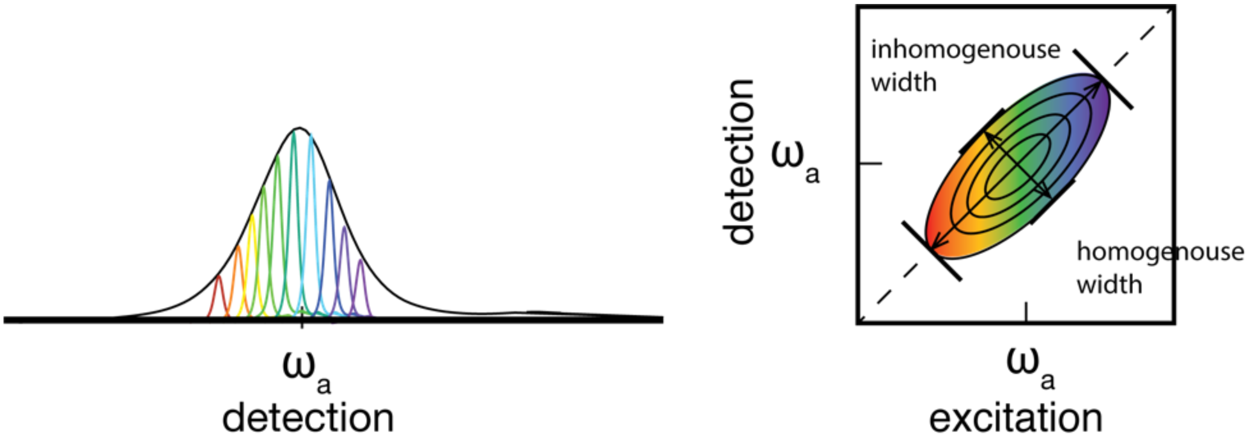

Figure 2-6: Spectral diffusion's signature in a 2D-IR spectrum. Molecules in different solvent environments will experience different frequencies, which causes absorption linewidth to be broadened inhomogeneously (left). In 2D-IR inhomogeneous linewidth and homogenous linewidth can be distinguished spectrally. The diagonal linewidth is inhomogeneous linewidth and the antidiagonal linewidth is homogeneous linewidth (right).

Another piece of information needs to be introduced is coherence map (**Figure 2-7**)[54-56]. The second pulse creates a population so usually we would expect an exponential or several exponential τ_2 dependence decay depends on the nature of system. The advance of stable ultrafast light source allows us to use a broad band pulse which can cover more than one first manifold excitations to do experiment, the coherence beat between these energy levels would show up as coherence oscillations. This has also been referred to as intraband coherence. There could also be other frequency components represent the violation of Redfield equation. To better understand the oscillation, usually, to avoid confusions, people will isolate the coherence signal from the population information and perform a Fourier transformation (FT) along τ_2. Then, the coherence map will be generated by plotting the FT amplitude in terms of the excitation and detection axis. People can do this analysis for either rephasing or nonrephasing spectra. Due to the nature of pathway, rephasing will oscillate at cross peak and nonrephasing will oscillate at diagonal peaks. The positive oscillation will show up at higher detection frequency and negative frequency oscillation will show up at lower frequency. Polariton system by nature is a strongly coupled system and the oscillation between lower polariton and upper polariton mode is a clear feature that only belongs to polariton. So, analyzing vibrational polariton's coherence map will provide a better route to avoid background confusion.

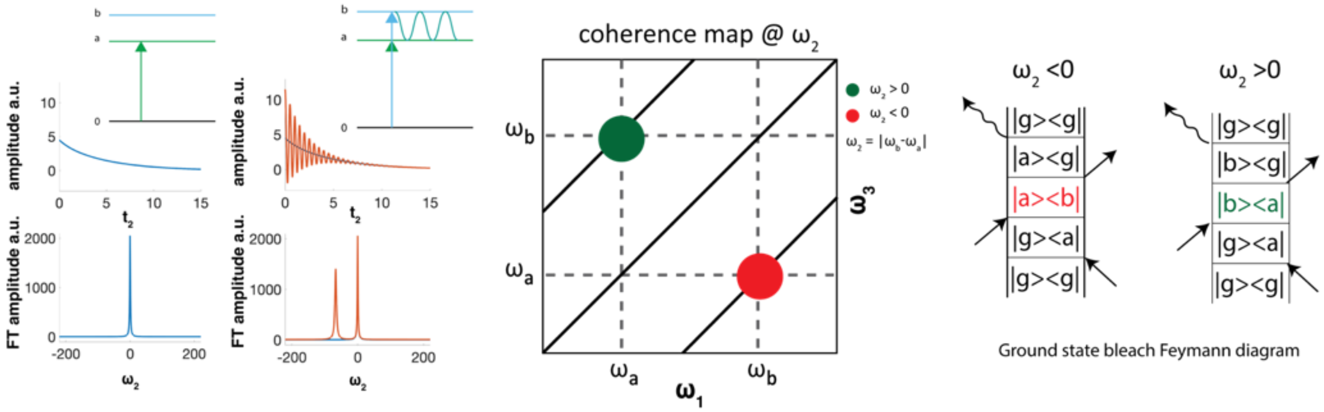

Figure 2-7. *coherence map for rephasing pathways*

2.2.2 Pump-probe geometry apparatus

There are three commonly used beam geometries for third-order spectroscopy: the fully non-collinear box, partially collinear pump-probe, and the fully collinear geometry (**Figure 2-8**). In the box geometry, the rephasing and nonrephasing signals can be collected separately and the signal is background free except for the external reference local oscillator (LO) field needed to heterodyne detect the signal field. One can also change the position of $\mathbf{k}_1$ and $\mathbf{k}_2$ to collect rephasing and nonrephasing signals separately at the same position. In the pump-probe and collinear geometries, the LO is the $\mathbf{k_3}$ field itself. For either pump-probe geometry, because $\mathbf{k_1}$ and $\mathbf{-k_2}$ or $\mathbf{-k_1}$ and $\mathbf{k_2}$ are traveling along the same direction, the result is a signal propagating along $\mathbf{k_3}$ together with other background signals (transient absorption signals arising from each pump pulse). One limitation of the fully collinear geometry is that the pump and probe fields must have orthogonal polarizations in order to be able to extinguish the very strong pump pulses, which limits our selectivity to the $R^{(3)}_{xxyy}$ tensor element. When possible, for example when using a pulse shaper, it is much easier in terms of alignment to use phase cycling in the pump-probe geometry case, where is still possible to extract the rephasing and nonrephasing signals. The fully collinear geometry is primarily used for ultrafast microscopy where it is essentially impossible to cross two beams in an objective lens. There are some limitations for this set up include that it is not suitable for anisotropy study (because the $R^{(3)}_{xxxx}$ response is not measurable), it is more challenging to implement when there is low SNR with weak transitions. Nevertheless, the collinearity of the pump and probe beams becomes convenient, and even essential, in the case where we want to measure incident angle dependent systems like polaritons.

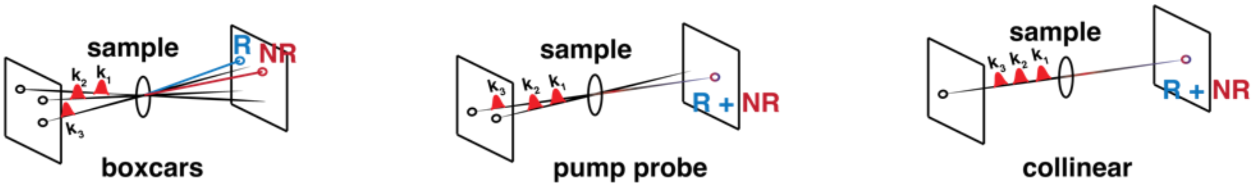

Figure 2-8. Different 2D-IR apparatus geometries. From left to right: boxcars geometry, rephasing and nonrephasing will show up at different phase matching positions; pump probe geometry, rephasing and nonrephasing will show up in the same direction traveling along with $\mathbf{k_3}$; Collinear geometry, the signal travels with the same directions as pump probe geometry but has a different polarization than the pump.

The pump-probe 2D-IR set up that I majorly contributed to in LUMOS is shown in Figure 2-8[57]. In this set up, there is a Spectra-Physics Solstice Ace chirped-pulse regenerative amplifier generating horizontal (p) polarized, 100 fs, 4.5-5.0 mJ, 800 nm pulses at a 1kHz repetition rate. This is used to pump a two-stage optical parametric amplifier (Light Conversion TOPAS-TWINS). An LP900nm filter is used to filter out the residual pump light. The resulting signal (s-polarized) and idler (p-polarized) are then separated using a dichroic beam splitter (BS). The signal and idler are then combined collinearly by using another BS in front the silver thiogallate (AGS_2) in a type I configuration. The delay stage is used to finely adjust timing between the two beams. To fullfil the type I phase matching condition (e,o,o), both the signal and idler's polarization are changed with a periscope. The signal from OPA was used as the new pump and the idler as the new signal for the different frequency generation (DFG) process. The resulting ~10 μJ mid-IR pulses entered another periscope to rotate the signal's polarization back to parallel because the grating pairs inside the pulse shaper work most efficiently when the light polarization is perpendicular to the grating blaze, which is parallel polarization (p) to the table. 5% of the mid-IR is reflected using a CaF_2 wedge to separate the reflection from the first and second surface. 95% of the light goes into the 4f geometry germanium acoustic optical modulator (AOM) pulse shaper (PhaseTech Spectroscopy). Based on a customized RF mask, the AOM can control the time delay and the phase of the two pump pulses. A detailed explanation for AOMs and using an AOM as a pulse shaper can be found in textbooks in the referrence[58-60]. The timing between the mid-IR light and the RF wave is determined by a TTL trigger from channel 7 of the Solstice. The acoustic wave generater (AWG) card will generate the desired mask and the acoustic mask will be amplified before sent to the crystal. The cooling capacity for the amplifier is >1000 W at 20^{o} C. Another TTL trigger generated from the AWG is used to control the data acquisition timing and need to be amplified using SRS delay generator to fufill the input sync pulse requirement. The pump pairs and probe are focused by a 10-cm effective focal length off-axiis parabolic mirror to the sample position. The probe, along with the signal, is focused uisng a 0.3 m CaF$_2$ lens into the spectrometer (Horiba-Yvon, iHR320) equipped with a 64-pixel liquid nitrogen cooled HgCdTe (MCT) IR detection array.

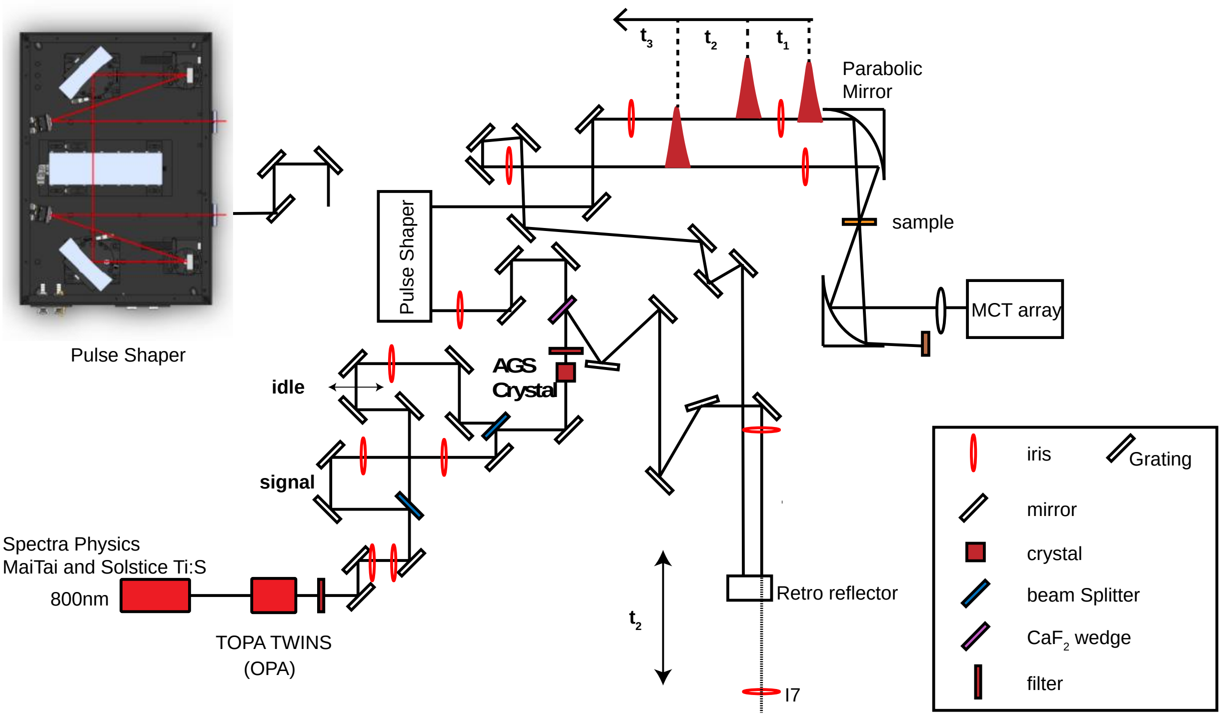

Figure 2-9. LUMOS pump-probe geometry set up.

The signal that is detected can be described using equation 2.14, 2.15. The third order polarization in the time domain can be written as the convolution between selected response functions with the three incident pulses. By substituting equation 2.11 into equation 2.5, the resulting signal polarization of the rephasing and nonrephasing signals can be written as:

$$\boldsymbol{P_R^{(3)}}\,(\boldsymbol{t}) = \int_0^\infty d\tau_3 \int_0^\infty d\tau_2 \int_0^\infty R_R^3(t-\tau_1, t-\tau_2, t-\tau_3)E(\tau_1)E(\tau_2)E(\tau_3) \qquad (2.14)$$

$$\times\, e^{i(-\boldsymbol{k_1}+\boldsymbol{k_2}+\boldsymbol{k_3})} e^{i(\phi_3+\phi_2-\phi_1)}$$

$$\boldsymbol{P}_{\boldsymbol{NR}}^{(\mathbf{3})}(\boldsymbol{t}) = \int_0^\infty d\tau_3 \int_0^\infty d\tau_2 \int_0^\infty R_R^3(t-\tau_1, t-\tau_2, t-\tau_3)E(\tau_1)E(\tau_2)E(\tau_3) \times e^{i(\boldsymbol{k_1}-\boldsymbol{k_2}+\boldsymbol{k_3})} e^{i(\phi_3-\phi_2+\phi_1)} \tag{2.15}$$

The spectrum is measured interferometrically with a LO, in this case, the probe is the LO. So that for measured spectrum S2D-IR, we have

$$S_{2D-IR}(\phi_1, \phi_2, \phi_3, \phi_{LO}) = Re[E_{2D-IR}E_{LO}^*] \propto R_R^{(3)} e^{i(\phi_3+\phi_2-\phi_1-\phi_{LO})} + R_{NR}^{(3)} e^{i(\phi_3-\phi_2+\phi_1-\phi_{LO})} \tag{2.16}$$

Most importantly, the phase of the resulting signal is:

$$\phi_{sig} = \mp(\phi_1 - \phi_2) + \phi_3 - \phi_{LO} = \mp(\phi_1 - \phi_2) \tag{2.17}$$

This means the signal's phase only depends on the phase difference of the pump pair, which can be controlled by the pulse shaper. Using this fact, we can implement different phase cycling schemes to help get remove of the phase-insensitive background, and in turn, increase the signal level while separating rephasing and nonrephasing spectra. One of the phase cycling schemes we used to separate rephasing and nonrephasing is listed in **Table 2-1**[61].

Table 2-1. Phase cycling scheme to separate rephasing and nonrephasing spectra

Frame	Input phase		
	E1(φ_1)	E2(φ_2)	E3(φ_3)
A	0	0	0
B	0	1/2π	0
C	0	3/2 π	0

The rephasing and nonrephasing responses can be extracted using this matrix method:

$$\begin{bmatrix} S_{NR} \\ S_R \\ S_{TA} \end{bmatrix} = \frac{1}{2} \times \begin{bmatrix} 1 & -\frac{1}{2}+\frac{1}{2}i & -\frac{1}{2}-\frac{1}{2}i \\ 1 & -\frac{1}{2}-\frac{1}{2}i & -\frac{1}{2}+\frac{1}{2}i \\ 0 & 1 & 1 \end{bmatrix} \times \begin{bmatrix} S_A \\ S_B \\ S_C \end{bmatrix} \tag{2.18}$$

This 2D-IR set up is one of the many set ups in LUMOS which can implement 2D spectroscopy in a wide range of optical frequencies (**Figure 2-10**).

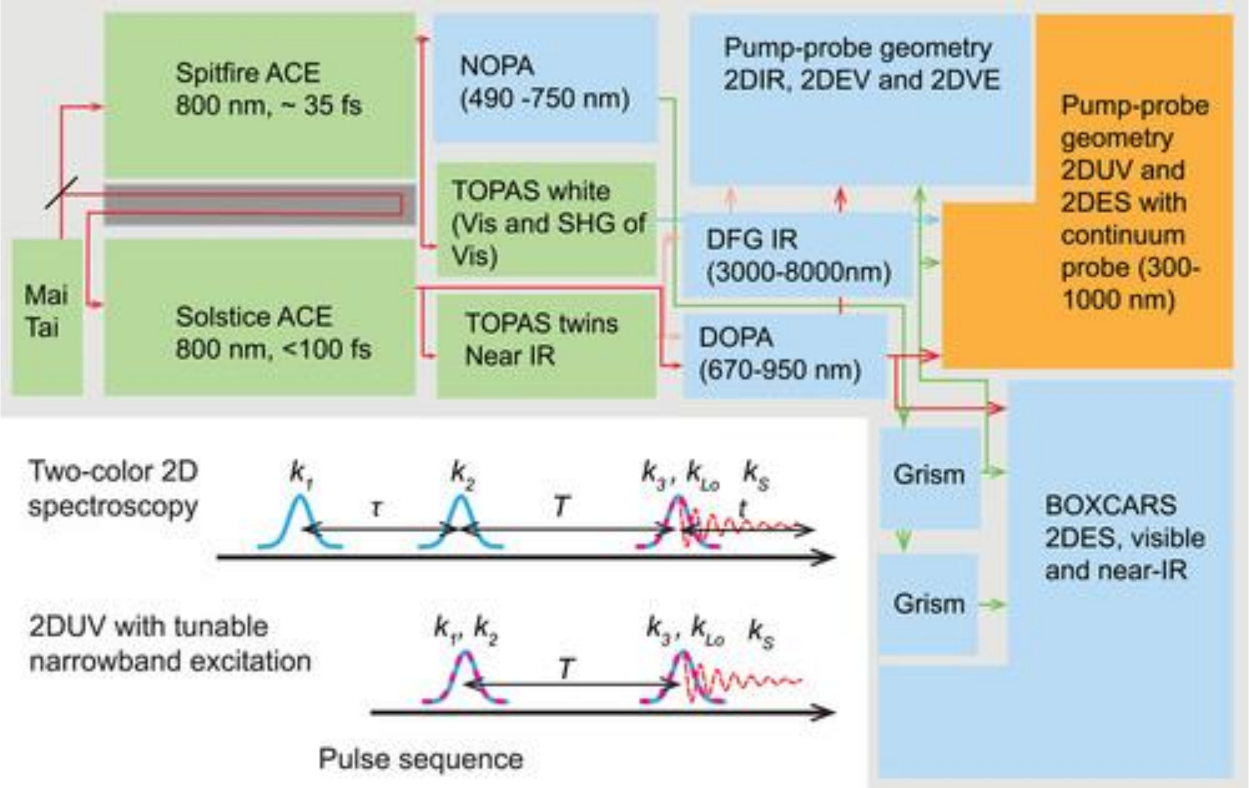

Figure 2-10. Set-ups in LUMOS. From Song et. al. showing the different layouts for different color 2D spectroscopy experiments located in LUMOS.

2.2.3 Collinear geometry apparatus

The collinear geometry was implemented to understand dual mode polaritons because of the crucial role of angle of incidence on the nature of the polariton energy structure and dynamics. The set up was modified from the previous described pump-probe geometry set up based on work by Baiz et al.[62]. Polarization selection is implemented to minimize the pump leakage into the spectrometer. The probe's polarization is rotated 90° from parallel to perpendicular by using a half waveplate. A wire grid polarizer is used as a beam splitter to combine the pump and probe by transmitting the probe (s-pol) and reflecting the pump (p-pol). The two-polarizer system with the opposite selection is used to minimize the pump leakage. The signal polarization is also selected based on polarization of pump and probe, so only the $R^{(3)}_{xxyy}$ tensor element is being selected.

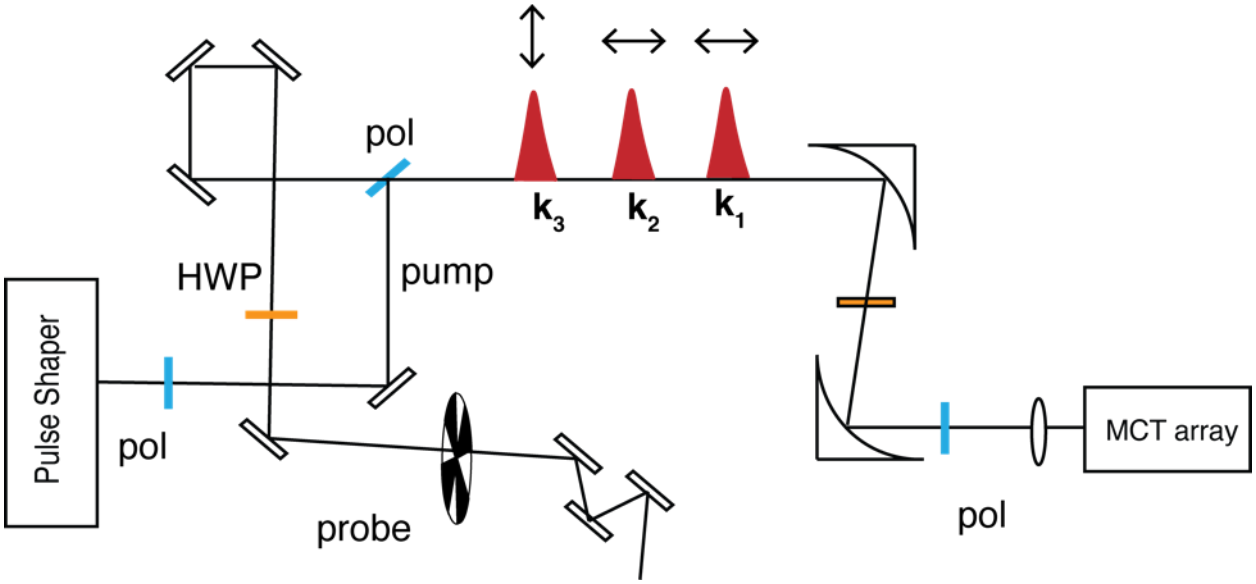

Figure 2-11. Essential parts of the collinear set 2D-IR set up. The probe's polarization is rotated by a half wave plate(HWP) from parallel polarization to perpendicular polarization. Two polarizers

To elaborate on polarization dependence measurements, using different polarizations of the electric field can help to selectively choose the signal's polarization. A general term in the nonlinear polarization in the frequency domain can be represented as:

$$P_i^{\omega} \propto \chi_{ijkl}^{(3)}(-\omega; \omega_1, \omega_2, \omega_3) E_j^{\omega_1} E_k^{\omega_2} E_l^{\omega_3} \qquad (2.18)$$

In which the $\chi_{ijkl}^{(3)}(-\omega; \omega_1, \omega_2, \omega_3)$ is the third order susceptibility and it is a fourth rank tensor. In general, $\chi_{ijkl}^{(3)}$ has 81 elements but only 21 of them are non-zero. In an isotropic environment, 4 of them survive ($\chi_{xxxx}^{(3)}$, $\chi_{xxyy}^{(3)}$, $\chi_{xyxy}^{(3)}$, $\chi_{xyyx}^{(3)}$) and only 3 elements are independent based on the symmetry ($\chi_{xxxx}^{(3)} = \chi_{xxyy}^{(3)} + \chi_{xyxy}^{(3)} + \chi_{xyyx}^{(3)}$). As showed by Tokamakoff et. al., the ratio of the amplitudes between crosspeak and diagonal peak using XXXX and XXYY polarization is different. Further, the ratio between the two experiments can help with understanding orientational dynamics. However, the collinear geometry can not be used in analyze orientational dynamics due to its restriction to the crossed polarization tensor element.

An experimental challenge cannot be ignored, the mid-IR wire grid polarizer does not have sufficient extinction to block all the pump light before the spectrometer. To minimize the pump-pump scattering, and to get rid of the unwanted nonlinear signals, both phase cycling and an optical chopper needs to be implemented.

Table 2-2. Phase cycling scheme to isolate the 2D-IR absorptive signal from unwanted interference

Frame		Input phase			Output phase			
		E1(φ_1)	E2(φ_2)	E3(φ_3)	E_1E_2	E_1E_3	E_2E_3	S_{2DIR}
Chopper off	A	0	0	0	0	0	0	0
	B	0	π	0	π	0	π	π
	C	π	0	0	π	π	0	π
	D	π	π	0	0	π	π	0
	a	0	0	0	0	-	-	-

Chopper on	b	0	π	0	π	-	-	-
	c	π	0	0	π	-	-	-
	d	π	π	0	0	-	-	-

The unwanted signal from the table 2.2-2 is the phase dependent interference terms between E_1E_2, E_1E_3 and E_2E_3. In this phase cycling scheme, the signal has the form:

$$S_{2DIR} = (B + C) - (A + D) - ((b + c) - (a + d)) \tag{2.19}$$

Unfortunately, because of these unwanted interference terms, in the collinear geometry, one cannot separate the rephasing and nonrephasing spectra using the previous phase cycling method motioned in **Table 2.2**.

2.3 Summary

In this chapter, we included a ‘decoder’ for public and new graduate student to understand 2D-IR spectrum and the research described in later chapters, including the meaning of peak position, types of peaks and how to extract population, coherence, and diffusion dynamics. To help people better understand what 2D-IR measures along with the strength and limitation of this technique, we introduce a brief theory about nonlinear, three pulse sequence, light matter interaction in the weak coupling regime and include good reference for people who wants to learn more. And finally, we talked about two experimental implementations, partially collinear, and fully collinear geometry in our lab in detail.

Chapter 3 Vibrational Polariton

Polariton's name comes from the combination of 'polarization' and 'photon', indicating its quasiparticle nature. Chapter 2 summarizes the fundamentals of spectroscopy that are the most relevant to this work, and it based entirely on the perturbative regime of relatively weak-light matter interactions. From the perspective of perturbation theory, the induced polarization is treated as an independent field. However, if the induced polarization acts back on the incident field with a sufficiently high exchange rate, the process is considered to be in the *strong coupling* regime. Strong coupling can happen under restricted conditions, like placing one oscillator, or a collection of oscillators, between a simple pair of high reflectivity mirrors, or by using more complex cavity designs. To provide an introduction of the basic concepts of vibrational polaritons[9, 17, 18, 63-65], this chapter will summarize the prevailing theoretical treatments of strong light-matter coupling that leads to the formation of polariton states.

3.1 Understanding polaritons

3.1.1 Basic theory

The rate of a spontaneous photon emission from a molecule in vacuum is determined by Fermi's Golden rule, usually characterized by the so-called Einstein A coefficient. The rate of spontaneous emission is proportional to the product of the transition dipole moment and the density of electromagnetic modes at the emission frequency. By manipulating the density of states of the accepting modes (i.e. the light), it is possible to enhance or suppress spontaneous emission. This process is known as the Purcell effect[66]. As one example, the spontaneous emission rate can be modified by an optical cavity because only specific modes that satisfy the cavity's boundary conditions propagate, so tuning a cavity in resonance with the emission can enhance fluorescence, whereas a cavity that is anti-resonant with the emission will suppress the fluorescence. The degree of cavity's effect is related to the quality factor (Q) and the cavity mode volume. In a high-Q cavity, there is a significant probability that the molecule will reabsorb the emitted photon before it dissipates outside the cavity. As the field and the molecule start to exchange energy at a rate Ω_{eq}, the spontaneous emission becomes reversible. In this regime, the molecule is coupled with its own field without an external applied field, and this is referred to as a "Vacuum Rabi Oscillation." The coupling rate (Ω) is proportional to the square root of the number of molecules, N, coupled to the cavity mode.

$$\Omega = \Omega_{\mathrm{eq}}\sqrt{N} \tag{3.1}$$

There are multiple models to describe polaritonic systems. The classical transfer matrix model is commonly used to fit the linear spectrum, and is able to describe both dispersive and absorptive (i.e. the complex index of refraction) aspects of the optical response by treating the molecule as a Lorentzian oscillator inside the cavity. Transfer matrix is a commonly used mathematical description to analyze how electrical magnetic wave prorogating through different one-dimensional homogenous materials[67]. The foundation of transfer matrix is the combination of Maxwell equation and Fresnel's law. Simplified version of transfer matrix is commonly used in optic ray tracing under the assumption of no magnetic field. Using transfer matrix can connect the ingoing and outgoing electric field on the same side of the material together. Each material can be treated as a 2x2 matrix, and the total transfer matrix is simply the matrix multiplication of different components inside.

The transmission spectrum can be easily derived[68] as:

$$T = \frac{(1-R)^2 \exp\left(-\frac{\alpha L}{cos\theta}\right)}{1 + R^2 \exp\left(-\frac{2\alpha L}{cos\theta}\right) - 2Rexp(-\frac{\alpha L}{cos\theta})\cos\,(2\eta\omega Lcos\theta/c)} \tag{3.2}$$

Inside the equation, variable η and α is the classical refract index and absorption coefficient of the vibrational mode. L is the length of the cavity and θ represents the incident angle.

$$\eta(\omega) = 1 + \sum_i \frac{2\delta\omega_i(\omega_{oi} - \omega_i)\eta_{oi}}{(\omega_{oi} - \omega_i)^2 + \delta\omega^2} \tag{3.3}$$

$$\alpha(\omega) = \sum_i \frac{\delta\omega_i^2\alpha_{oi}}{(\omega_{oi} - \omega_i)^2 + \delta\omega^2} \tag{3.4}$$

The central frequency of the molecule transmission for each molecular mode is ω_{oi}; $\delta\omega_i$ is the HWHM of atomic transmission broadening; η_{oi} is the unsaturated maximum refractive index while α_{oi} is the unsaturated maximum power absorption coefficient. **Figure 3-1** is an example of using transfer matrix way to simulation a single polariton.

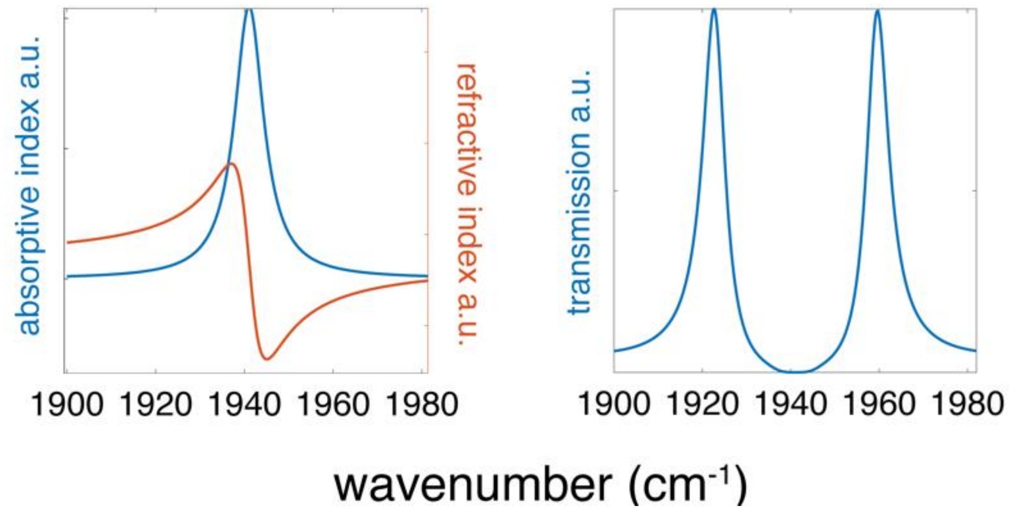

Figure 3-1. Lorentzian model simulated absorptive and refractive index and transfer matrix way of simulating polariton transmission spectrum

Alternative, a basic quantum mechanical approach often used to explain the strong light and matter coupling, due to Jaynes and Cumming[69], models the Hamiltonian with three terms, one for each of the photon, electron and photon-electron coupling. For vibrational polaritons, in which the coupling happens with an ensemble of photons and molecules, under the rotating frame approximation, the Hamiltonian can be constructed as:

$$\begin{aligned} \hat{H}_{pol} &= \hat{H}_{cav} + \hat{H}_{vib} + \hat{H}_I \\ &= \sum E_{cavity}\, \hat{c}^\dagger \hat{c} + \sum E_{vib}\, \hat{\alpha}^\dagger \hat{\alpha} + \sum \hbar\Omega\, (\hat{c}^\dagger \hat{\alpha} + \hat{\alpha} \hat{c}^\dagger) \end{aligned} \tag{3.5}$$

where $\hat{c}$ and $\hat{c}^\dagger$ are cavity photon's creation and annihilation operators and $\hat{\alpha}$ and $\hat{\alpha}^\dagger$ are the vibration polarization's creation and annihilation operators. $\hbar\Omega$ arises due to the molecular dipole and photon interaction. One might notice that weak coupling has a similar Hamiltonian construction; the only difference is the $\hat{H}_I$ in weak coupling case is treated perturbatively, while the energy exchange is expressed explicitly in the strong coupling case. Nevertheless, this Hamiltonian can be diagonalized into the polariton operators $\hat{p}_{LP}$ and $\hat{p}_{UP}$, which is a linear combination of the vibration's and photon's creation and annihilation operators. These two new polariton operators are called the lower polariton (LP) and upper polariton (UP) operators. After diagonalization, the Hamiltonian has the following form:

$$\hat{H}_{pol} = \sum E_{LP}\, \hat{p}_{LP}^\dagger \hat{p}_{LP} + \sum E_{UP}\, \hat{p}_{UP}^\dagger \hat{p}_{UP} \tag{3.6}$$

In which:

$$\hat{p}_{LP} = X\hat{\alpha} + C\hat{c}$$

$$\hat{p}_{UP} = C\hat{\alpha} + X\hat{c}$$

The coefficients X and C, often called Hopfield coefficients, describes the linear composition of light and molecule. They must satisfy the normalization condition

$$|X|^2 + |C|^2 = 1.$$

The eigenvalues for the LP and UP after diagonalization can be written as:

$$E_{LP/UP} = \frac{1}{2}[E_{vib} + E_{cav} \ \pm \sqrt{4\hbar^2\Omega^2 + (E_{vib} - E_{cav})^2} \tag{3.7}$$

When the detuning of the vibrational mode and the cavity mode is zero, the energy difference between the LP and UP reaches its minimum value; this minimum energy often called the vacuum Rabi splitting.

If we define ΔE to be the detuning of cavity mode and vibrational modes, $\Delta E = E_{vib} - E_{cav}$, the Hopfield coefficients can be rewritten as:

$$|X|^2 = \frac{1}{2}(1 + \frac{\Delta E}{\sqrt{\Delta E^2 + 4\hbar^2\Omega^2}})$$

$$|C|^2 = \frac{1}{2}(1 - \frac{\Delta E}{\sqrt{\Delta E^2 + 4\hbar^2\Omega^2}})$$

3.1.2 Fabry Perot cavity

The most widely used and straightforwardly implemented cavity is a planar Fabry Perot cavity. The construction of this cavity only requires having two high reflectivity mirrors. Spatially, by selecting the inter-mirror distance (d), one can selectively chose the order and the frequency of longitudinal mode to couple with the desired vibrational mode. These longitudinal modes are standing waves, and just like a harmonic oscillator, the *n*th energy level will have *n*-1 nodes. In the frequency domain, because of multibeam interference, the resulting total transmission and reflection are evenly spaced Lorentzian functions with the free spectral range (FSR) equal to the reciprocal of the cavity transit time. The full width at half maximum (FWHM) of each mode reflects the imperfection of reflectivity.

The cavity's wave vector, **k**, can be decomposed into two components $k_\perp$ and $k_{//}$. The standing wave inside the cavity requires $k_\perp = \frac{\pi}{L}$ in vacuum, but $k_{//}$ varies with the angle of incident light. Based on Maxwell's equations, the dispersion relationship between **k** and frequency can be reconstructed as:

$$\omega = \frac{c}{n}\boldsymbol{k} = \frac{c}{n}\sqrt{k_{\perp}^{2} + k_{\parallel}^{2}} \tag{3.8}$$

In which n is the index of refraction.

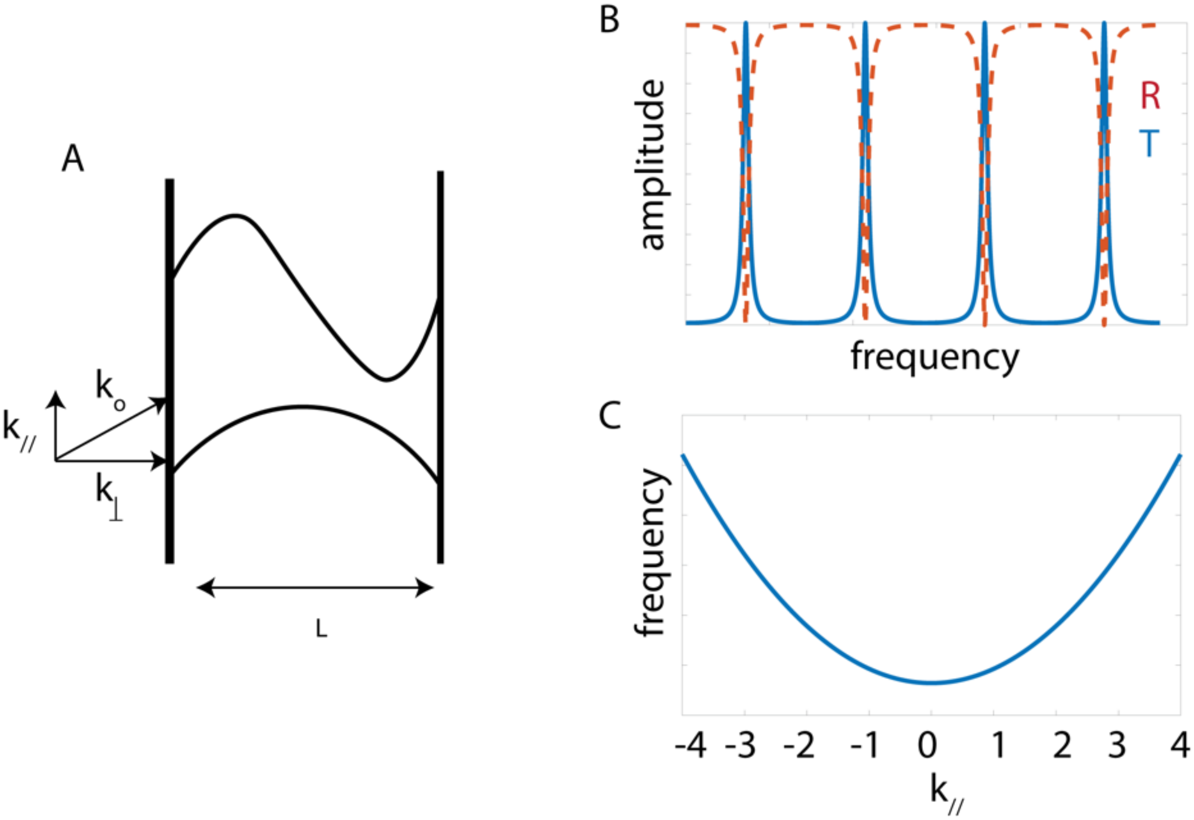

Figure 3-2. (A) A Fabry Perot cavity with two examples of confined standing wave modes; decomposition of the incident wave vector into $k_{\perp}$ and $k_{//}$. (B) Transfer matrix simulated transmission and reflection mode in the frequency domain. (C) The dispersion relationship between $k_{//}$ and frequency.

If the light energy has been treated quantum mechanically, the energy dispersion relation of the cavity can be written as

$$E_{cav} = \frac{\hbar c}{n}k = \frac{\hbar c}{n}\sqrt{k_{\perp}^{2} + k_{\parallel}^{2}} \tag{3.9}$$

At the limit of $k_{//} << k_{\perp}$, the relationship reduces to the equation 3.10 by applying the parabolic approximation:

$$E_{cav} = E_{cav}(k_{\parallel} = 0) + \frac{\hbar^2 k_{\parallel}^2}{2(2\pi\hbar/\lambda_{cavity}c)} \tag{3.10}$$

The $\frac{2\pi\hbar}{\lambda_{cavity}c}$ can be defined as the cavity mode's effective mass m_{cavity}.

3.1.3 Dispersion relation of polaritons

To continue the discussion about the dispersion relationship when medium is strongly coupled with a cavity, it is helpful to consider that different frequencies experience different indexes of refraction, which is essentially the permittivity when propagating inside a medium. The dispersion relationship for a molecule strongly coupled to light can be generalized as:

$$\frac{c^2k^2}{\omega^2} = \epsilon(\omega) \tag{3.11}$$

in which $\epsilon(\omega)$ is the permittivity of the material. The permittivity can be modeled using the classical Lorentzian model, so that the dispersion relationship becomes:

$$\frac{c^2k^2}{\omega^2} = \epsilon_b + \frac{f}{\omega_o^2 - \omega^2 + i\omega\gamma} \tag{3.12}$$

in which the ω_o is the central frequency of the oscillator, γ is the dephasing rate of the oscillator, f is the oscillator strength, and ϵ_b is the background dielectric constant.

The vibrational transitions within the molecules we want to study need to be treated quantum mechanically. Similar to equation 3.10, the energy dispersion relationship for polaritons can also be written as eqn 3.13:

$$E_{LP,UP} = E_{LPUP}(k_{\parallel} = 0) + \frac{\hbar^2 k_{\parallel}^2}{2m_{LP,UP}} \tag{3.13}$$

in which the effective mass of the LP and UP can be defined as:

$$\frac{1}{m_{LP}} = \frac{|X|^2}{m_{vib}} + \frac{|C|^2}{m_{cav}}$$

$$\frac{1}{m_{UP}} = \frac{|C|^2}{m_{vib}} + \frac{|X|^2}{m_{cav}}$$

Because the effective mass of light in the cavity is much smaller than the effective mass of the vibration, these two equations can be further reduced to:

$$m_{LP} \sim m_{cavity} / \, |C|^2$$

$$m_{UP} \sim m_{cavity} / \, |X|^2$$

An example of a simulated dispersion relationship with a negative detuning polariton system is shown in **Figure 3-3**. There is no value of $k_{//}$ for which the LP and UP polariton modes have the same energy. This is one of the signatures of strong coupling.

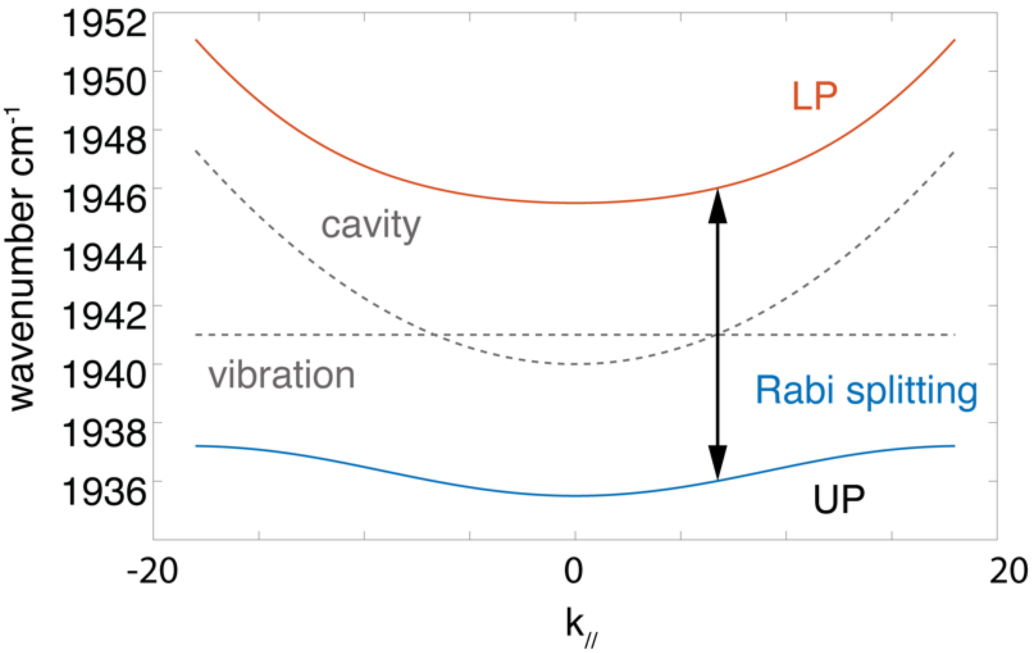

Figure 3-3. polariton dispersion curve. When there is zero detuning, the frequency different is called Rabi Splitting.

This dispersive feature is a blessing and a curse when trying to understand the nonlinear properties using absorptive nonlinear spectroscopy. The vacuum Rabi splitting arises from the zero-point fluctuations of the cavity modes and does not rely on optical excitation with an external field. So absorptive spectroscopy by its nature can only probe one polariton mode depending on the choice of the incident angle of light wave vector. Fully non-collinear and pump-probe beam geometries can only be used for zero detuning polariton analysis. Changing the angle between the light and the cavity normal allows to map the full polariton dispersion, but this is essentially impossible when the optical beams are incident from more than one direction. So ideally, a collinear geometry should be used whenever the system has nonzero detuning.

3.1.4 Dark modes

One additional component of a practical polaritonic system that needs to be considered is presence of the so-called *dark* states, also referred to as *reservoir* states (**Figure 3-4**). Whether there is a single molecular mode or an ensemble of *N* molecular modes coupling with one cavity mode, there will only be two polariton eigenmodes formed, the rest of the *N*-1 modes are called dark states[70]. They have the same frequency as the molecular modes and are much less delocalized than the polariton states.

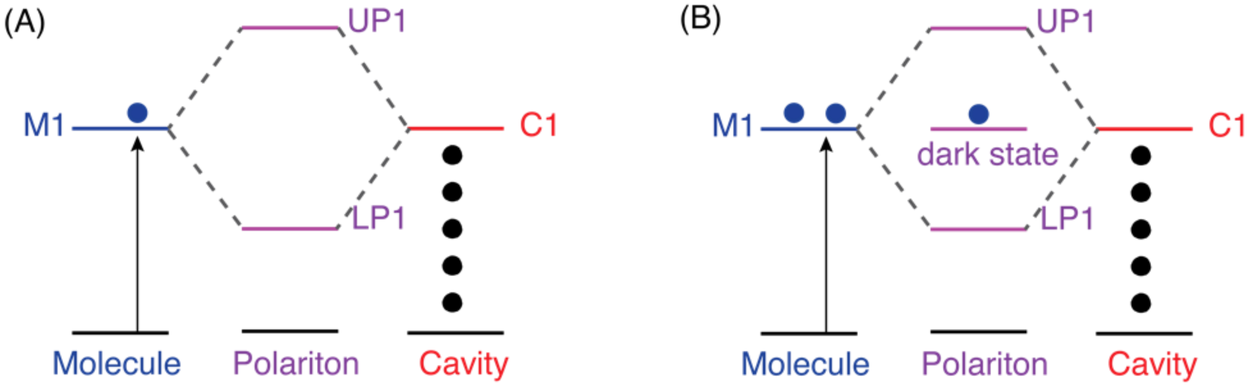

Figure 3-4. polariton energy levels. (A) one molecule mode and one cavity mode coupling will result in two polariton modes. (B)two molecule modes and one cavity mode will result in the same two polariton modes and one cavity mode which has the same frequency as the molecule mode

The dark state only formed by mixing molecule states together, its dipole moment is the linear combination of molecular vibrational mode. For the purpose of simplicity, if we only coupled two molecular modes with a single cavity mode the dipole moment could be write as:

$$\mu_{0d} = \sum_{j}^{N} c_j^{(d)} \mu_{0j} = \frac{1}{\sqrt{2}}(-\mu_{0a} + \mu_{0b}) \tag{3.14}$$

The dark state will be truly dark if all the transition dipoles are aligned. However, in liquid solution, the spectroscopically active solute molecules are in constant motion, so it is impossible to have all molecular modes aligned perfectly. Therefore, dark mode’s transition will not be entirely forbidden. This orbitational dependence coupling also reflect on the coupling strength on individual molecule.

It is also impossible to have all molecular modes coupled identically with the cavity mode, which only couples with the in-plane projection of the dipole moment. Sometimes those uncoupled molecular modes are called ‘dark modes’ as well, which makes this term slightly confusing. In both cases, dark states have the same energy as the bare molecule transition.

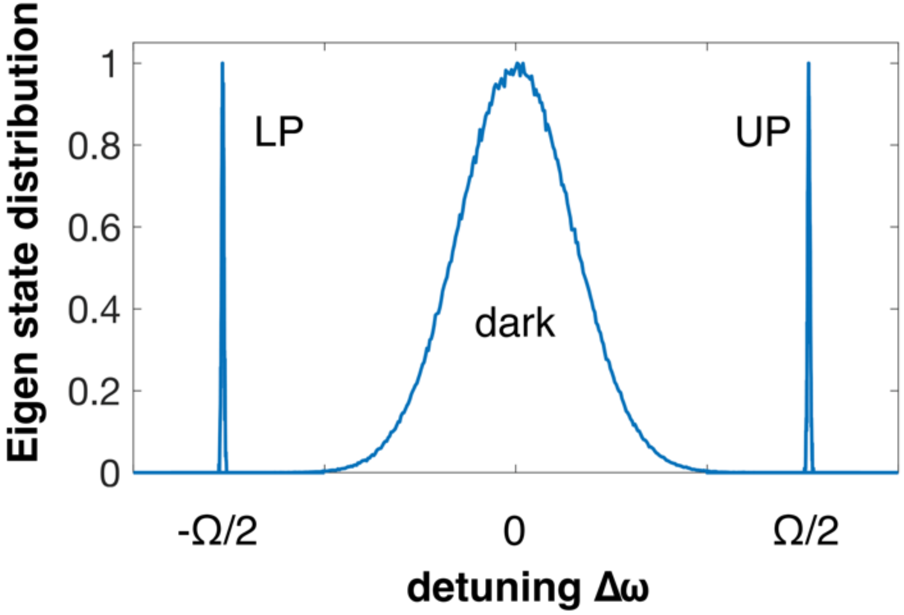

Figure 3-5. Eigenstate distribution of several molecule states coupled with one cavity mode

One interesting and important feature of the dark modes is that they adopt all the inhomogeneous broadening from the bare molecules [71-73]. **Figure 3-5** shows a simulation of eigen state distribution of multiple molecule states coupled with one cavity state with added disorder to mimic molecule in different environment. It clearly shows that there is only one single value for each polariton eigenstate while dark state's energy is a distribution. Viewed from the polariton perspective, the polariton modes can the thought of as being immune from inhomogeneous broadening. The linewidth of both polariton states is determined by the homogenous linewidths from the light and the vibrational modes only. Also, the inhomogeneous broadening has little effect on Rabi splitting[74].

3.1.5 Orientational and spatial coupling

Vibrational polariton's closest physics analogy is solid-state quantum well (QW) microcavity polariton. They share a lot of things in common as we discussed in the previous sessions but vibrational polariton also has some other properties that QW polaritons doesn't have. First of all, in QW polariton, all translational dipole moment is fixed spatially in the x-y plane based on the growth direction and can be placed spatially right under the place that has highest mode volume. In this case, every QW inside have the same individual coupling rate with different $k_{//}$. While in vibrational polariton system, because everything is in solution phase, it is impossible to have all molecular modes coupled identically with the cavity mode. And usually, we can't 'place' the solution at different places inside the cavity. In this case, the molecule inside all has different coupling rate with the cavity's in plane wave vector based on their spatial position. There is an example showing by using a film, they can show that the coupling rate changes based on mode volume[75] (**Figure 3-6**). The bulk result is as we previously discussed, there will be some uncoupled molecule modes. And these modes will be spatially distributed based on the longitudinal mode distribution so as the coupling rate.

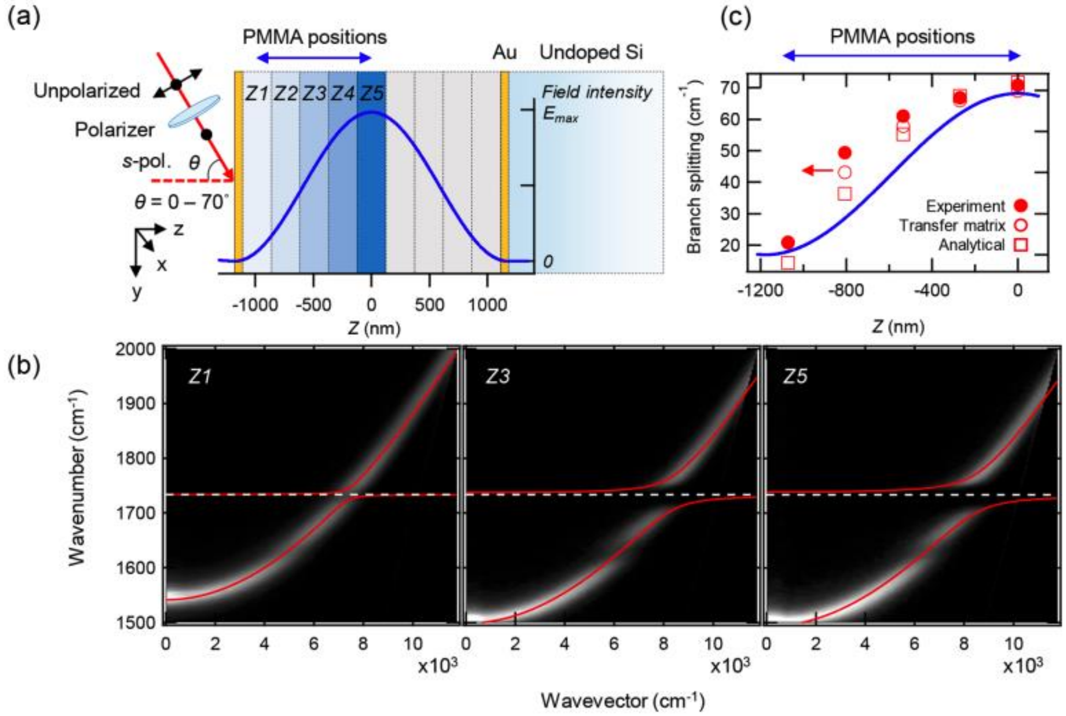

Figure 3-6. Taken from reference 75[75]. A demonstration of how coupling rate being affected by spatial distribution of the longitudinal mode. (a) selectively chose PMMA position at Z1-Z5. (b) strong coupling rate depends on mode volume

3.1.6 Dynamics relaxation

The molecule's vibrational modes and cavity's finite lifetime need to be taken into accounts. Usually, the lifetime of a molecule mode (10-200ps) is longer than the cavity lifetime(1-10ps). Radiative decaying process which mostly dominated by the lifetime of cavity mode and Hopefield coefficient; For example, at zero detuning, polariton spends half of the time behave like a light and the other half like a molecule. The lifetime of the polariton is double the lifetime of the cavity mode which reflets the fact that it can only escape the cavity through its photon phase[64]. The relaxation of both polariton modes also includes relaxing to the dark state which has longer relaxation time is dominated by the lifetime of vibrational modes.

Rabi oscillation can be manifest in time domain measurement as sinusoidal oscillations with the period equals to the frequency different between LP and UP. As we previously discussed, Rabi oscillation represent the coherence energy change the two polariton modes. The lifetime of this oscillation represents the composition of the polariton modes pair[39].

Chapter 4 Direct Comparison of Amplitude and Geometric Measures of Spectral Inhomogeneity Using Phase Cycled 2D-IR

The work presented in this chapter has been published in the following paper:

Rong Duan, Joseph N. Mastron, Yin Song, and Kevin J. Kubarych , "Direct comparison of amplitude and geometric measures of spectral inhomogeneity using phase-cycled 2D-IR spectroscopy", J. Chem. Phys. 154, 174202 (2021) https://doi.org/10.1063/5.0043961

4.1 Introduction

Spectral inhomogeneity is a general property of line shapes involving ensembles of absorbers, and methods to measure, or remove, the broadening it causes have long been employed in nonlinear spectroscopy. What began as Ramsey fringe[76] and spectral hole burning[77] using continuous wave excitation has evolved in recent years to ultrafast photon echo[58, 78, 79] and multidimensional optical spectroscopy[80, 81]. Regardless of the spectral range, central to the goal of understanding the influence of environmental dynamics is to separate inhomogeneous broadening from homogeneous and motionally-narrowed dephasing.[82, 83] Though these contributions are often viewed as being qualitatively different processes, from a Kubo-Green line shape[84] perspective we understand the distinction between these mechanisms—originally introduced phenomenologically by Bloch[85] and Redfield[86]—to be one of time scale. The essential parameter that determines the optical response in this picture is the frequency-fluctuation correlation function (FFCF):

$$C(t) = \langle \delta\omega(0)\delta\omega(t) \rangle = \langle \omega(0)\omega(t) \rangle - \langle \omega \rangle^2 \tag{4.1}$$

Although it underlies measurements as simple as one-dimensional absorption spectra, it is not possible to extract the FFCF unambiguously from those measurements.[87] However, in multidimensional spectroscopies, it is widely accepted that elongation of a peak shape along the diagonal is a signature of inhomogeneous broadening.[82, 88-91] Subsequent investigations demonstrated several easily-measured observables that relate to this broadening that are proportional to the FFCF,[92] and analysis methods can be chosen subject to other practical considerations such as the relative homogeneous line width[31] and anharmonicity. Fits to the entire absorptive 2D response can be used to consider the potentially complicating interference of ground state bleach/stimulated emission (GSB) and excited state absorption (ESA) features.

Perhaps the most widely used metric in two-dimensional Infrared spectroscopy (2D-IR) is a geometric fitting of the center line slope (CLS)[47, 91-93]. Under the Gaussian approximation of spectral diffusion dynamics[79], the spectral feature is tilted as a linear function of the frequency and the decay of this slope reports on the spectral diffusion time scale. Several alternatives to the CLS method provide access to spectral diffusion using similar metrics, including the nodal line slope[94] between the GSB and ESA features, the phase line slope from a constant contour level of the 2D spectral phase,[52] or fits of the ellipticity.[31] Geometric methods work best in cases where the observed line shape is broad. Additional complications arise when there are two spectral features close to each other, though strategies do exist to circumvent this situation.[47] However, energy-transfer dynamics that occur on similar timescales to spectral diffusion confound these methods by making the line shape appear more symmetric.[95]

The Inhomogeneity Index (II) introduced by Roberts *et al.*[52] is an alternative measure of spectral inhomogeneity that does not rely on geometric peak shape analysis, but rather can be calculated from the amplitudes of the rephasing ($\mathbf{k_R} = -\mathbf{k}_1 + \mathbf{k}_2 + \mathbf{k}_3$) and nonrephasing ($\mathbf{k}_{NR} = \mathbf{k}_1 - \mathbf{k}_2 + \mathbf{k}_3$) spectra ($A_r$ and A_{nr}, respectively).

$$II(t) = \frac{A_r(t) - A_{nr}(t)}{A_r(t) + A_{nr}(t)} \tag{4.2}$$

Since the initial discovery of spin echoes in nuclear magnetic resonance,[96] it has been understood that phase conjugation during the two coherence evolution time delays leads to an enhancement of the signal amplitude when there is inhomogeneous broadening. As the nonrephasing signal is not similarly enhanced due to a lack of phase conjugation ($\mathbf{k}_1$ and $\mathbf{k}_3$ have the same sign), it does not produce an echo. Comparing the change in amplitude observed in echo-producing rephasing response relative to the non-echo-producing nonrephasing response yields the II at a given waiting time (t_2) between excitation and detection. It can be shown[52] that the II is related to the normalized FFCF, $\overline{C(t)}$:

$$\frac{C(t)}{C(0)} = \overline{C(t)} = \sin\left(\frac{\pi}{2} \times II\right) \tag{4.3}$$

In practice, one selects a region of the rephasing and nonrephasing spectra, as small as a single spectral point, and integrates the absolute magnitude of each spectrum within that region. We have used this method in many studies of spectral diffusion dynamics in a wide range of systems from protein hydration[97-101] and the glass transition[102] to photocatalysis.[103, 104] Despite many demonstrations of the utility of the inhomogeneity index, it is not widely used in the 2D spectroscopy community. There are few reports[52, 105] that directly compare experimental measurements of the inhomogeneity index with more common metrics such as the center line slope, though comparison of spectral diffusion time scales for similar systems do show a general consistency. This agreement is nevertheless expected from the basic theoretical formulations that indicate both are proportional to the normalized FFCF.

Although the II and geometric methods, in principle, access the same FFCF, the II has an advantage in that it also can be measured quickly without measuring multiple full 2D spectra. Rapid Acquisition of Spectral Diffusion (RASD)[106-108] makes use of heterodyne detection at a fixed coherence time (t_1) to record rephasing and nonrephasing signal fields. As a function of the waiting time, the reduced dimensionality of the RASD measurement yields FFCF decays that agree quantitatively with the inhomogeneity index recorded using full 2D-IR spectra. However, implementation of the II method requires the ability to separately resolve the rephasing and nonrephasing signals, and not just their sum as the absorptive spectrum as accessed with the pump-probe geometry. The II method thus requires either the use of the noncollinear geometry to spatially resolve these signals, or phase-cycling in a pump-probe geometry, as will be described below. As phase cycling is an additive process, it does not reduce the overall signal to noise ratio as in amplitude modulation schemes, and the overall measurement time is not appreciably increased.

New spectroscopic challenges are emerging where non-geometric measures of spectral diffusion will be beneficial, such as those where spectral line shapes are affected by propagation through a sample. Spectral shaping due to high optical densities or large beam crossing angles have been well documented,[109-111] and there are prescriptions for removing these distortions. There has recently been rapidly growing interest in polaritonic systems, where strong coupling occurs between molecular transitions and resonant optical cavities.[36, 112-115] In planar cavities, strong coupling can be achieved with moderately concentrated (10 – 100 mM) concentrated solutions of transition metal complexes[116]. As many of these organometallic molecules are also widely used in catalysis, it is possible that strong coupling may enable the design of new catalytic reactions.[14] Since most theoretical models of ensembles of molecules coupled to optical cavities neglect spectral diffusion, it is not clear how processes such as solvation dynamics and intramolecular flexibility in transition metal complexes will manifest in the dynamics of the hybridized polariton state. These dynamical processes can lead to complex spectra with multiple relatively narrow features at frequencies where light can be transmitted through the cavity.[36] As a result of this feature narrowing due to the cavity finesse, a CLS analysis of spectral diffusion in these systems is challenging.

Here, we compare the non-geometric II method to the more commonly applied CLS analysis using a pulse shaper-based 2D-IR spectrometer in the pump-probe geometry. Rephasing and nonrephasing spectra can be obtained using phase cycling, and thus the calculated II can be directly compared to the CLS analysis of the absorptive 2D spectra of the same dataset.[61, 117] To the best of our knowledge, this comparison has not been made in 2D spectroscopy using pulse shaping with phase-cycling.

As our model systems, we use tungsten hexacarbonyl (WCO_6) to represent the most simple case, and for a more complex vibrational structure, we consider methylcyclopentadienyl (Cp’) manganese tricarbonyl [$Cp'Mn(CO)_3$] (MCMT), a metal-carbonyl tripod complex (**Fig. 4-1A**). The vibrational spectrum of MCMT contains three coupled IR-active metal carbonyl bands, two of which are nearly degenerate, which are moderately inhomogeneously broadened in 1-propanol solution.

4.2 Experimental methods

Tungsten hexacarbonyl ($W(CO)_6$) and methylcyclopentadienyl manganese tricarbonyl ($Cp'Mn(CO)_3$, MCMT) were purchased from Sigma Aldrich and used without further purification. Experiments were performed using a 3.8-mM solution of MCMT in 1-propanol and a 5 mM solution of $W(CO)_6$ in dimethylformamide (DMF).

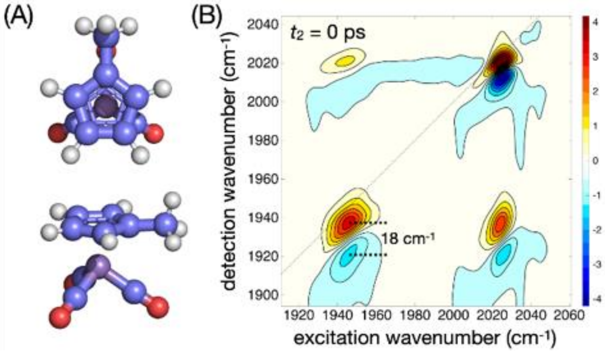

Figure 4-1. Methylcyclopentadienyl manganese tricarbonyl (MCMT) structure (A) and the 2D-IR spectrum in 1-propanol solution at t_2 = 0 ps (B). The anharmonicity of each mode is 18 cm^{-1}.

All 2D-IR spectra presented in this paper were collected using a pump-probe geometry 2D-IR spectrometer,[57, 118] which has been described in detail previously. Briefly, a Spectra-Physics Solstice Ace amplifier generating 100 fs, 4.2 mJ, 800 nm pulses at a 1-kHz repetition rate was used to pump an optical parametric amplifier (OPA, Light Conversion TOPAS-Twins). The resulting signal and idler pulses generated by the OPA were combined using an AgGaS crystal in a home-built collinear difference frequency generation (DFG) stage to generate 8 μJ mid-IR pulses centered near 5000 nm. About 95% of the generated IR was sent into a germanium acousto-optic pulse shaper (PhaseTech Spectroscopy) to produce the phase-controlled excitation pulse pair with a maximum total pump power of 3.5 μJ, and the remaining ~5% was used as the probe. The pump and probe pulses were compressed to about 100 fs. The pump pulses were compressed using the pulse shaper while the probe was compressed by matching the dispersion with a combination of calcium fluoride and germanium windows. Pump and probe beams were focused by a 15-cm effective focal length parabolic mirror at the sample position, and the probe was detected using a 0.3 m spectrograph (Horiba-Yvon, iHR320) equipped with a 64-pixel HgCdTe (MCT) IR detector array.

Each 2D spectrum is recorded at a fixing waiting time (t_2) delay while scanning t_1 from 0 to 5 ps with 25 fs time steps and a rotating frame wavenumber set at 1700 cm^{-1}.[118] To separate rephasing ($\mathbf{k}_R = -\mathbf{k}_1 + \mathbf{k}_2 + \mathbf{k}_3$) and nonrephasing ($\mathbf{k}_N = \mathbf{k}_1 - \mathbf{k}_2 + \mathbf{k}_3$) responses and to remove scattering, a three-phase-cycle sequence was used with three different relative phases (referred to as *A*,*B*, and *C*) between the excitation pulses and the probe pulse[61, 119]: $A: \phi_1 = 0, \phi_2 = 0; B: \phi_1 = 0, \phi_2 = \frac{1}{2}\pi; C: \phi_1 = 0, \phi_2 = \frac{3}{2}\pi$, where the subscripts 1 through 3 refer to the two pump fields and the third probe field. Raw spectral data was windowed using a Hann function and zero padded.

4.3 Experimental methods

4.3.1 Vibrational assignment using DFT, FTIR and 2D-IR for MCMT

The linear FTIR spectrum of MCMT in 1-propanol shows two strong absorption peaks in the metal carbonyl stretching band near 2000 cm^{-1}. The symmetry of tripods generally leads to the observation of two IR active bands with a high frequency symmetric stretch of all three CO ligands and a lower frequency band composed of the nearly-degenerate anti-symmetric stretch mode and out-of-phase symmetric stretch mode of the three carbonyls. As is well established with methyl-substituted-arene-coordinated metal carbonyls, the electronic orbital overlap is optimized when the CO ligands eclipse one or more of the methyl-bound carbons of the Cp’ ring.[120] This symmetry can be disrupted by solvent interactions, which we have included in density functional theory (DFT) calculations only at the level of a continuum solvent. The calculated structure of the MCMT complex demonstrates the expected partially-eclipsed conformation (**Fig. 4-1A**). DFT calculations used the B3LYP functional with a 6-31+G* basis on each of the light atoms and the LANL2DZ effective core potential on the Mn atom. The bulk solvent effects of 1-propanol were included using the polarizable continuum model in Gaussian 09. DFT calculations predict three CO stretching modes with (unscaled) frequencies of: 2061.96, 1971.16, and 1970.29 cm^{-1}.

The FTIR spectrum (see Supplementary Materials, SM) of MCMT in 1-propanol shows carbonyl stretching bands at 2020 and 1936 cm^{-1}. The second derivative spectrum is also consistent with a single contribution at the lower frequency band. The full width at half-maximum (FWHM) of the symmetric stretch mode is 8 cm^{-1} and the asymmetric band is about twice as broad, with a FWHM of 16 cm^{-1}.

4.3.2 Using Phase Cycling to Separate Rephasing and Nonrephasing Spectra

There are several advantages to using a pulse-shaper-based 2D-IR spectrometer, as it is straightforward to collect data while cycling the phases of the pump phases, and scanning with a rotating frame.[118] While a π phase shift phase cycling can be used for incoherent scatter subtraction, phase shifts in fractions of π have been demonstrated in a scheme to obtain complex rephasing and nonrephasing spectra.[61, 117, 119] Spectra along ω_3 are collected in the frequency domain. Causality is enforced with the application of a Fourier transform of a spectrum into the time domain, with a time axis of t_3, removal of the data at negative time delays in t_3, and the application of an inverse Fourier transform to obtain the complex frequency-domain spectrum.[61, 78] Not only can we separate the rephasing and non-rephasing signals using phase cycling, this method can help us reduce stationary scatter that is independent of the relative phase.[121] In a pump-probe geometry 2D experiment, the phase difference between the signal and the local oscillator (LO) is fixed as both interactions occur with the probe pulse. Thus, the phase of the signal depends only on the phase difference between the first two pump pulses ϕ_1 and ϕ_2.

$$\phi_{sig} = \mp(\phi_1 - \phi_2) + \phi_3 - \phi_{LO} = \mp(\phi_1 - \phi_2) \tag{4.4}$$

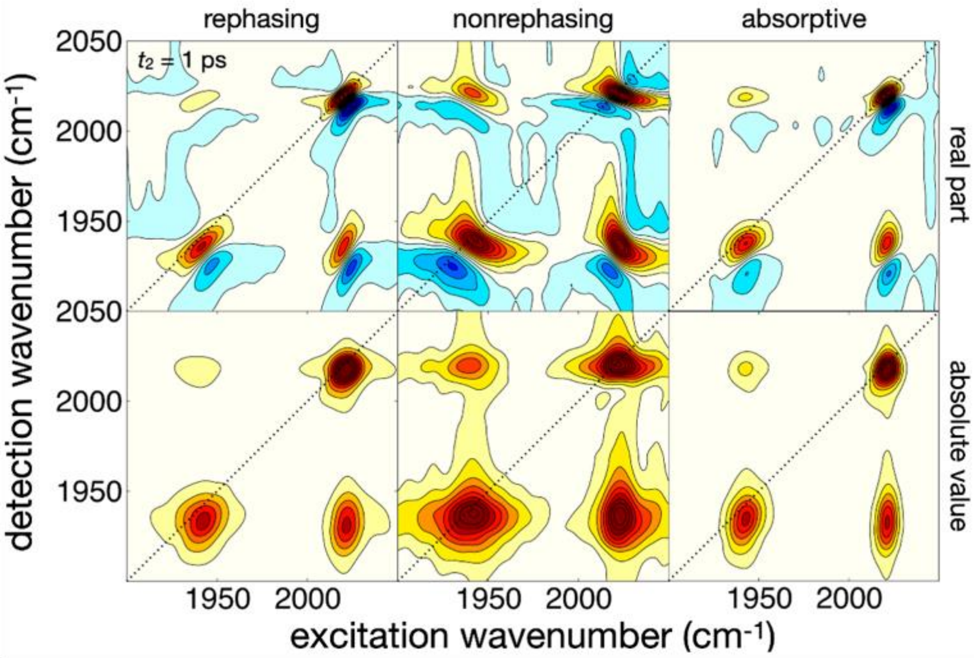

Figure 4-2. Methylcyclopentadienyl manganese tricarbonyl (MCMT) 2D-IR spectra at 1 ps waiting time obtained using phase cycling to separate the rephasing and nonrephasing Liouville space pathways. From top to bottom: real part, absolute value; from left to right: rephasing, nonrephasing and absorptive spectra, respectively. Notice that for the real and imaginary columns, red (low temperature color) represents ground state bleaching (GSB) and stimulated emission (SE), and blue (high temperature color) represents excited state absorption (ESA)

Using a three-phase cycle sequence, the following transforming matrix equation defines the relationship between the three phase cycled signals (S_A, S_B, S_C), and the rephasing (S_{NR}), nonrephasing (S_R), and transient absorption (S_{TA}) signals:

$$\begin{bmatrix} S_A \\ S_B \\ S_C \end{bmatrix} = \begin{bmatrix} e^{i(\phi_{A1}-\phi_{A2})} & e^{i(-\phi_{A1}+\phi_{A2})} & 1 \\ e^{i(\phi_{B1}-\phi_{B2})} & e^{i(-\phi_{B1}+\phi_{B2})} & 1 \\ e^{i(\phi_{C1}-\phi_{C2})} & e^{i(-\phi_{C1}+\phi_{C2})} & 1 \end{bmatrix} \times \begin{bmatrix} S_{NR} \\ S_R \\ S_{TA} \end{bmatrix} \tag{4.5}$$

Rephasing and nonrephasing spectra (**Fig.4-2A,B**) can be separated by substituting the phase values set in this experiment and then inverting the transforming matrix.

The real part of the sum of the complex rephasing and nonrephasing signals is equivalent to the absorptive spectrum measured in the pump-probe geometry in the absence of phase cycling (**Fig. 2C**)[122]:

$$S_{ab} = Re[\tilde{R}_R(\omega_1, t_2, \omega_3) + \tilde{R}_{NR}(\omega_1, t_2, \omega_3)] \tag{4.6}$$

The expected spectral features and line shapes are exemplified in the set of 2D-IR spectra for MCMT shown in Fig. 2.

4.3.3 Comparison of Inhomogeneity index and CLS method without intraband coherence

Tungsten hexacarbonyl was chosen as the first model system to compare the agreement between the general CLS and II methods without other complicating factors. The FFCF (**Fig 3**) obtained from CLS and II for tungsten hexacarbonyl in 1-propanol solution are in good agreement, although the FFCF extracted from the CLS method needs to be scaled for comparison, and both are fit well with a single exponential decay with a time constant of ~1.5 ps, a typical value for a short alcohol.[123] In **Figs. 4-3**, **4-4** and **4-5**, in order to show intuitively the differences and similarities of FFCFs measured by different methods, we have scaled the CLS to force it to overlap the II-derived

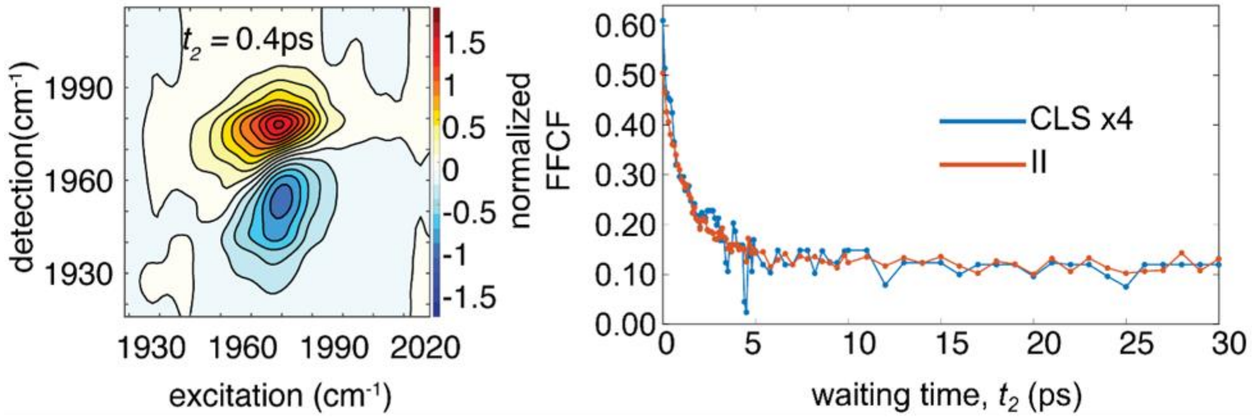

Figure 4-3.2D-IR spectrum of tungsten hexacarbonyl in 1-propanol at 0.4 ps waiting time (left), and (right) comparison of the FFCF obtained from the CLS versus that found with the II. The two methods yield the same FFCF decay dynamics. The FFCF extracted with the CLS method (arbitrary units) has been scaled to match the normalized FFCF extracted with the II method.

correlation function. The integration box size influences the early-time decay and y-intercept of the II-derived FFCF. This effect will be discussed below.

4.3.4 Comparison of Inhomogeneity Index and CLS methods with intraband coherence

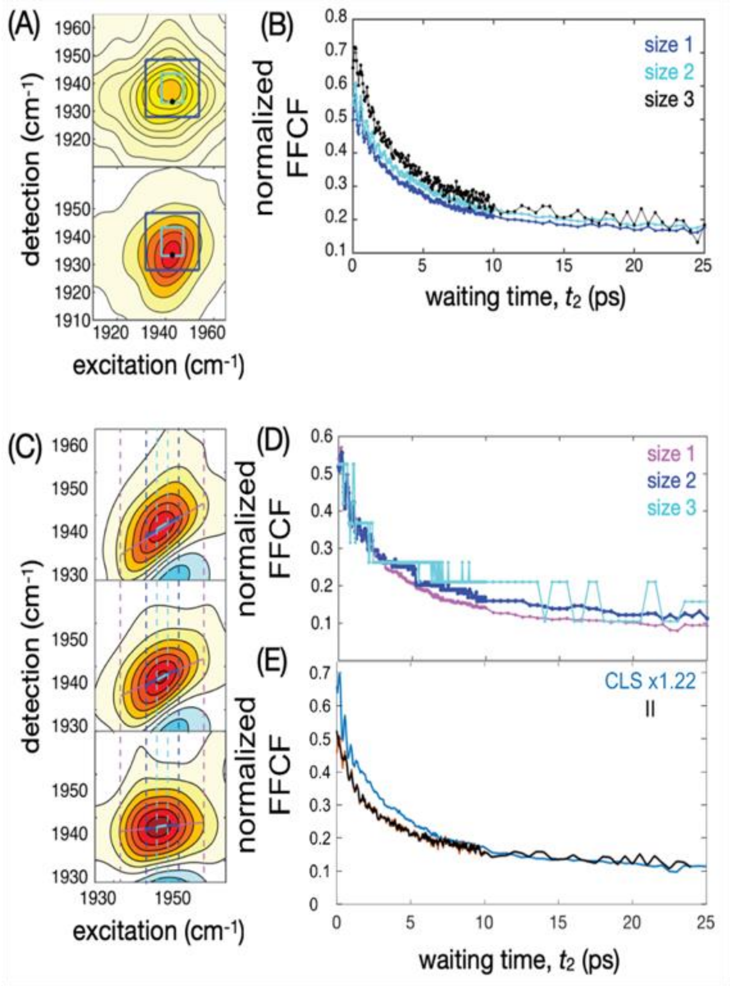

Figure 4-4. FFCFs for Cp’Mn(CO)$_3$ in 1-propanol obtained using the inhomogeneity index (II) and center line slope (CLS) with integration regions of various sizes for the lower frequency degenerate asymmetrical stretch band. (A) Absolute value of nonrephasing (top) and rephasing (bottom) spectra for the antisymmetric band at t_2 = 1 ps. Different colored boxes indicate the integration regions: 35x61 points (blue), 15x31 points (cyan), and a single point (black). (B) FFCFs for the asymmetrical band with the different integration regions. The y intercept of the calculated FFCF is influenced by the spectral anharmonicity (see discussion in the SI). (C) Absorptive 2D-IR spectra of the asymmetric band at various waiting times with the analyzed peak region indicated (34, 14 and 4 points, corresponding to purple, blue, and cyan). (D) FFCFs calculated from the CLS show the consequence of using differently sized analysis regions. (E) Comparison of FFCF obtained from CLS (blue) and II (red); reducing the coherence contribution in the II with a Fourier filter (see SI) is shown in black. The FFCF extracted with the CLS method (arbitrary units) has been scaled to match the normalized FFCF extracted with the II method.

Waiting time dependent 2D-IR spectra of MCMT in 1-propanol and the FFCF analyses for the asymmetric (**Fig. 4-4**) and symmetric (**Fig. 4-5**) bands show that the inhomogeneity index and the CLS spectral fitting analyses yield qualitatively similar results. A single exponential fit to the

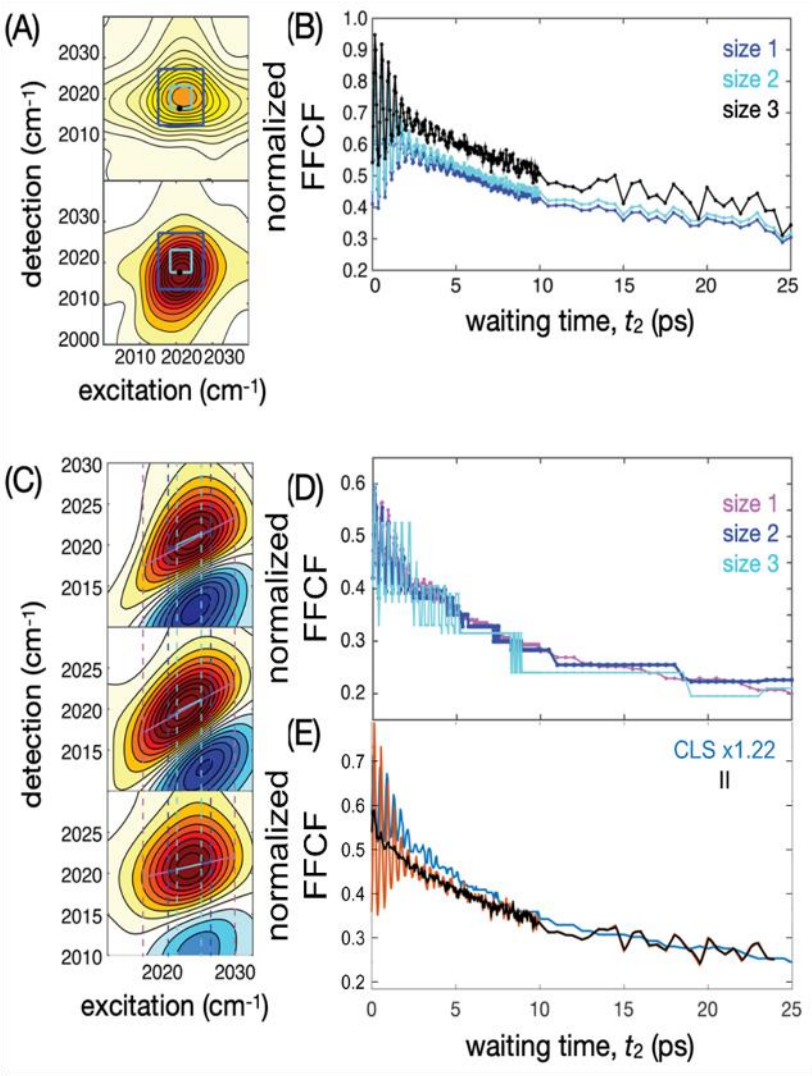

Figure 4-5. FFCFs for Cp'Mn(CO)$_3$ in 1-propanol obtained using the inhomogeneity index (II) and center line slope(CLS) with integration regions of various sizes for the high frequency symmetrical stretch band. (A) Absolute value of nonrephasing (top) and rephasing (bottom) spectra for the symmetric band at t_2 = 1 ps. Different colored boxes indicate the integration regions: 20x41 points (blue), 10x17 points (cyan), a single point (black). (B) FFCFs for the symmetric stretch band with the different integration regions. In addition to the size of the integration region, the FFCF obtained from the II method is modulated by intraband coherence oscillations. (C) Absorptive 2D-IR spectra of the symmetric band at various waiting times with the analyzed peak region indicated (19, 9 and 5 points, corresponding to purple, blue, and cyan). (D) FFCFs calculated from the CLS of the different analysis regions for the symmetric band. Coherent oscillations contribute to these FFCFs as well. (E) Comparison of FFCFs obtained from CLS (blue) and II(red); reducing the coherence contribution in the II with a Fourier filter (see SI) is shown in black. The FFCF extracted with the CLS method (arbitrary units) has been scaled to match the normalized FFCF extracted with the II method.

FFCFs obtained from the symmetric band using the different methods yields a decay time scale of ~7 ps (**Fig.4-5E**). This time scale is considerably slower than that found for $W(CO)_6$ in the same

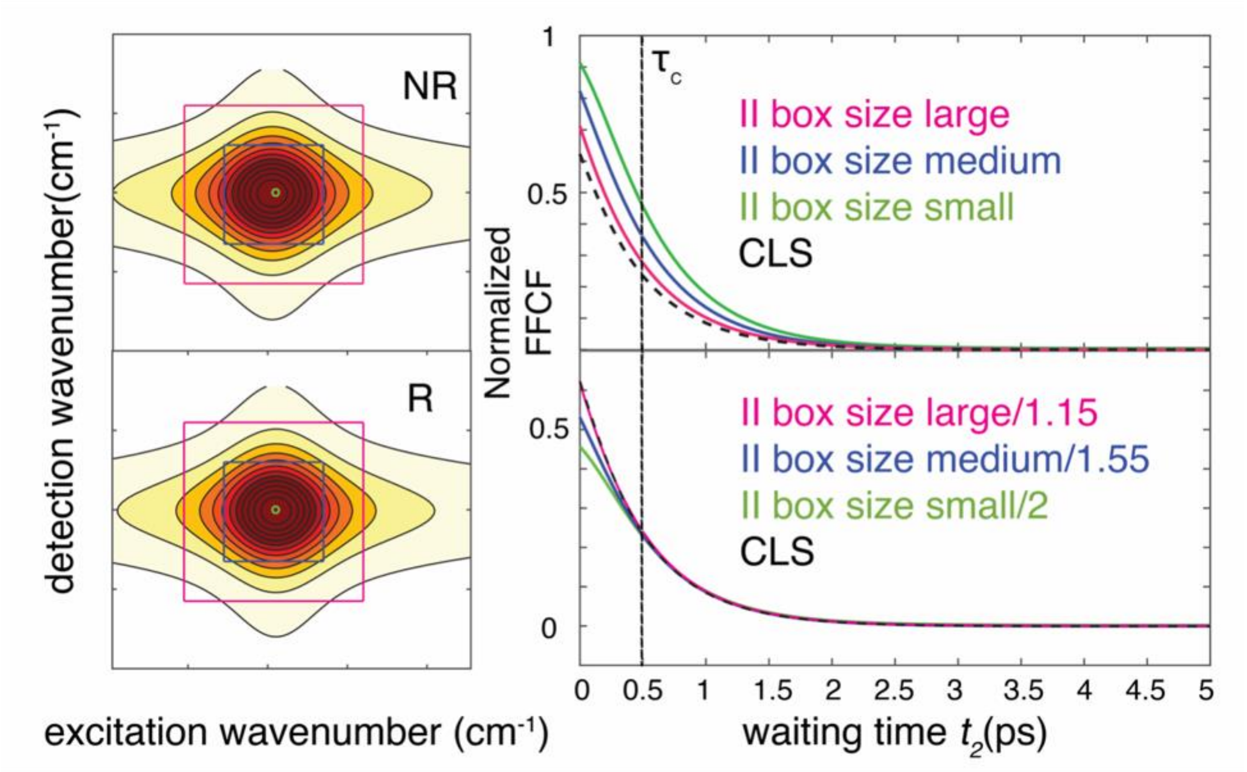

Figure 4-6. Calculated II and CLS with the response function of a three-level system. Different colors represent different integration box sizes and corresponding norm. FFCF; pink, blue, green represent large, medium and small integration box sizes. The black dashed line represents the FFCF calculated by CLS method. The FFCF traces calculated using different integration box sizes have a different y-intercept but similar decay constants.

solvent, and potential origins of the difference are discussed below. Further, oscillations are observed in the waiting time delay that arise from intraband coherences excited between the symmetric and asymmetric carbonyl stretches of MCMT and are thus observed to oscillate at the difference between the modes' frequencies.

The asymmetric band cannot be fit well with a single exponential decay and is instead fit with an offset biexponential decay. The slow decay term is almost the same using both methods, with wide error bars to the fit. Fixing the slow decay constant for both cases to be 5.85 ps, the average of the two independently fitted values, yields a fast decay term in the FFCF of 1.35±0.13 ps using the II analysis and 0.78±0.07 ps using the CLS analysis. This band consists of two nearly degenerate modes and we expect that energy transfer dynamics contribute to this difference, given that intramolecular vibrational energy redistribution (IVR) is typically very fast in complexes like this, occurring on a time scale of a few ps.[124, 125] We note that IVR between nearly degenerate modes is not readily measurable using 2D-IR, and has not been reported in any other system, but in cases where the energy gap is <100 cm^{-1}, IVR is routinely observed on timescales as short as 1 ps. Further, the fast component may include dynamical contributions from internal torsional dynamics, similar to our previous observations in the η^6-arene complex, benzene chromium tricarbonyl.[107, 126-128] Many tripod complexes have low barriers to internal rotation, introducing conformational change as a source of spectral diffusion.[129] Dynamics arising from internal flexibility are more challenging to observe distinctly in polar solutions where we expect a significant contribution from solvation, but such intramolecular motion contributes to the FFCF decay.

The oscillatory contribution to the FFCF from intraband coherences that occurs at the difference frequency between simultaneously excited modes appears to be much more pronounced when calculated using the II analysis, which may influence fitting accuracy but can easily be removed by Fourier filtering (**Fig 4-4** and **4-5**, black traces, details in the SM). There is a slight residue of oscillation remaining for the lower frequency band arising from the rephasing contribution that we do not Fourier filter. For the purpose of analyzing the FFCF, these oscillations are negligible in our fitting procedure, though they do reflect likely presence of coherence transfer, as we have recently identified in other metal carbonyl complexes.[130]

4.3.5 Comparison of effect of analysis region on the inhomogeneity index and CLS methods

In the absence of homogeneous broadening, the normalized FFCF at time zero should equal unity, and the y intercept measured in both methods is, at least in part, affected by homogenous broadening (cite 23,18). The intercept can also be influenced by fast dephasing and spectral diffusion caused by inertial solvent motion. To assess the information content that can be extracted with the II method in cases where the spectra are highly structured and geometric analyses are difficult to carry out, we compare the extracted FFCFs from IIID, analyzing the 2D peak over different spectral ranges for both the II and CLS methods. For the II analysis, the size of the integration region has no apparent influence on the time scale of the decay but alters the measured y-intercept. One explanation for this shift in the y-intercept with the II method arises from the weak anharmonicity of this system, as the area of the GSB feature sampled will include some contribution from the oppositely signed ESA feature, reducing the integrated amplitude. An analysis of the dependence of the II on the magnitude of the vibrational anharmonicity shows that the offset is proportional to the vibrational anharmonicity included in the response function of a three-level system (**Fig. 4-6**, see details in the SM). This effect occurs with large integration windows in any system with weak anharmonicity and is not limited to systems such as MCMT where intraband coherences can be observed.

While the II method appears to produce more accurate results with smaller sampling windows and produces an informative FFCF with slightly increased noise when sampling at a single point, in contrast, the CLS method fails to yield a high-quality FFCF in narrow spectral ranges (**Fig. 4-4D, Fig. 4-5D**). Further, the FFCF data extracted with the CLS method must be scaled to match the FFCF data extracted from the II method. While the II method produces a consistent y-intercept in the FFCF of $W(CO)_6$ in different solvents (see details in the SM), the CLS method requires inconsistent scaling factors in each of these samples. As a geometric method, the CLS is sensitive to any effect that broadens the measured peak in the excitation axis, including apodization windowing in the interferometric time delay and error in the interferometric time delay that causes ringing of the peak in the frequency domain. The CLS method requires more scaling across different solvents in these data (up to a scaling factor of 4) than the offset observed by varying the size of the integration region with the II method. To accurately determine the effects of homogenous broadening on the FFCF obtained with either of these methods and separate other effects such as motional narrowing, fast dephasing, and early-time contributions from spectral diffusion, additional methods including theoretical calculations and fitting of the linear spectrum should be used. However, in systems where the spectral diffusion timescale is of more interest than the homogeneous broadening term, as in this work, both the CLS and II methods agree and should be sufficient.

4.4 Conclusions

Neither the amplitude (inhomogeneity index) nor geometric method (center-line slope fitting) methods of extracting the frequency-fluctuation correlation function are new discoveries. This work does, however, present the first direct comparison of the two methods. While the theory underlying both approaches suggests that they will yield identical results given typical assumptions, the CLS still dominates the field as the standard method for measuring spectral diffusion. Indeed, for a pump-probe geometry 2D-IR spectrometer without field phase control, the CLS method is the easiest to implement since true phase cycling is difficult. Extracting the II in a pump probe apparatus requires at least a three-phase cycling scheme and further data process for implementation. Phase cycling is an additive process and does not reduce the signal-to-noise ratio, and overall measurement time is not appreciably increased. However, the CLS method fails for narrower line widths and atypical line shapes. For example, while the pump-probe geometry is the best suited for polariton systems to ensure that the same polariton mode is being pumped and probed, it is known that the absorptive line shapes of vibrational polariton modes do not match the spectral line shapes with which the CLS analysis is most used.[116] Further, the line width of vibrational polariton systems can be quite narrow, limiting the accuracy of this method in these systems.

Both tungsten hexacarbonyl and methylcyclopentadienyl manganese tricarbonyl are good candidates for use in a model vibrational polariton system, as they both have strong oscillator strengths and are soluble in various solvents at high concentrations. We find the II method to yield an almost identical result as CLS for tungsten hexacarbonyl, which has 3 degenerate modes. In MCMT, even after removing intraband coherence from nonrephasing spectra, a method-dependent difference in the faster time scale of the FFCF decay suggests that there are dynamics that are not captured in the simple theoretical foundations. Our results show that intraband coherences and fast IVR can manifest themselves in the fast time scale of the FFCF. However, for the purposes of analyzing the slower time scale present in the FFCF, both methods agree. Further experimental and theoretical development is needed to extract the fast time scales, particularly since it is not apparent why there should be differences between the CLS and II in the presence of intraband coherence and IVR. With these caveats, with the current relative ease of setting up a 2D-IR spectrometer in the pump-probe geometry with pulse-shaping and phase control, the inhomogeneity index method is a good candidate for measuring spectral diffusion in systems or spectra where the CLS method fails. We anticipate that this underutilized method will be more widely implemented in spectrometers with phase-control in the future.

4.5 Supporting information

4.5.1 Normalized Linear FTIR Spectrum of MCMT

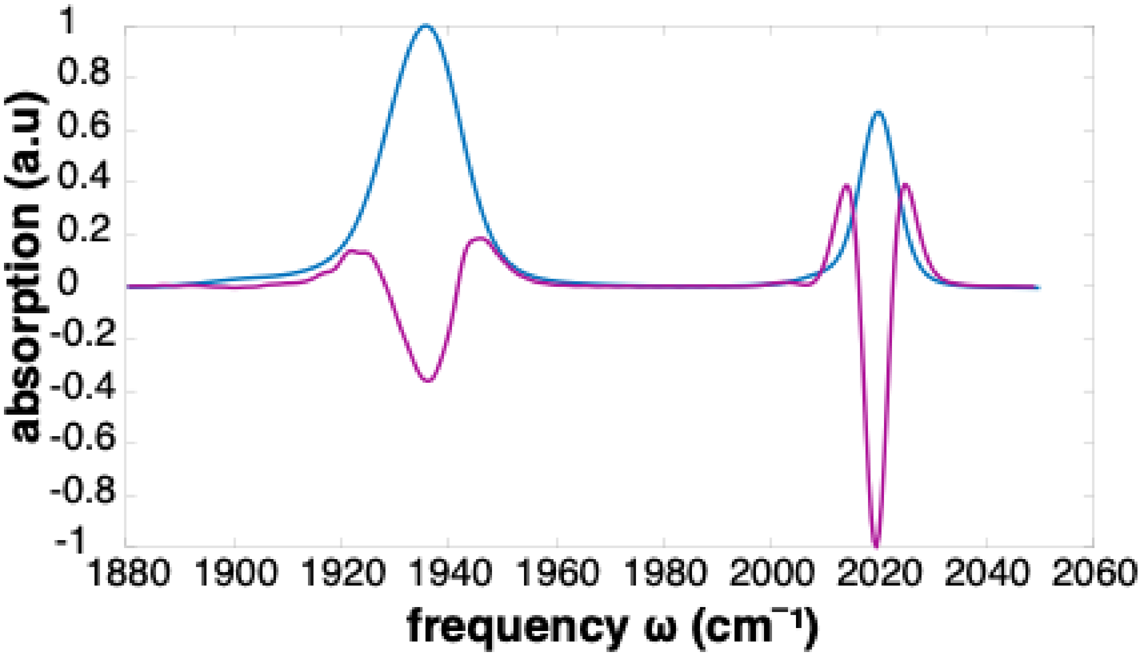

Figure 4-7. Normalized linear spectrum for MCMT molecule in 1-propanol. Blue curve is the normalized FTIR spectrum and purple curve shows the second derivative spectrum.

4.5.2 DFT calculation of MCMT in 1-propanol

The DFT calculation is performed using the B3LYP functional. The electrons on Mn were represented by the Los Alamos National Laboratory double zeta pseudopotential function (LANL2DZ) while for other atoms we used the 6-31+G* Gaussian basis set. A continuum solvent model is included using Gaussian's built-in SCRF. Three calculated relevant carbonyl stretching vibrational modes are listed in Table 4-1.

Table 4-1. Mode frequency list**:**

Mode	Frequency (cm^{-1})
1	1970.29
2	1971.16
3	2061.96

4.5.3 Simulation of FFCF in the Presence and Absence of Intraband Coherence

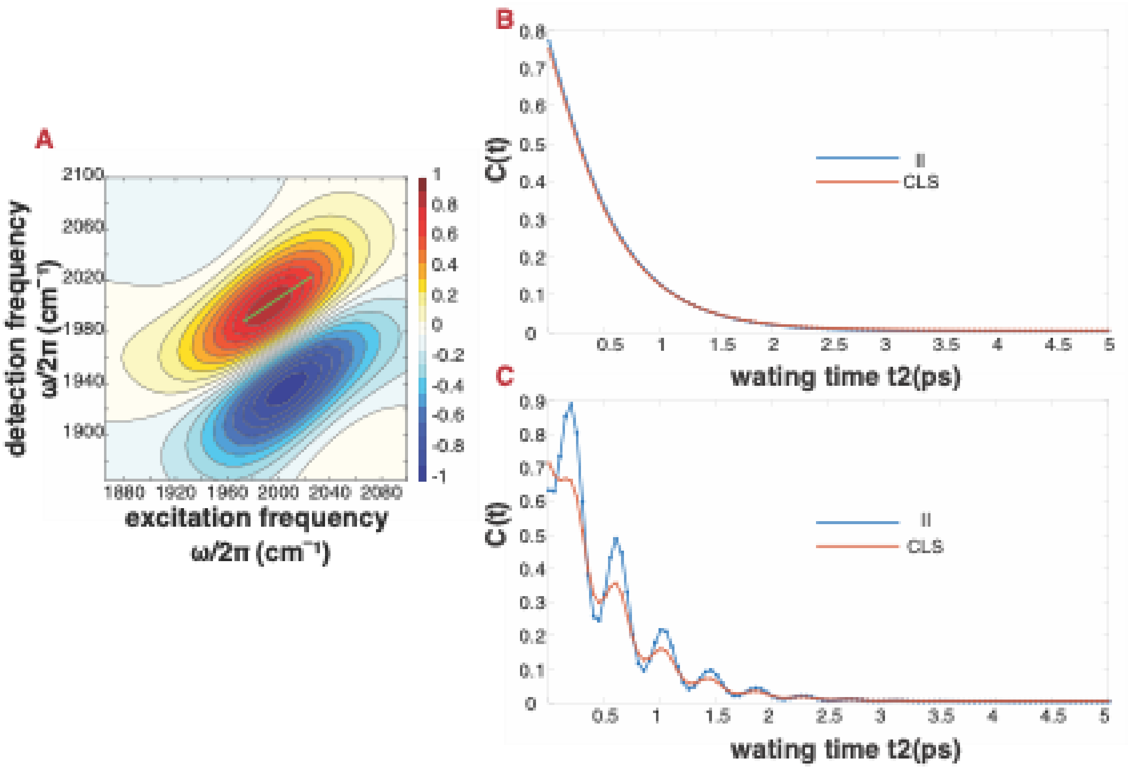

Figure 4-8. Simulation of 2D spectra and FFCF in the presence and absence of intraband coherence. A) Simulated 2D spectrum with superposed CLS. B) FFCF calculated using II and CLS methods almost perfectly agree in the absence of coherent modulations. C) With modulations arising from intraband coherence, the II and CLS calculated FFCF response differ. The CLS exhibits smaller amplitude modulations, consistent with our experimental findings.

Simulation of the diagonal peak (and it's excited-state absorption doublet) is done by assuming a 3-level system with a Kubo line shape function[131]:

$$g(t) = \Delta\omega^2 \tau_c^2 \times \left[e^{-\frac{t}{\tau_c}} + \frac{t}{\tau_c} - 1\right] \tag{4.7}$$

Rephasing and nonrephasing response functions are given by:

$$R_R = i\mu_{01}^4 e^{-1\omega_{01}(t_3-t_1)} e^{-g(t_1)+g(t_2)-g(t_3)-g(t_1+t_2)-g(t_2+t_3)+g(t_1+t_2+t_3)} \tag{4.8}$$

$$R_{NR} = i\mu_{01}^4 e^{-1\omega_{01}(t_3+t_1)} e^{-g(t_1)-g(t_2)-g(t_3)+g(t_1+t_2)+g(t_2+t_3)-g(t_1+t_2+t_3)} \tag{4.9}$$

Intraband coherence is added manually as an additional signal amplitude contribution that oscillates as a function of t_2. CLS and II are calculated using the same method as described in the main paper for the experimental spectra. CLS and II are both good methods for calculating FFCF in principle, but the II accentuates intraband coherence because the absolute value is not linear.

4.5.4 Simulated Inhomogeneity Index with Different Vibrational Anharmonicity

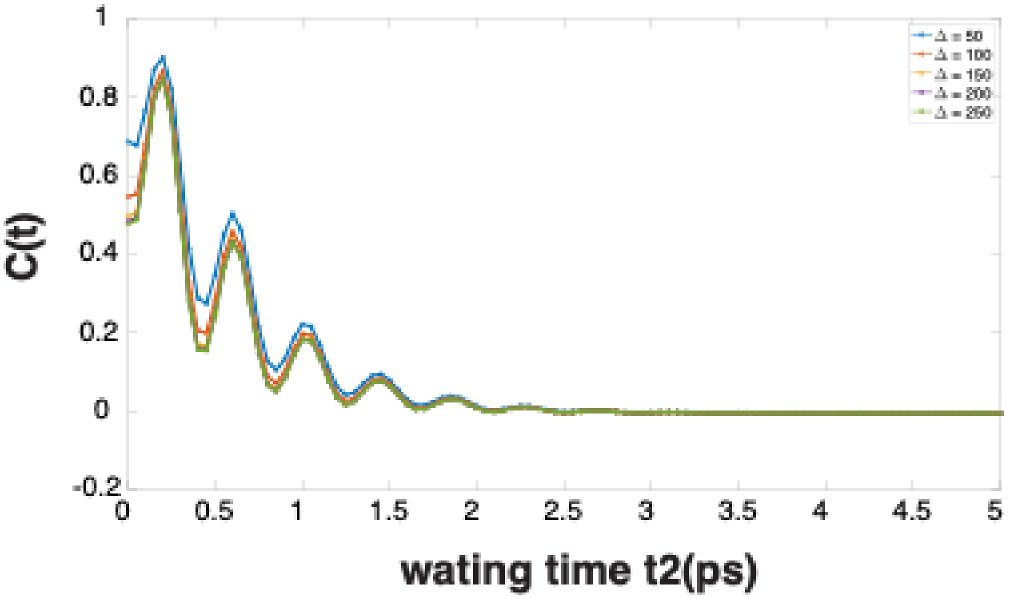

Figure 4-9. simulated II corresponding with different anharmonicity values 50,100,150,200,250 cm^{-1}.

With small anharmonicity (less than 150 cm^{-1} in this simulation), the FFCF intercept will change due to the interference between the excited state absorption and ground state beaching contributions.

4.5.5 Simulated Inhomogeneity Index with Different Integration Regions

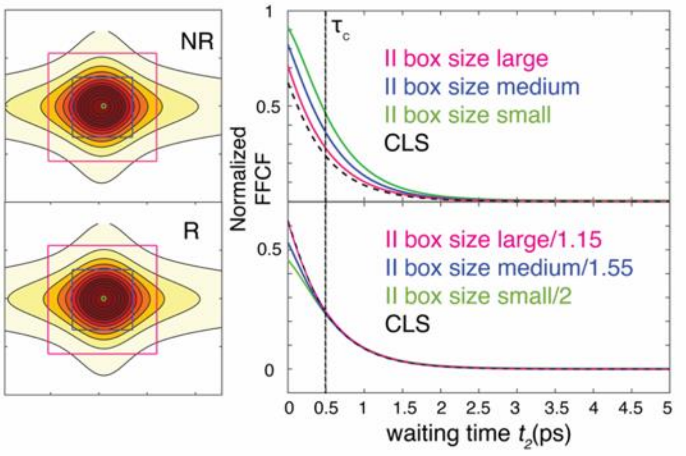

Figure 4-10. Simulated II with different integration sizes compared with CLS

The normalized FFCF calculated with CLS can be fit using a single exponential with a constant equal to the correlation time. Depending on the integration size, the normalized FFCF calculated by II with the smallest integration size recovers a more gaussian shape before the correlation time while CLS fails to do so. With larger integration size, the calculated FFCF using II will be identical to that recovered by the CLS method.

4.5.6 Fourier Filtering Coherences out of the Inhomogeneity Index

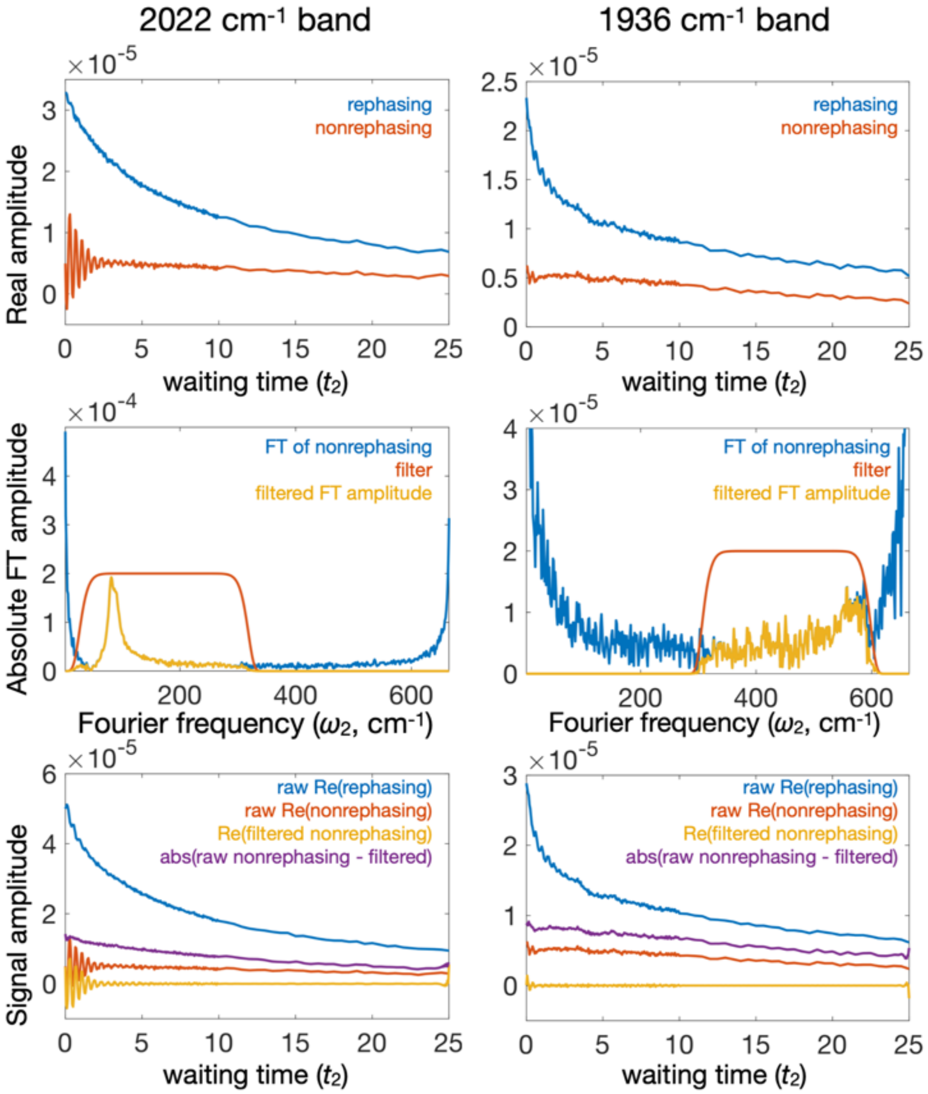

Figure 4-11. Full sequence of steps (described in the text) for Fourier filtering the nonrephasing signal in MCMT. We filter the complex amplitude, hence the high-frequency and low-frequency coherences appear at opposite signs due to the difference in the frequency difference in the t_2-dependent field-free Green function propagator.

Filtering the coherences in the inhomogeneity index can be done at the level of the individual signal contributions, rather than on the computed correlation function due to the essential lack of coherence in the rephasing signal. Moreover, because we are using a pulse shaper and have complete phasing information, it is advantageous to filter the complex nonrephasing signal instead of the absolute value amplitude as we have done in past work. **Figure 4-11** shows the steps used to filter the non-rephasing spectral amplitudes. First, we Fourier transform the nonrephasing signal to the frequency domain, and apply a super-Gaussian (with a power of 20) to select the oscillatory component. We then inverse Fourier transform the filtered signal back the time domain and subtract it from the original time-domain signal. Because the higher frequency (2022 cm-1) peak and the lower frequency peak (1936 cm-1) oscillate with frequencies of opposite sign, the 2022-cm-1 peak appears only around +90 cm-1, whereas the 1936 cm-1 peak appears at around -90 cm-1 (though its amplitude is quite small).

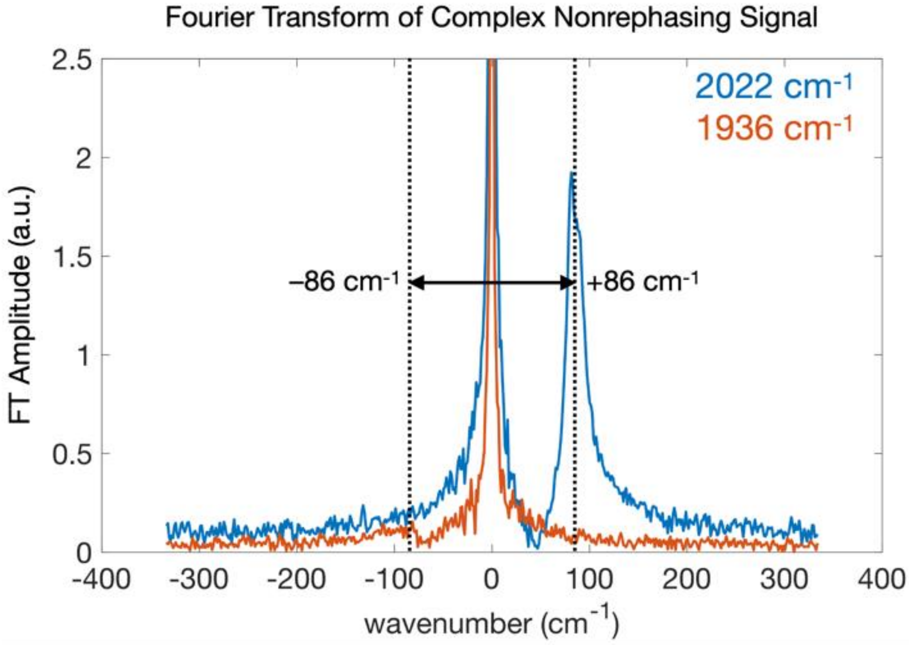

Figure 4-12. Fourier transform of the complex nonrephasing t2-dependent signal amplitude for the two fundamental transition of MCMT. The 2022 cm^{-1} appears with a positive frequency whereas the 1936 cm^{-1} peak appears at a negative frequency (though its amplitude is quite low).

The frequency position is shown in **Fig. 4-12** In all our previous work on vibrational intraband coherences, we analyzed the absolute value of the rephasing and nonrephasing signals, whereas here we are filtering the complex nonrephasing signal. In the absolute value case, the Fourier transform is symmetrical (because the time-domain input is real valued).

The comparison of the starting signals and the filtered nonrephasing signals are shown in **Fig. 4-13**.

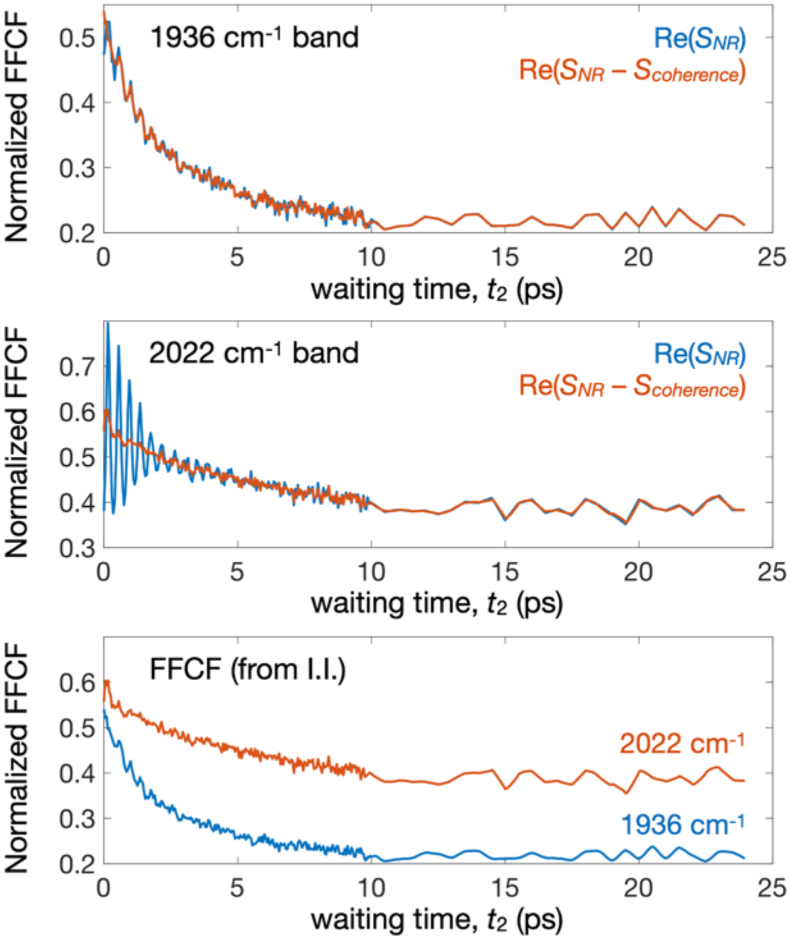

Figure 4-13. Comparison between the FFCFs obtained with and without filtering, as well as the two FFCFs obtained from the inhomogeneity index.

4.5.7 Comparison of $W(CO)_6$ in Two Different Solvents

In order to assess the degree to which the details of the 2D line shape influence the differences in the FFCFs obtained by either the II or CLS methods, we measured the 2D-IR spectra of $W(CO)_6$ in two additional polar solvents, dimethyl formamide and butyl acetate (**Fig. 4-14**). The total line width in DMF is somewhat broader than it is in butyl acetate, and the time scale for spectral diffusion is faster in DMF relative to butyl acetate. The key observation is that for the case of butyl acetate, the CLS and II are indistinguishable in amplitude, and there is no need to scale the FFCF from the CLS to overlap that obtained from the II. By contrast, in the DMF case, we do need to scale the FFCF from the CLS by more than a factor of 3 to make it overlap the FFCF from the II. We note that the line shape in the butyl acetate case resembles those produced by simple model response functions, whereas in the DMF case there is a more complex shape, which results in a smaller overall center line slope. The waiting time dependence of the two FFCFs, however, has essentially the same temporal dynamics. We do observe the initial value of the correlation to be different even with the two FFCFs scaled to overlap.

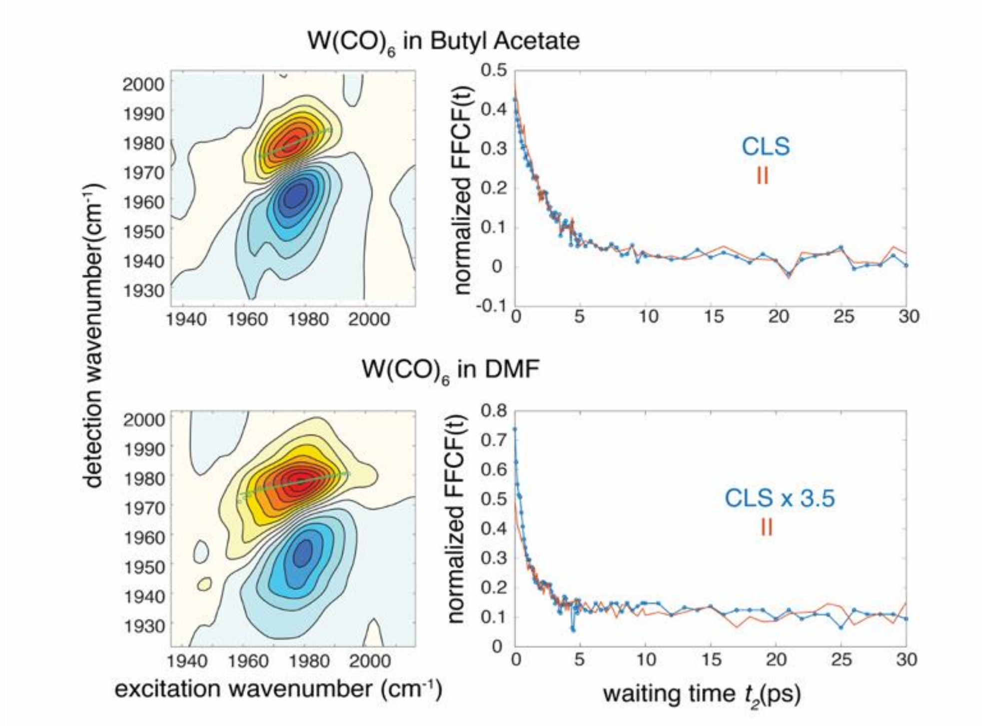

Figure 4-14. (left) Absorptive 2D-IR spectra of $W(CO)_6$ in butyl acetate and dimethyl formamide. (right) Normalized FFCFs obtained using the CLS and II methods. In the butyl actetate, where the line shape exhibits a particularly simple form, the two FFCFs agree without any scaling. In DMF, like the example of propanol in the main manuscript, there is a more complex shape along the detection axis for the fundamental transition, the FFCF obtained using the CLS needs to be scaled by a factor of more than 3 to overlap the FFCF from the II.

Chapter 5 Isolate Polaritonic 2D-IR Transmission Spectra

The work presented in this chapter has been published in the following paper:

Rong Duan, Joseph N. Mastron, Yin Song, and Kevin J. Kubarych , "Isolating Polaritonic 2D-IR Transmission Spectra", J. Phys. Chem. Lett. 2021, 12, 46, 11406–11414

https://doi.org/10.1021/acs.jpclett.1c03198

5.1 Introduction

Strong coupling between electronic states of matter and resonant optical cavities has played a key role in the development of novel states of quasi-particles, such as Bose-Einstein condensation[132] and lasing in exciton-polaritons.[133, 134] Very recently there has been a sharp growth in chemical applications of strong coupling, led by the discoveries of Ebbesen *et al.* that chemical reactivity can be altered by vibrational strong coupling.[14, 135-139] Infrared spectroscopy of vibrational strong coupling offers direct access to the polaritonic states, and ultrafast pump-probe or 2D spectroscopy enables determination of relaxation and dephasing in these novel hybrid light-matter states.[112, 115, 140-148] The promise of cavity controlled chemistry is sufficiently great that intense investigation is clearly warranted.[149-160]

When N molecules are resonantly coupled to a cavity mode, the eigenstates of the composite system consist of two highly delocalized, collective states that carry both photonic and matter character.[161, 162] These zero detuning polaritons are separated in energy by the so-called vacuum Rabi splitting, which is proportional to the scalar product of the transition dipole moment and the cavity wave vector, as well as the square-root of the number of molecules in the cavity. In addition, there are N-1 "dark" states, that resemble the uncoupled molecules (also referred to as the "bare molecules" to indicate a cavity-free condition). Because the cavities required to support a mid-IR wavelength are at least $\lambda/2$, N is typically very large ($>10^{10}$), leading to a large number of dark states relative to the two polaritons. However, the polaritons have a very large oscillator strength due to the participation of N molecules and the cavity mode. A quantitative description of the interaction of the polaritons and the dark states is central to understanding vibrational polariton relaxation and dephasing, as well as the mechanisms by which chemical reactions can be controlled.[143, 149, 163-165] In addition to the dark states, there is also a population of "uncoupled" molecules that do not participate in the delocalized polariton due to their spatial position along the cavity at regions of low field mode amplitude (see discussion in the SI). In terms of frequency, both the dark and uncoupled molecules are essentially indistinguishable from ordinary molecules in the absence of a cavity, though it remains to be determined if the dark states are distinct dynamically from the cavity-free bare molecules.[112, 143, 166]

5.2 Background correction presented by other people

In the sodium nitroprusside (SNP) example, Grafton *et al.* present a method to subtract the "reservoir" 2D-IR spectrum due to the uncoupled molecules.[166] Using the response at a 25-ps waiting time (t_2) delay, which is longer than the cavity lifetime, they generate a reservoir-only spectrum by extracting two slices of the 2D-IR spectrum: one at an excitation frequency matching the bare molecule peak maximum, and the other at a detection frequency corresponding to the maximum in the 2D spectrum. The product of these two slices is a 2D surface that resembles the overall appearance of the 25-ps spectrum. This spectrum is then subtracted from the early waiting time (1 ps) 2D-IR spectrum of the cavity response, yielding a putative reservoir-subtracted 2D-IR spectrum. A similar analysis was also used to correct the pump-probe transient absorption spectrum.

This method of estimating a 2D spectrum is similar to assuming a purely homogeneous limit, though we are not aware of a precedent for constructing a 2D-IR spectrum by multiplying two slices at one waiting time delay. Khalil *et al*. found that SNP exhibits substantial inhomogeneous broadening as well as spectral diffusion on the same time scales as the polariton studies.[167] Subtracting the constructed homogeneous reservoir spectrum from earlier time 2D spectra, where inhomogeneous broadening leads to diagonally correlated line shapes, cannot capture the dynamic peak shape of the uncoupled molecules. Using a model response function, we show that the background-subtracted 2D spectrum reported previously results from this dynamic 2D line shape in the filtered uncoupled response (details are in the Supporting Information, SI). Nevertheless, the insight that it is necessary to subtract a background 2D response due to the uncoupled molecule is essential for obtaining the polariton response. Our approach takes into account the dynamic line shape by recording the 2D-IR spectrum of the cavity-free sample and multiplying the spectrum at each waiting time by the two-dimensional polariton transmission to account for the spectral filtering of both the excitation and the detection processes. We show below that this approach is capable of isolating the polaritonic 2D-IR response.

If one neglects the dark states, it is possible to view the polariton system as one oscillator coupled to one cavity mode.[161, 162] It is common to invoke an effective coupling that collects the electric dipole interaction as well as the square root of N dependence. A recent treatment by Herrera *et al*. includes explicitly the state dependent transition dipole moments of an anharmonic oscillator, to arrive at a set of energy levels of the polaritonic ladder beyond the first excited state

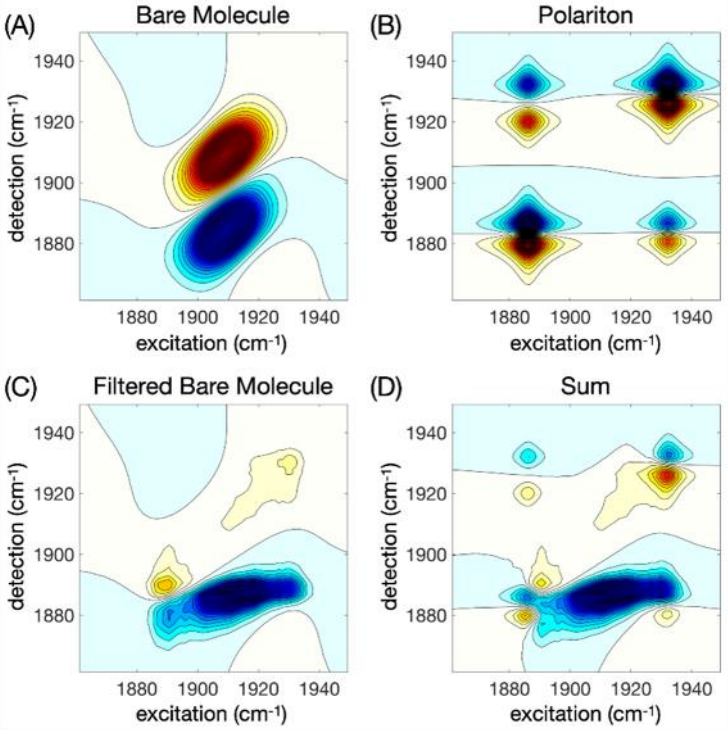

Figure 5-1. (A) Simulated 2D-IR absorptive response characteristic of sodium nitroprusside (SNP) based on the work of Khalil *et al*. **(B)** Polariton 2D-IR spectrum parameterized using the energy levels reported in Grafton *et al*. Note that the features corresponding to ground state bleach and excited state absorption have signs opposite to those of the absorptive bare molecule response. **(C)** Bare molecule response filtered by the polariton transmission (taken from data in Ref. 38). **(D)** Sum of the filtered background and the polariton response.

manifold.[168] With the energy level parameters determined using this method and reported in Grafton *et al*.,[166] we use conventional response functions[131] to produce a purely polaritonic 2D spectrum (**Fig. 5-1**). Keeping in mind that the signal phase in the polariton case is opposite that in the uncoupled background: ground state bleach (GSB) and stimulated emission (SE) pathways in the polariton lead to reduced transmission, whereas these pathways lead to increased transmission in the uncoupled response. The same logic leads to excited state absorption pathways with opposite signs in the polariton and uncoupled response. In our color scheme, the red features are increased transmission (reduced absorption), and the blue features are decreased transmission (increased absorption).

5.3 Isolate pure polariton spectra experimentally

Using the filtered 2D-IR spectrum (**Fig. 5-1**), either measured independently, or modeled using a simple response function, we can construct a 2D-IR spectrum for the cavity by adding the uncoupled background to the polaritonic response. We note that we currently do not know *a priori* how to weight the two contributions, but have developed an empirical method to correct our measured spectra (described below). Work by Xiong *et al*. shows that pump-probe spectra change with pathlength at constant concentration,[144] an effect that could be due to changes in the background contribution. The simulations here use weights chosen to resemble the characteristic 2D-IR spectra that are in the literature, as well as the many spectra we have recorded ourselves. The simulations show a striking resemblance to previously reported results. We do note one feature of the spectra that is clearly not reproduced in these simulations is the prominent cross peak at (ω_1 = 1956 cm^{-1}, ω_3 = 1977 cm^{-1}) corresponding to LP excitation and dark state fundamental detection. This feature could indicate evidence for the LP-to-reservoir energy transfer, and the sign is precisely what would be expected for excited state absorption, but the frequency corresponds to the $v = 0$ to 1 transition of the reservoir. Stimulated emission due to LP-to-dark state energy transfer would have the opposite sign (it would appear red in the present representation). We also find a cross peak at the UP-dark region, but again, it has the incorrect sign to be attributed to stimulated emission.

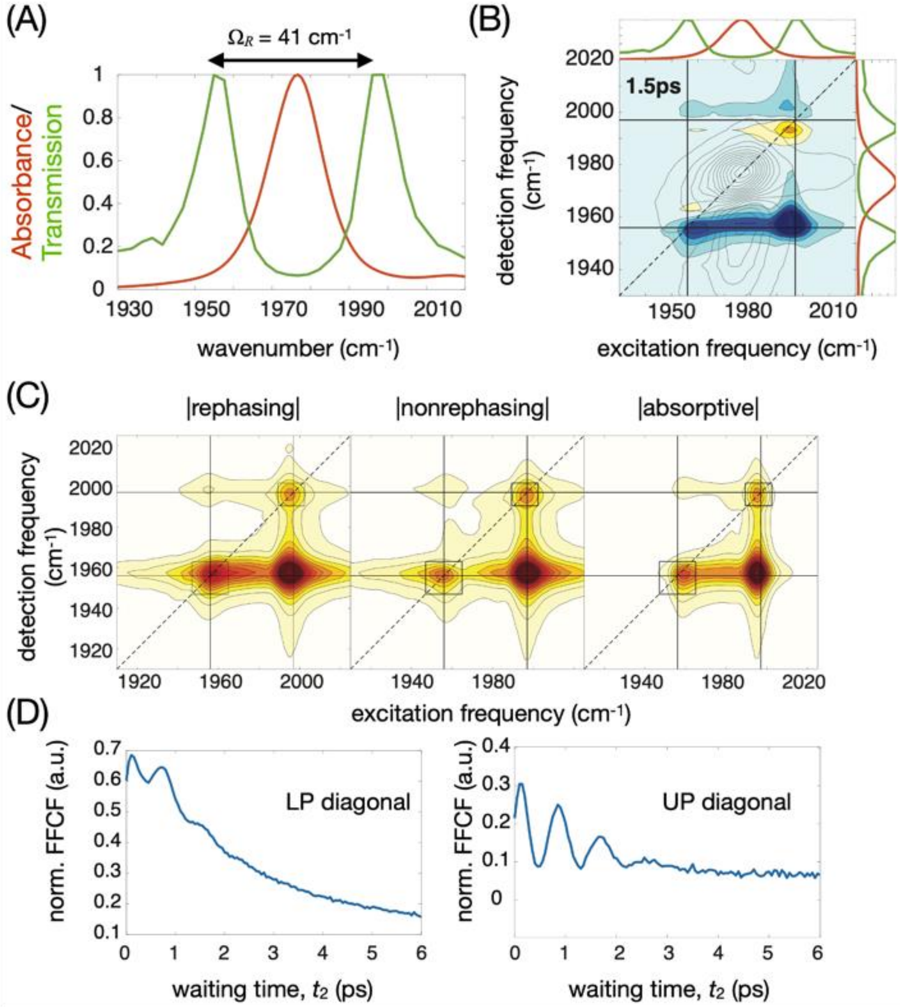

Figure 5-2. (A) Linear absorbance (red) of 2-mM $W(CO)_6$ in butylacetate in a standard cell, and transmission (green) of 40 mM $W(CO)_6$ in butylacetate in a resonant cavity (mirror reflectivity = 92%). Polariton bands are at 1956 and 1997 cm^{-1}; the bare molecule band is at 1977 cm^{-1}. **(B)** Absorptive 2D-IR spectrum of the cavity response (color) superimposed on the bare molecule response (gray), showing the significant overlap of the v=1 to v=2 excited state absorption and the lower polariton. Linear responses are shown along each axis for reference. **(C)** Absolute value rephasing, nonrephasing and absorptive 2D-IR spectra for the cavity; the signals are obtained using a 6 phase cycling scheme (SI). **(D)** Normalized frequency fluctuation correlation functions (FFCFs) for the LP diagonal (left) and the UP diagonal both indicate coherent modulation due to the nonrephasing contribution. The LP diagonal shows a pronounced spectral inhomogeneity that decays on the same time scale (2.4 ps) as the bare molecule measured outside of a cavity. This apparent spectral diffusion is due to the overlapping uncoupled background 2D-IR response.

Subtracting the uncoupled background 2D-IR requires measuring that response under conditions that are as similar as possible to the cavity-coupled conditions. Due to the typically high concentrations used in establishing strong coupling, there can be distortions to the 2D spectrum arising from solute-solute interactions as well as optical effects such as signal reabsorption. For both the bare molecule and polariton experiments we used ~40 mM $W(CO)_6$ in butyl acetate. To reduce the optical density and signal reabsorption, we used a 6-µm spacer for the bare molecule 2D experiment, whereas the cavity used a 25-µm spacer. In general, an ideal subtraction should be done with identical sample pathlengths and concentrations, but this is often difficult in practice

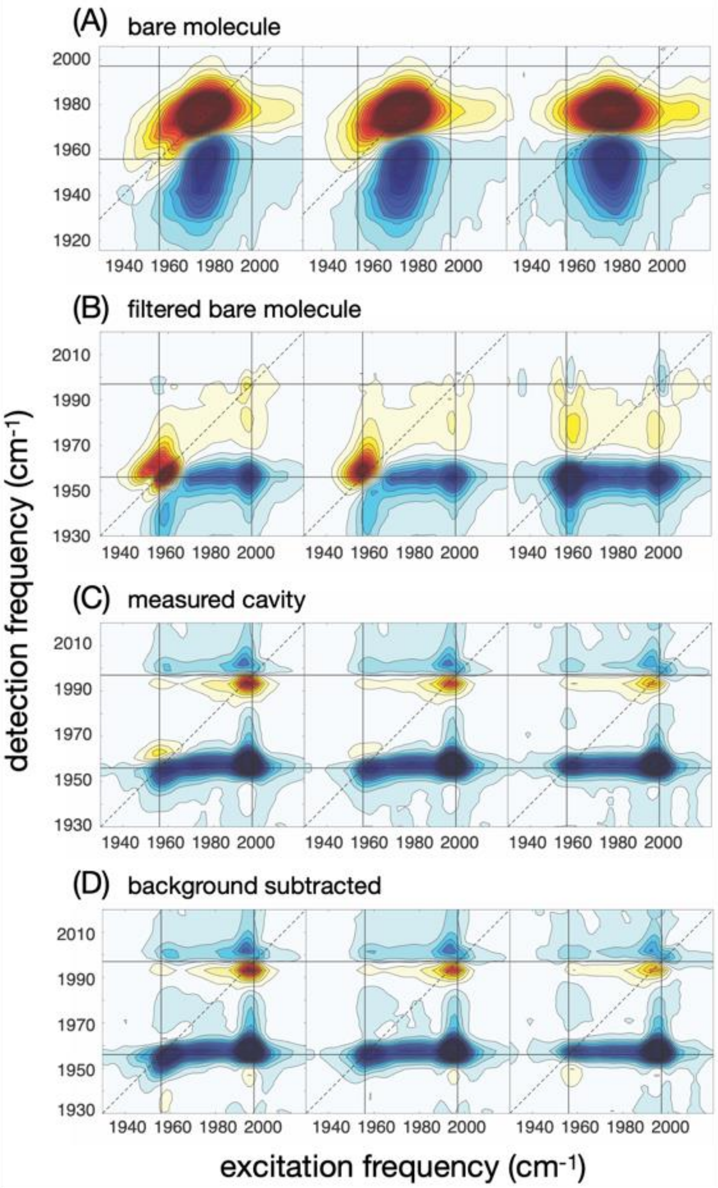

Figure 5-3. (A) Absorptive bare molecule 2D-IR obtained using 40 mM $W(CO)_6$ in butylacetate with a 6 µm pathlength cell (uncoated, 3-mm CaF_2 windows). All sets of three 2D spectra are shown for the same three waiting times (0.8, 1.5, and 30 ps). Dynamic changes of the line shape are due to spectral diffusion. **(B)** Absorptive 2D-IR response filtered by the polariton transmission (shown in Fig. 2A). **(C)** Measured absorptive 2D-IR spectra of the full cavity response (40 mM $W(CO)_6$ in butylacetate with a 25 µm pathlength; mirror reflectivity is 92%). **(D)** Background subtracted response (cavity – filtered bare molecule) shows the spectral signatures of the polaritonic ladder expected for an anharmonic oscillator coupled to a single harmonic cavity mode.

with the cavity lengths required to form the polaritonic system. The FTIR was recorded using a lower concentration sample (2.5 mM) in order to obtain an undistorted linear absorption spectrum. The 2D-IR experimental set up has been described previously, and is summarized in the SI.

The as-measured 2D-IR spectra of the cavity and bare molecule shows significant overlap of the 1-2 bare molecule response and the LP-detected 2D-IR signal (**Fig. 5-2B**). Absolute value rephasing, nonrephasing and absorptive spectra show prominent peaks at locations expected based on the linear transmission spectrum. Using the inhomogeneity index as a measure of the frequency-fluctuation correlation function,[169] we find coherent oscillations due to the impulsive excitation of both polariton bands, as well as a slow decay in the LP diagonal signal. This decay matches the FFCF decay of the bare molecule (2.4 ps), which arises from spectral diffusion. The polariton bands are purely homogenously broadened, and therefore cannot undergo spectral diffusion. This signature is, therefore, indicative of the uncoupled background 2D-IR signal.

Given the ability to construct 2D spectra of cavity systems by adding a pure polaritonic response to the filtered bare-molecule 2D-IR spectrum, it should be possible to isolate the pure polaritonic response experimentally. In our transmission polariton 2D measurement, the probe, serving as a local oscillator (LO), propagates within the cavity along with the signal, therefore the LO should have the same shape as the polariton transmission spectrum [$T(\omega)$]. The uncoupled bare molecule signal is modulated by the LO [$S_{\text{sig,bare molecule}} \propto 2\mathrm{Re}(E_{LO}(\omega_{det})E_{sig}(\omega_{det}))$]. The excitation pulses are filtered in a similar way. **Figure 5-3** shows the process of obtaining polaritonic spectra from the measured cavity response. We record the 2D-IR spectrum of the same sample in an ordinary cell without reflective cavity mirrors. The polariton transmission spectrum, $T(\omega)$, is measured in-situ using the pump and probe pulses (Fig. 2A). By multiplying the bare molecule 2D-IR spectrum by the polariton transmission in both excitation and detection dimensions [i.e.

$T(\omega_1)T(\omega_3)$], we obtain the filtered bare molecule response. To obtain the pure polaritonic contribution, we subtract the filtered bare-molecule 2D-IR spectrum from the measured spectrum of the cavity system (i.e. $S_{residual} = S_{cavity} - \alpha S_{filtered\ bare\ molecule}$). We use data with the same waiting time (t_2) to account for spectral shape changes that arise from the spectral diffusion within the inhomogeneously broadened band. Given that polaritons are immune to inhomogeneous broadening, we set the weight for subtraction such that we minimize the residual spectral diffusion in the LP diagonal peak (see SI for details). The resulting polaritonic 2D-IR spectra at various waiting times illustrate that the prediction based on two coupled oscillators yields a good correspondence with the measurements.

Several peaks in the polaritonic 2D spectrum exhibit oscillatory behavior with a frequency corresponding to the vacuum Rabi splitting (**Fig. 5-4)**, as is expected in 2D-IR spectra of coupled modes having narrow homogeneous linewidths. This oscillatory behavior is present in other 2D-IR spectra of polaritons,[112, 166] and it is well established that the diagonal peaks oscillate due to the non-rephasing pathways, whereas the cross peaks (and their red-shifted ESA doublets) oscillate due to the rephasing pathways.[170] The dephasing of the LP/UP coherence arises primarily from the cavity lifetime, which is estimated to be 2.7 ps based on 92% mirror reflectivity (see SI).

Besides the coherent oscillation, we also observe waiting time amplitude changes that reflect energy transfer between the polaritons, as well as ultimate relaxation back to the ground state. Our spectra show that the polaritonic populations decay on time scales that are far longer than the ~3 ps cavity lifetime. The UP diagonal peak exhibits biexponential decay with a fast time constant of 1.4 ps and a slow timescale of roughly 10 ps. Previous work by Xiong *et al.* and by Owrutsky *et al.* also show the same trend, where the slow component is expected to match the bare molecule lifetime, as the cavity signal has already decayed as that point. We attribute the 1.4 ps time constant to UP-to-LP population transfer because we see a rising component of the same time scale in the cross peak between UP and LP. By analyzing waiting-time dependent peak amplitudes, which largely reflect the population dynamics (**Fig. 5-4**), we can conclude qualitatively that for the regions where there is less overlap between the polariton and background spectrum (regions A and B of Fig. 4C), the residual polariton dynamics is not influenced by the background signal. For the regions of greater overlap, subtracting the background signal results in the LP diagonal (peak C in Fig. 4C) showing a reduction in the longer time decay constant while the LPUP cross peak's rise time constant becomes slower (D, Figure 4(C)). All fitting parameters for the curves shown in Fig. 4C are given in **Table S1**. Finally, the polaritonic state energies can be derived directly from the 2D spectrum at early waiting time, yielding an energy ladder diagram shown in **Fig. 5-4B**. In the case of ultrastrong coupling, which we do not have in the present case, there are reports of evidence of transitions between the dark and polariton manifolds.[171] For example a dark-to-UP overtone ($D_1 \rightarrow UP_2$ in our notation), would occur with an excitation frequency of 1977 cm^{-1} and a detection frequency of 2011 cm^{-1}. Though there may be amplitude at this spectral location, it is not significant compared with the polaritonic response. We have indicated the energy differences for any dark and polaritonic transitions in **Fig. 5-4B**.

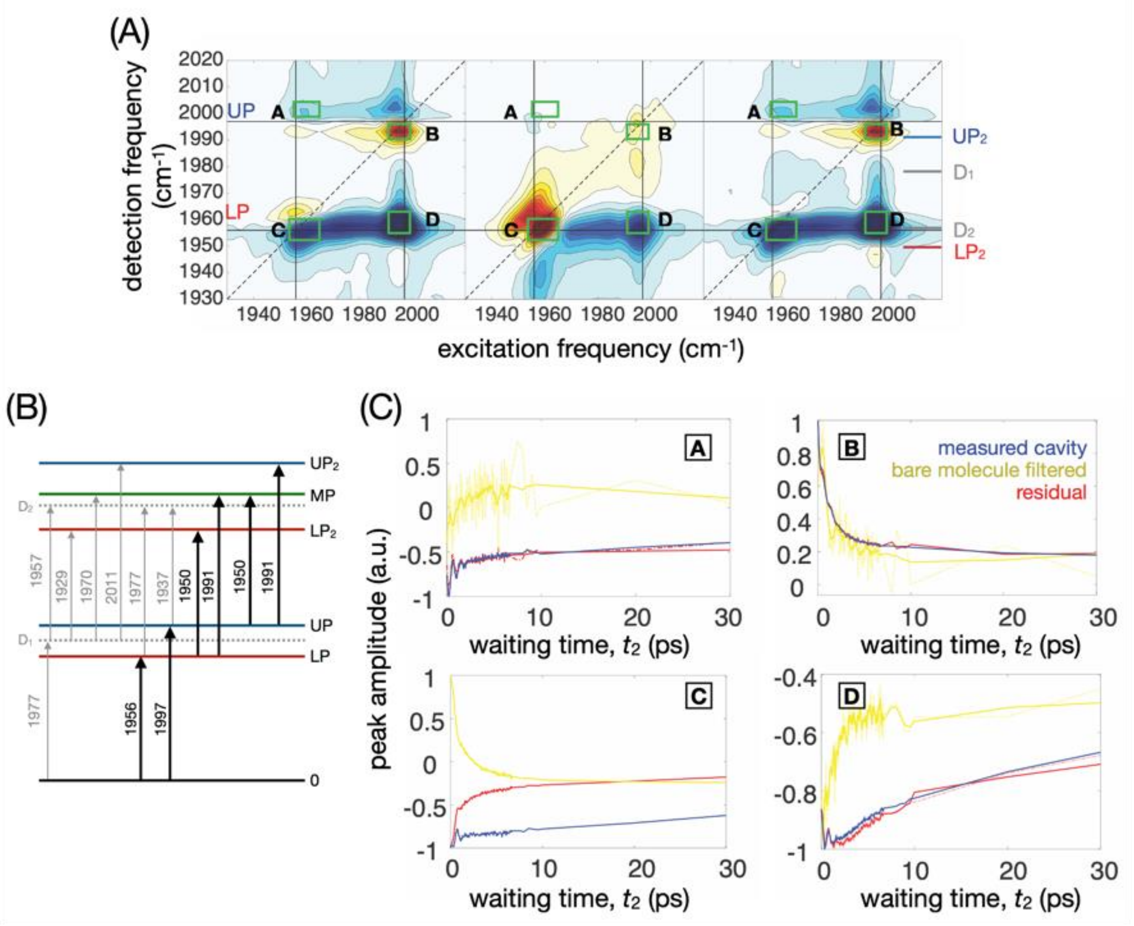

Figure 5-4. (A) Measured full cavity response (left), filtered bare molecule (middle), and subtracted residual (cavity – filtered bare molecule) at a waiting time of 0.8 ps. **(B)** Polaritonic ladder deduced from the 30 ps residual spectrum (shown in Fig. 3D, right). Gray arrows indicate transitions involving the uncoupled and dark states (D_1, D_2); bold arrows depict transitions between polariton states (LP, UP, LP_2, MP, and UP_2). **(C)** Waiting time dependence of the two diagonal (peaks C and B) and two main cross peaks (peaks A and D) as indicated in Fig. 4A. Peak A shows essentially negligible contributions from the uncoupled background, whereas the LP diagonal, peak E, shows a pronounced background contribution due to the uncoupled background. For peaks A, B and D, data are shown as moving averages (dark lines) and raw measured data (light lines); window sizes are 10 for peaks A and D, and 3 for peak F.

Regarding the role of dark states in the relaxation of polaritons, there should be two experimental signals associated with polariton-to-dark energy transfer. One feature would be a *v* = 1 to *v* = 2 ESA associated with excitation of either of the polaritons, which happens to coincide with the LP transmission. The other feature would be a stimulated emission from *v* = 1 to *v* = 0 in the uncoupled reservoir. Because that signal emits in the transmission minimum of the polariton spectrum, it will be more difficult to observe. In the subtracted spectrum, we observe a peak at (1956 cm^{-1}, 1977 cm^{-1}), corresponding to LP excitation followed by detection at the bare molecule fundamental. The sign of this LP/bare cross peak corresponds to an induced absorption (blue in our color scheme) instead of the expected stimulated emission feature (red in our color scheme). It is difficult to conclude whether this feature simply arises from the filtered bare molecule response, where it is rather prominent (**Fig. 5-3B**). The LP/bare ESA peak shape is elongated along the diagonal, which is not expected for a purely polaritonic response as the polariton features are not inhomogeneously broadened. If this feature is due to polariton-to-reservoir energy transfer, it is possible that the inhomogeneous broadening of the reservoir states would manifest as a frequency correlation. For the inhomogeneity to persist, the energy transfer to the reservoir must be faster than the spectral diffusion within the reservoir. Nevertheless, it is difficult to rationalize why the excitation frequency of the homogeneously broadened polariton would be correlated with the inhomogeneously broadened reservoir. From the bare-molecule 2D-IR we determine the spectral diffusion to occur on a 2.4 ps timescale, setting an upper bound on the energy transfer time scale. Unfortunately, it is not possible to conclude definitively that the diagonally elongated peak shape is due to energy transfer without observing the concomitant stimulated emission signal.

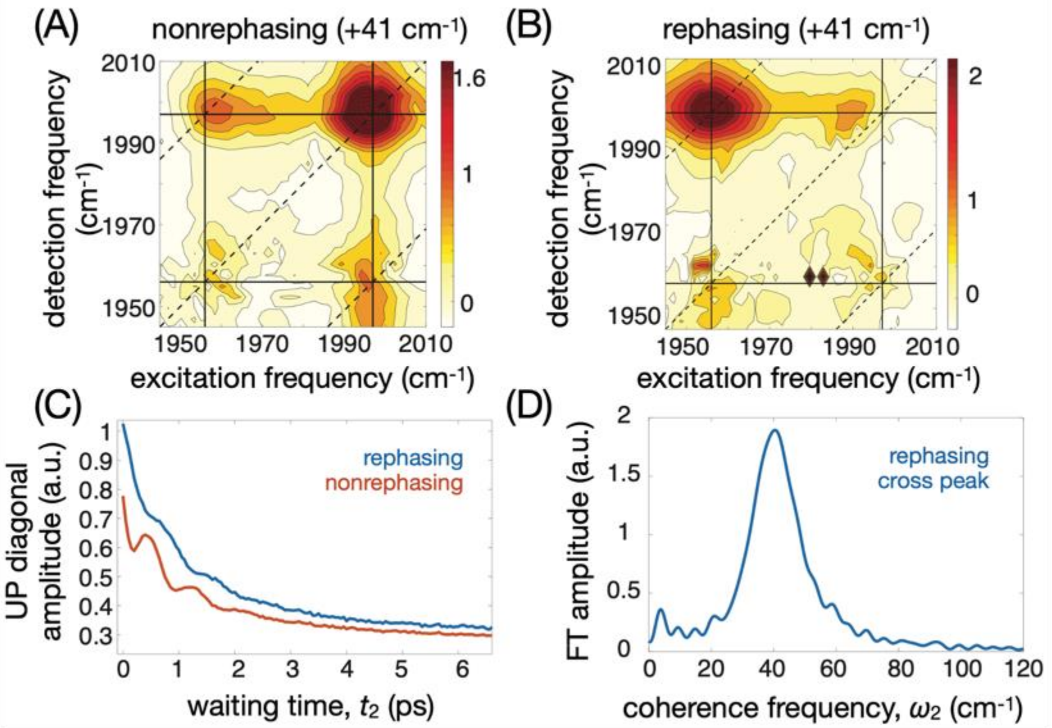

Figure 5-5. (A) Coherence map for the nonrephasing response shown at a frequency cut of +41 cm^{-1}. Because we analyze the complex rephasing spectrum, the coherence for the UP diagonal appears at positive frequency, whereas the LP diagonal appears at –41 cm^{-1} (negative frequency coherence maps are shown in the SI). **(B)** The rephasing coherence map at +41 cm^{-1}, shows the upper left cross peak oscillates (the lower right cross peak oscillates with a frequency of –41 cm^{-1}). **(C)** Full waiting time dependence of the UP diagonal peak for the rephasing (blue) and nonrephasing (red) responses. **(D)** Absolute square Fourier transform amplitude of the rephasing response at the LP/UP cross peak indicates a single peak at 41 cm^{-1}, with a width of roughly 15 cm^{-1}, corresponding to an exponential dephasing of ~3 ps (assuming a Lorentzian spectrum).

As mentioned above, and by others,[112, 140, 166] the coherence in the waiting time is a signature of a polariton system. As is expected for a single vibrational mode, the filtered bare molecule response does not exhibit any quantum beats. Fourier transforming the cavity response with respect to t_2 yields a coherence frequency, ω_2. Pulse shaping can be used either to isolate or suppress these coherent oscillations,[115, 166] and we have chosen to analyze them using coherence maps. Employing a 6 phase cycling (SI) scheme[172] enables direct measurement of both the real and imaginary parts of the rephasing and nonrephasing spectra. Due to the specific signs of the frequency of each pathway, this separation enables a greatly simplified coherence map that is readily assigned for each pathway. We show here (**Fig. 5-5**) the positive vacuum Rabi splitting

(+41 cm^{-1}), with the negative frequency maps shown in the SI. As expected, the coherence appears on the upper diagonal for the nonrephasing and on the upper cross peak for the rephasing responses. In the Frobenius spectrum,[173] obtained by summing over all excitation and detection frequencies (Fig. 5D), we find a single peak at the 41 cm^{-1} vacuum Rabi splitting, with a width of roughly 15 cm^{-1}, corresponding to an exponential dephasing of about 3 ps (assuming a Lorentzian spectrum), consistent with the ~3 ps calculated cavity lifetime (see SI).

5.4 Conclusion

We present a method of removing the polariton-filtered background 2D-IR spectrum that comprises roughly half of the signal amplitude in many cavity-based experiments. The dark state spectral amplitude arises from molecules located, for example, in low-field regions of the cavity, producing appreciable oscillator strength of the reservoir states. These features are inherent in vibrational polaritons, and care must be taken in interpreting polariton nonlinear spectroscopy without correcting for this potentially significant background contribution. Once corrected, the polariton 2D-IR response can be interpreted using the standard concepts of coherence, energy transfer and energy relaxation that have been developed in the multidimensional spectroscopy community.[103, 131] Compared with ordinary molecules, polaritons are immune to inhomogeneous broadening, thus signatures such as spectral diffusion suggest non-polaritonic contributions. Dynamical signatures of non-polaritonic contributions can aid in identifying processes such as energy transfer to and from the dark reservoir. These findings also suggest that nanophotonic resonances may offer a notable advantage due to the potential to achieve strong coupling with single molecules.[174, 175] While the approach we have demonstrated here can reduce the uncoupled background nonlinear response, for cases with more complex bare-molecule spectra, the method may not be sufficient. We propose that the most straightforward solution is either to (1) rely on the ultrastrong coupling where the polaritons are shifted very far from the bare molecule transitions, or (2) to ensure the active molecules are located in high-field regions of the optical cavity, thus reducing the contribution of the uncoupled molecules.

5.5 Supporting information

5.5.1 Illustration of spatial distribution of polariton eigenmodes

Cavity mode resonances arise due to the boundary conditions imposed by the mirrors. Because the coupling to the cavity is proportional to the field amplitude, molecules near the mirrors (or any nodes in higher-index optical modes) will experience reduced coupling. These molecules can be included in a Tavis-Cummings Hamiltonian[52] by simply making the coupling to the cavity depend on each molecule's longitudinal position in the cavity. The result is that the polariton eigenvectors have coefficients that follow the field (**Fig. 5-6**). The locations of the dark states also follow the field, but the uncoupled molecules are located near the mirror interfaces. The uncoupled contribution, as well as the dark states, are responsible for the substantial non-polaritonic background.

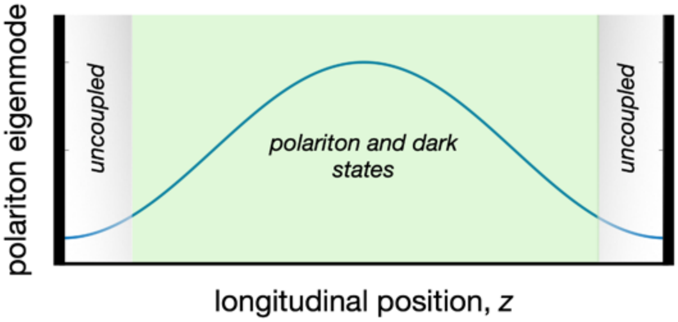

Figure 5-6: Eigenvector distribution of a polariton in a cavity. The blue line shows the squared modulus of the molecular part of the polariton eigenvector (i.e. $|c_j|^2$). Near the mirrors, there is little participation from molecules in both the polariton and dark state eigenvectors. In the regions of higher cavity mode field, there are dark states and the polariton states.

5.5.2 Experimental method: 2D-IR spectrometer and cavity fabrication

The 2D-IR experiment is performed using a pump probe geometry.[53-54] The Spectra-Physics Solstice Ace amplifier generates 100-fs, 4.2-mJ, 800-nm pulses at a 1-kHz repetition rate. This pulse train pumps an optical parametric amplifier (OPA, Light Conversion TOPAS-Twins). The OPA output is sent into a home-built collinear difference frequency generation stage using a $AgGaS_2$ crystal to generate 9-µJ mid-IR pulses centered at 5050 nm. Using a CaF_2 wedge, we direct 95% of the beam into a germanium acoustic-optic modulator-based pulse shaper (PhaseTech Spectroscopy) to produce the phase-controlled excitation pulse pair. The remaining 5% serves as the probe pulse. Both pump and probe pulses are ~100 fs. A 15 cm effective focal length parabolic mirror focuses the two beams at the sample position, and only the probe is detected using a 0.3-m spectrograph (Horiba-Yvon, iHR320) equipped with a 64-pixel HgCdTe (MCT) IR detector array.

2D spectra were recorded at a fixed waiting time (t_2) delay while scanning t_1 from 0 to 6 ps with 10 fs time steps and a rotation frame set at 1700 cm^{-1}. A 6 phase cycling scheme is used to separate the rephasing and nonrephasing spectra[172] while also allowing for subtraction of the scattered light. Raw data is windowed using a Hann function and zero padded to a computed spectral resolution of 0.8 cm^{-1}. 2D-IR spectra were collected at waiting time (t_2) points from -2 ps to 0 ps in steps of 500 fs, from 0 to 7 ps in steps of 50 fs, from 7 to 10 ps in steps of 500 fs, and from 10 to 30 ps in steps of 10 ps.

Cavity mirrors (coated by Universal Thin Film Lab) are coated with magnesium fluoride (MgF_2) on 25-mm diameter, 3-mm thick calcium fluoride (CaF_2) windows. The reflectivity at the region of interest is ~92%. The coarse cavity length was set using a PTFE spacer of known thickness, and then finely adjusted to shift the Fabry-Pérot transmission bands using a spectrometer. In terms of sample preparation for the experiments, the same concentration of $W(CO)_6$ (40 mM) was filled inside the 25 μm cavity for the polariton experiments and a 6 μm spacer was used for the bare molecule experiments.

5.5.3 Effect of spectral diffusion on long-time estimate of the uncoupled 2D-IR background

Due to inhomogeneous broadening and spectral diffusion, 2D-IR spectra of molecules in polar solvents typically exhibit dynamical line shapes that change as a function of the waiting time (t_2). We show here that this dynamical line shape causes the majority of the spectral features attributed to the polariton response in the work by Grafton *et al.* on sodium nitroprusside.[56] To simulate their results, we compute two 2D-IR absorptive spectra (using standard response functions),[57] one at an

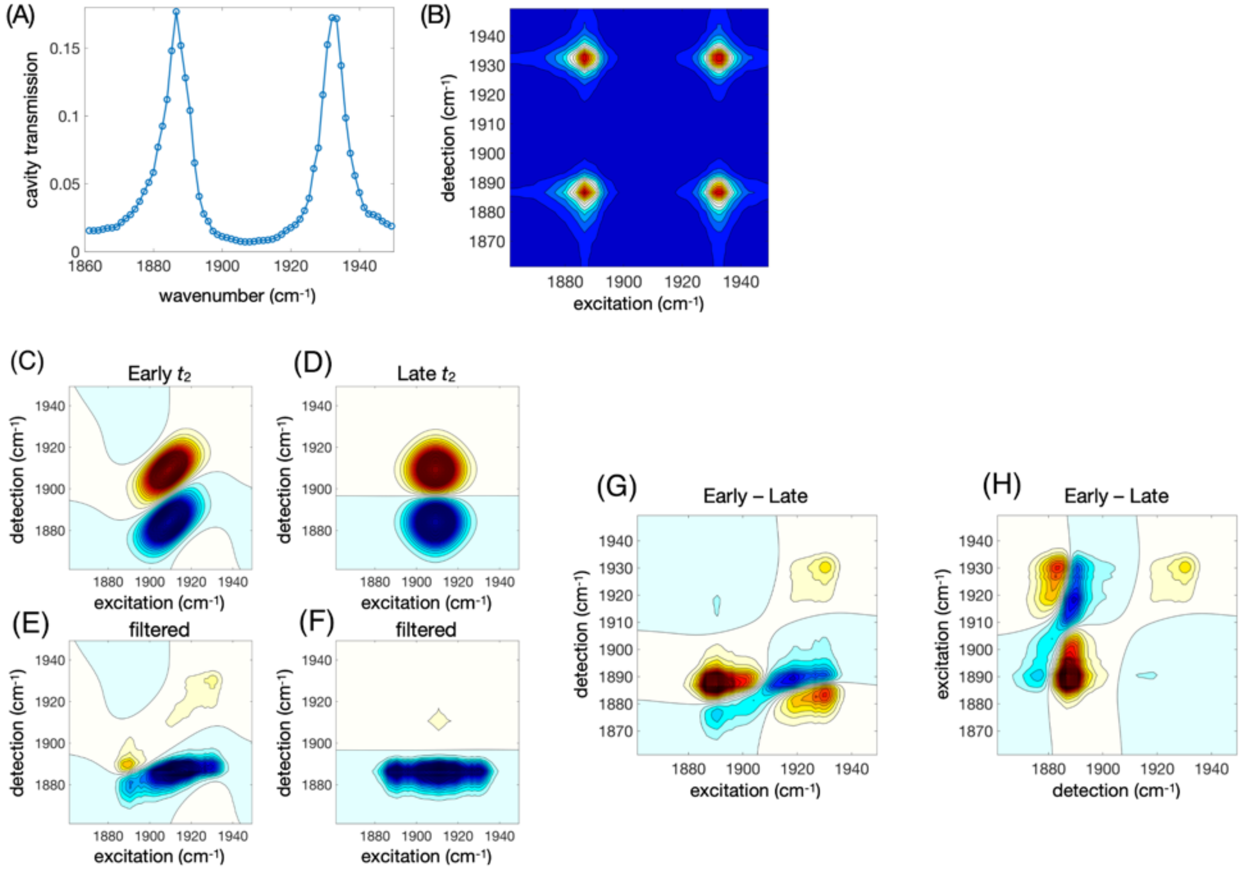

Figure 5-7.(A) Transmission spectrum (data extracted from Ref. 56) used to filter the simulated 2D-IR response. **(B)** 2D transmission filter. **(C)** Simulated early waiting time (t_2) absorptive 2D-IR spectrum resembling the results of Khalil et al. for sodium nitroprusside. **(D)** Simulated late waiting time 2D-IR spectrum. **(E)** Filtered early time 2D-IR spectrum. **(F)** Filtered late-time 2D-IR spectrum. **(G)** Late time, filtered 2D-IR spectrum subtracted from the early-time filtered 2D-IR spectrum. **(H)** Same difference spectrum plotted using the convention where the excitation and detection axes are swapped (for easier comparison with Ref. S5).

early waiting time (i.e. before significant spectral diffusion occurs) and another at a later waiting time when the response appears homogeneous (i.e. spectral diffusion is complete). We then filter these bare-molecule 2D spectra by the reported polariton transmission (data shown in **Fig. 5-7A** are taken from Ref. 56). Both 2D-IR spectra are multiplied by the filter function (**Fig. 5-7B**) to produce two filtered bare-molecule responses (**Fig. 5-7B,D**). We subtract the late time response from the early time response, to give the residual spectra (**Fig. 5-7E,F**), which resemble the polariton spectrum reported in Ref. S5.

5.5.4 Detailed background subtraction process

We have devised an approach for removing the background uncoupled 2D-IR response by using the spectral diffusion as a feedback signal. Because we have used a 6 phase cycling scheme, we

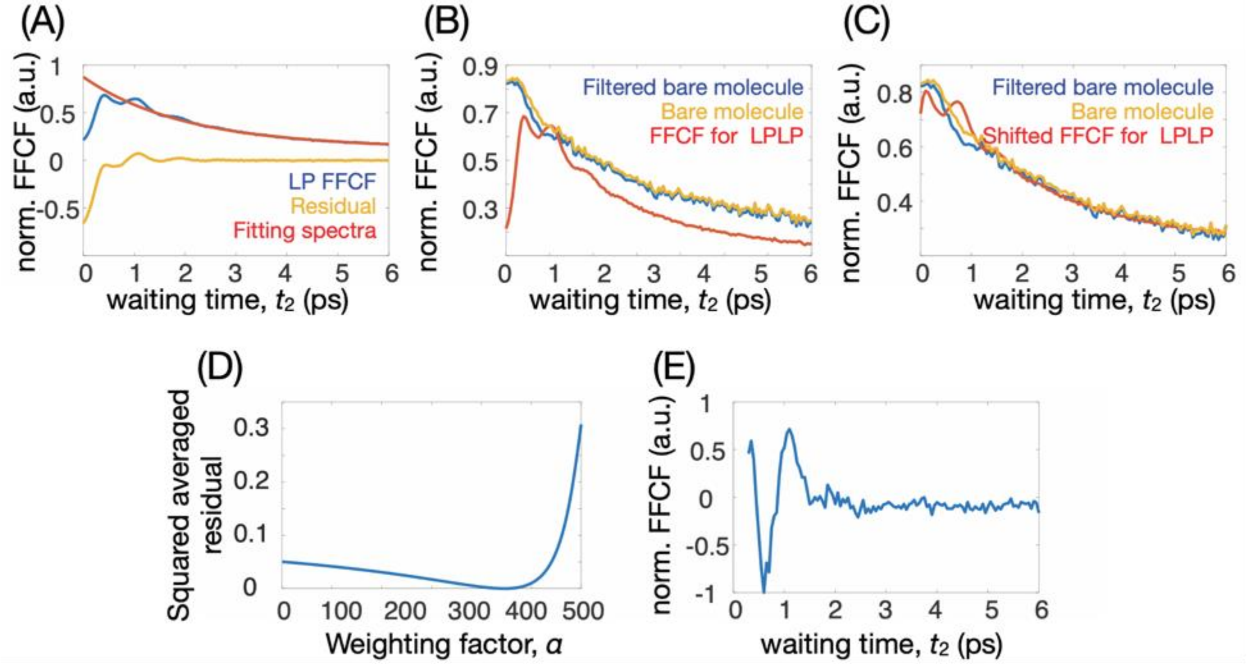

Figure 5-8. Using the FFCF of the LP to find the weighting parameter. (A) Waiting time dependence of the idealized FFCF of the LP band (yellow) obtained by subtracting the fitted molecule background (red) from normalized cavity LP normalized FFCF (blue). (B) $t_2 = 0$ comparison using the waiting time dependent FFCF from the filtered bare molecule (blue), bare molecule (yellow), and cavity LP (yellow). (C) Shifting the cavity FFCF forward by 300 fs and adding an offset of 0.12 to show that the LP FFCF is correctly timed. (D) Varying the weighting parameter gives a squared, average LP residual after 2 ps that reaches a minimum near 350 (arbitrary units). (E) The LP FFCF obtained by subtracting the weighted bare-molecule spectrum at each waiting time shows the elimination of spectral diffusion.

can construct the complex rephasing and nonrephasing signals. We choose the weighting factor with which we scale the bare molecule 2D-IR signal such that we eliminate the spectral diffusion signal in the residual polariton spectrum (most pronounced in the LPLP diagonal peak, see Fig. 2D of the main text). Due to the coherent oscillations that appear in the FFCF (expected for polaritons), we use the signal after 2 ps to set the weight parameter. Fig.1-7 shows that with an appropriate choice of the weight, we can remove the spectral diffusion and leave only the coherent oscillation caused by impulsive excitation of the two polariton bands. We show how the square of the residual (averaged from t_2 = 2 ps to t_2 = 6.7 ps) depends on the weight parameter. We choose the value that minimizes this squared difference from the expected value of zero. Due to slight differences in alignment between the cavity and non-cavity measurements, we find that we need to shift the t_2 of the cavity 300 fs to earlier time relative to the non-cavity measurements. The optimization process is summarized in **Fig.5-7**.

5.5.5 Coherence maps for ω_2 = –41 cm^{-1}

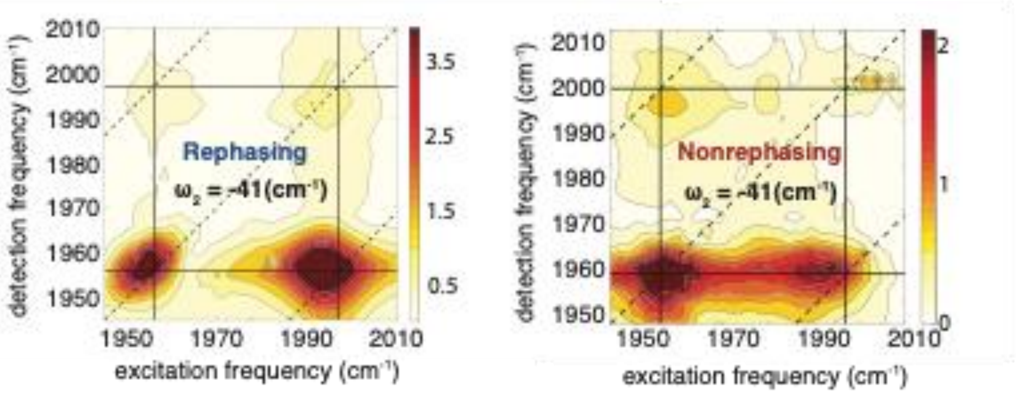

Figure 5-9.Coherence maps (absolute value amplitude) for the rephasing and nonrephasing signals at a coherence frequency of -41 cm^{-1}.

Using a 6 phase cycling scheme to collect the data, we can obtain both real and imaginary parts of the rephasing and nonrephasing spectra. As a result of Fourier transformation with respect to t_2, rephasing cross peaks with excitation frequency greater than the detection frequency will appear with negative coherence frequency. Likewise, the coherence located at the lower nonrephasing diagonal peak also appears with a negative frequency. Absolute value contour plots (**Fig. 1-8**) show the amplitude of the coherence maps.

5.5.6 Estimate of cavity lifetime

For a Fabry-Pérot resonator with loss arising from the mirror reflectivity, the cavity lifetime is given by:[58]

$$\tau_{cav} = T/(1 - R)$$

Where T is the roundtrip time and R is the reflectivity. For a 25 µm cavity, the round-trip time is 50 µm/((0.3 µm/fs)/1.3) = 216 fs (using an index of refraction of 1.3). Therefore the estimated cavity lifetime is 216/(1-0.92) = 2.7 ps.

5.5.7 Fitting results for several peaks in the 2D spectrum

We isolate the polariton spectrum by subtracting the filtered bare molecule 2D-IR response from the as-measured cavity response:

$$S_{Residual} = S_{cavity} - \alpha S_{filtered\ bare\ molecule}$$

Table 5-1. Table for fitting parameters. Waiting time dependent population dynamics of peaks A, D, E, and F (as labeled in Fig. 4) from the as-measured cavity, filtered bare molecule, and residual spectra.

	Measured cavity		**Bare molecule filtered**		**residual**	
peak	**τ_1(ps)**	**τ_2(ps)**	**τ_1(ps)**	**τ_2(ps)**	**τ_1(ps)**	**τ_2(ps)**
A	2.32±1.28	97.73±120.97	-	-	7.67±3.87	-
B	0.31±0.05	1.6±0.20	0.58±0.20	8.1±16.40	1.30±0.10	46.35±204.55
C	0.17±0.01	102.7±283.70	0.60±0.07	3.58±0.95	0.21±0.04	3.5±0.48
D	1.09±0.45	10.5±3.37	1.70±0.36	-	1.02±0.37	11.56±3.15

The waiting time dependence of peaks B, C and D are fit to the equation:

$$ae^{-\frac{t_2}{\tau_1}} + a_2 e^{-\frac{t_2}{\tau_2}} + c$$

In the as-measured cavity response, peak A is fit to a biexponential without a constant offset:

$$ae^{-\frac{t_2}{\tau_1}} + a_2 e^{-\frac{t_2}{\tau_2}}$$

The filtered bare molecule spectrum at peak F can be fit to a single exponential. The filtered bare molecule at peak A has too small amplitude to yield a fit. Error bars in the plots are the 95% confidence interval, and a considerable amount of the fitting error results from the coherent modulations of the peaks that inevitably arise from impulsive nonlinear spectroscopy of coupled transitions.

5.5.8 Calculation of molecule numbers in the cavity

We encapsulated a 40 mM solution inside 25 mm diameter cavity mirrors with a 25 µm spacer. This will give us a volume of 1.2×10^{-8} m^3, which is 1.2×10^{-5} L. With a concentration of 40 mmol/L, we have a total of 5×10^{-7} moles, or 3×10^{17} molecules.

Chapter 6 Investigation of the dynamics of dual modes polaritons probed with collinear geometry 2D-IR

6.1 Introduction

Controlling chemical reactions has always been a task that attracted most chemists. In Chapter 1, we have discussed the new development of using vibrational strong coupling (VSC) for both thermodynamically and selectively controlling the chemical reaction. Briefly, researchers were able to alter the ratio between two chemical reactions products by strongly coupling different reaction relevant vibrational modes with proper cavity mode. More results are showing that a specific chemical reaction's rate can be changed under VSC[9-14, 176-179]. The mechanism behind how VSC can control chemical reactions is unclear at this point[28, 65, 152, 180-183], but a similar strongly coupled system is well understood in the physics community and some major characters are discussed in Chapter 3. The major idea is by strongly coupled light and matter, these two separate systems interact with each other and form a new hybridized light and matter system namely polariton.

Usually, due to the small oscillator strength for individual vibrational modes, VSC requires a collective coupling with N vibrational modes and cavity at once. The coupling strength is proportional to the $\sqrt{N}$. And N-1 'dark state' or reservoir states which have the same frequency as the molecule's vibration mode along with two polariton states (LP and UP) are formed. If the dipole moments of all the molecule modes are aligned in the same direction, then the transition moment of the dark state is zero. And because of the spatial and orientational dependence coupling, because the molecule is usually dissolved in solution, it is nearly impossible to couple all the molecules inside the cavity and the dark reservoir state do not completely have zero dipole moment.

The polariton system adapted some of the important features of light, including having a small mass and dispersion relationship. To elaborate, in momentum space, there are two components $k_{//}$ and $k_{\perp}$ of the cavity's wave vector k. $k_{\perp}$ is determined by the length and the order of modes of the cavity. So, $k_{//}$ is usually a good quantum number to describe the energy dispersion of UP and LP. Since only molecule modes contribute to forming dark state, so the dark state energy remains constant with respect to changing of $k_{//}$.

Third order nonlinear spectroscopy has the benefit of directly accessing some of the important features of polariton that can potentially lead to help to understand the mechanism of VSC controlled chemical reaction; like population dynamics mechanisms, coupling between different modes, diffusion dynamics, and the energy ladder for higher excited states coupling. There are three commonly used phase matching geometries for multidimensional spectroscopy including 2D-IR, boxcars, pump-probe, and collinear. Commonly used pump-probe and boxcars geometry apparatus are only suitable to analyze zero detuning polariton system based on beams' geometry, for that reason, currently done 2D-IR polariton experiments are only focused on understanding zero detuning mostly at $k_{//}=0$ system[35, 37, 38, 75].

The polariton system is formed by vacuum Rabi oscillation; in another word, the molecular model is coupled with the cavity with no external light source required. That means all the $E(k_{//})$ simultaneously exist in one polariton system. So, the question about how other polariton modes inside the same system contribute to controlling chemical reaction therefore naturally rises. To better understand these questions, we will majorly investigate different parts of the polariton energy dispersion curve using an angle-dependent collinear geometry 2D-IR setup. Steve et al has done a collinear geometry 2D experiment but only looking at the energy laddering.[184] The system of choice is a methylcyclopentadienyl manganese tricarbonyl (MCMT) which has a high solubility in most organic solvents. The molecule has three vibrational active modes (two of them degenerate with each other) and zero Raman active mode in that region.

6.2 Experimental method

Collinear geometry apparatus (**Figure 6-1(A)(B)**) is converted from our pump-probe geometry set up which was detailed described in the previous chapters (Chapters 2, 4, and 5). A detailed discussion of collinear geometry setup has been published by Carlos and Tokmakoff[62]. In the collinear setup, the probe's polarization was changed by a 0-degree half wave plate (HWP). Two orthogonally polarized wire grid polarizers are implemented in the pump pathways to minimize pump leaking into the spectrometer; One of the polarizers (Thorlabs WP25H-C) was implemented right after the pulse shaper to selectively chose only the p polarized pump light. The grating pairs inside the pulse shaper have already preselected the pump pairs' polarization due to its high efficiency towards the p polarization beam. So, this polarizer is optional. Another polarizer (Thorlabs WP25H-C) is implemented right after the second parabolic mirror theoretically to only allow s polarization beams (probe and signal) to pass into the spectrometer. Because beam splitter (BS) is hard to find in the midIR (~5μm) region, another polarizer (Thorlabs WP25H-B) is used as polarization-dependent BS which transfers 59% of the s polarization probe beam and reflected 77% p polarization pump beam with the specific angle limited by the setup and all beams travels collinearly afterward. The beams are focused by a 10cm effective focal length parabolic mirror onto the sample position and a Thorlabs high precision micrometer controlled rotational stage is used to control the sample outside angle.

We use a 4 phase cycling scheme to remove scatter and unnecessary phase independent nonlinear signals. An additional chopper at the probe line helps to eliminate the pump leakage and pump and pump scatter which cannot be removed using phase cycling. The experiment pulse phase scheme can be found in chapter 3, table 2-2.

The sample is 0.12M of methylcyclopentadienyl manganese tricarbonyl (MCMT) dissolves in hexadecane and is placed within a 37μm Fabry Perot cavity made with average reflectivity of 95% of dielectric mirrors (**Figure 6-1 (C)**). Two sets of 2D experiments are done by changing the sample angle. Angle 1 is the normal incident with respect to the sample x-y plane and angle 2 is 7^o based on the reading of the rotating stage's micrometer (**Figure 6-1(C)**). Changing the beam incident angle is an equivalence of changing the sample angle in our case.

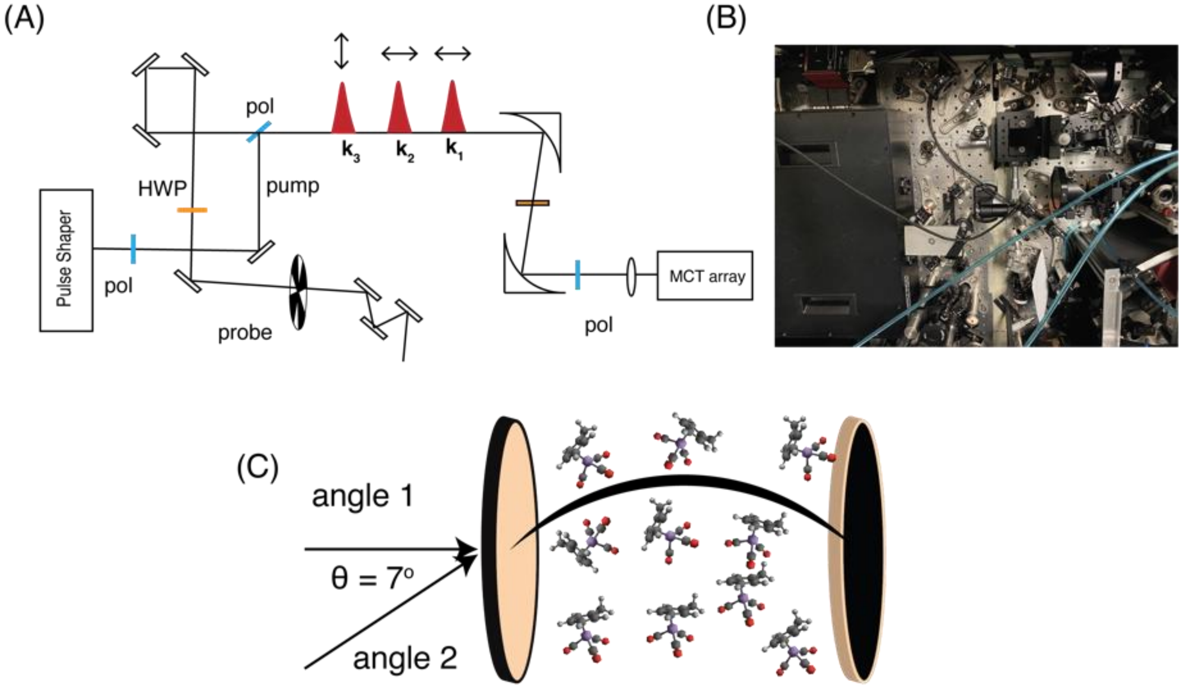

Figure 6-1. collinear geometry setup and angle dependent measurement. (A) diagrammed layout for the setup. (B) picture of the real setup (C) demonstration of angle dependent measurement

6.3 Vibrational assignment

Showed in FTIR (**Figure 6-2 (A)**), MCMT in hexadecane has two absorption peaks at 1941cm^{-1} and 2023 cm^{-1}. The linewidth is 8 cm^{-1} for both peaks. The lower frequency mode is a degenerate mode with the composition of the anti-symmetric stretch mode and out-of-phase symmetric stretch mode of the three carbonyls. This dual polariton system was labeled as two different polariton pairs based on frequency assignment, the lowest frequency polariton modes is polariton pair I (UP1and LP1) and the highest frequency modes pair named polariton pair II (UP2 and LP2). The frequency difference between the UP1 (1959 cm^{-1}) and LP1 (1920 cm^{-1}) is 39cm^{-1}, and the frequency difference is 23cm^{-1} for UP2(2034 cm^{-1}) and LP2 at angle 1(2011 cm^{-1}). The frequency difference between the UP1(1964 cm^{-1}) and LP1(1923 cm^{-1}) is 41cm^{-1}, and the frequency difference is 26cm^{-1} for UP2(2040 cm^{-1}) and LP2 (2014 cm^{-1}) at angle 2.

Transfer matrix way (chapter 3) is used to simulate both angle one and angle two linear spectra (**Figure 6-2 (A), (B)**), with the simulation we can identify that the free spectra rang

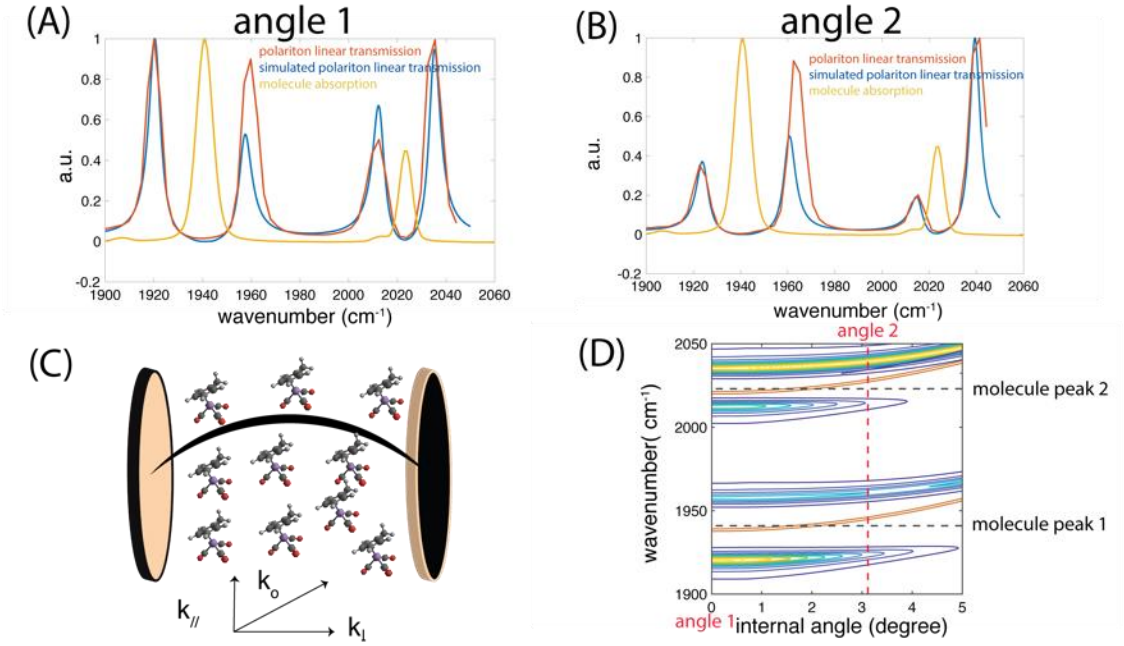

Figure 6-2. linear spectra, transfer matrix way of calculated dispersion curve and polariton demo. (A)(B)linear spectra at angle 1,2. red: probe transmission of the polariton; blue: polariton linear transmission spectrum calculated by using transfer matrix; (C) sample; (D) calculated dispersion curve using transfer matrix

(FSR) for angle one is 82.2cm^{-1} for angle 1 and 82.4cm^{-1} for angle 2. One thing to notice is this simplified transfer matrix way ignores the DBR property of the cavity mirror and uses the reflectivity which is determined by FTIR measurement. If we assume dissolving a little potion of MCMT (refractive index = 1.584) doesn't change the refractive index of hexadecane (1.4329), then the effective cavity length for angle one is 43.42 µm and for angle 2 is 43.36 µm. A dispersion spectrum of polariton and the cavity can also be simulated by scanning the incident angle of the beam (**Figure 6-1(C)**). The angle 2 by simulation is 3 degrees instead of 7 measured by a micrometer. The mismatching between the outside and inside angles is because of refraction.

The 2D spectra look like what we expected (**Figure 6-3**) for both angles. The cross-peaks shows up between every peak. One of the reasons is because the two molecule modes shared a

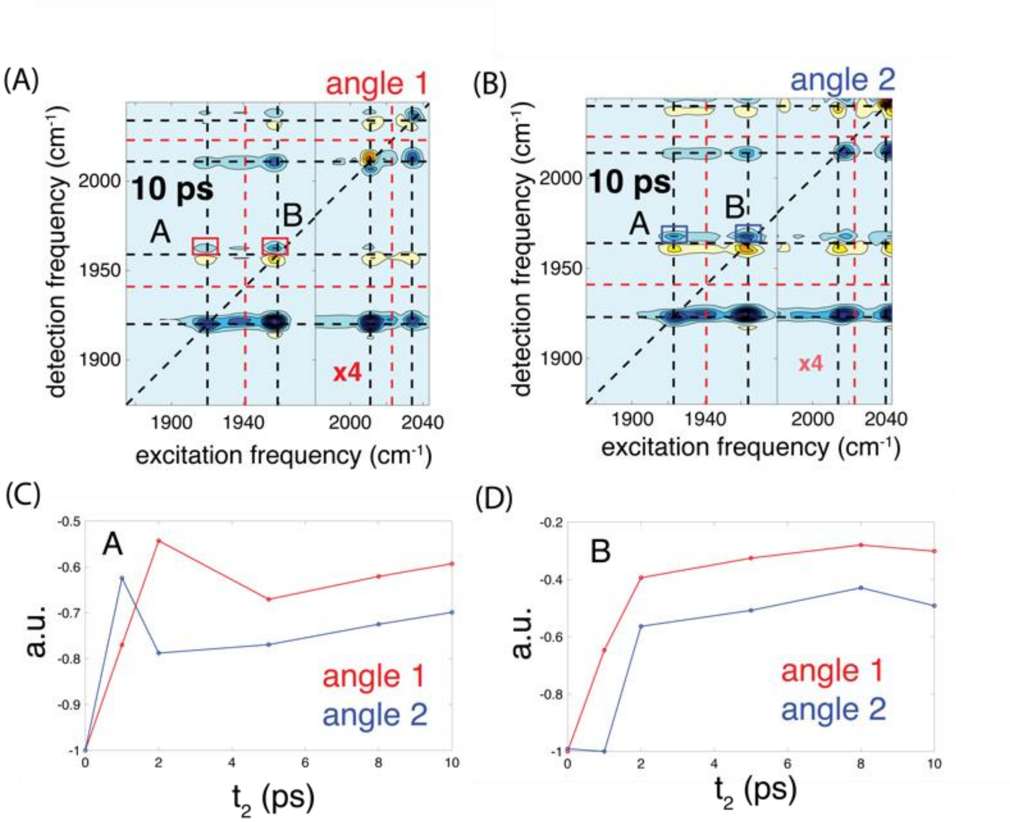

Figure 6-3. dynamic information for UP region of polariton 1. (A)2D spectrum of the polariton of angle 1 at 10ps (B) 2D spectrum of the polariton of angle 2 at 10ps (C)LP1UP1 cross peak dynamics. (D)UP1UP1 cross peak dynamics

common ground state so the polariton modes are too. However, this explanation is not as accurate, by using the simple Jaynes-Cumming model, we found out that even though most of the contribution for polariton comes from the cavity and molecule modes that have a similar frequency, the other cavity and molecule modes also contribute to form the same polariton. That means all the molecule modes and cavity modes are strongly coupled together to form this dual polariton system, so it is natural for the cross-peaks to rise. We were able to extract the energy ladder diagram for each of the angle (**Fig 6-4**).

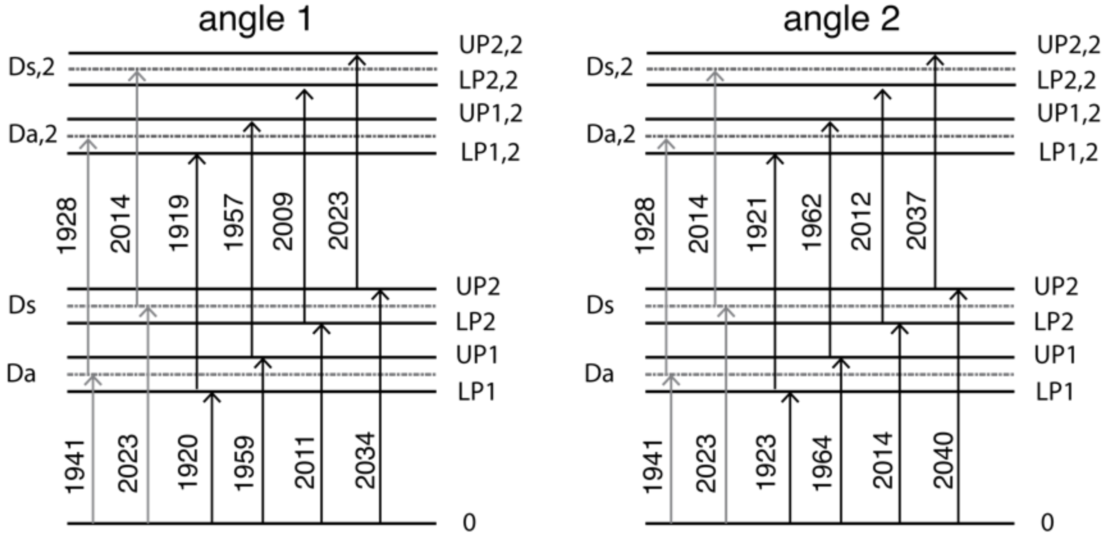

Figure 6-4. Energy ladder until the second manifold for angle 1(left) and angle 2(right). The grey line is for dark states.

The dynamic information is not so clear with the data shown here due to the limited time points (**Figure 6-3 (C), (D)).** But we expect to see different frequency oscillations on the top of population dynamics along with t_2 based on different intraband coherence between each polariton and molecule bands. Our hypothesis is that the coherence lifetime between two molecules stays the same as the bare molecule if no dark states contribute. And the coherence time for polariton should reflect the defection of the mirror. Naturally, a coherence map should help us to figure out the correlation. Relaxation dynamics, especially relaxation mediated by a dark state should change respect with $k_{//}$. Those are the information we will be looking for if we take a new set of data with more time points.

6.4 Conclusion

In this chapter we talked about using collinear geometry 2D-IR setup to investigate two different parts of the energy dispersion curve, $E(k_{//})$ by selecting the incident angle of the beams. Using a simple Jaynes-Cumming model, we were able to explain the cross peaks in a single 2D spectrum for both angles. The next step is to take more data points at an earlier time to find out the energy transfer dynamics for dual modes polariton

Chapter 7 Conclusion and Outlook

7.1 General conclusion and outlook

This dissertation first reviewed the recent developments, current complications, and open challenges of using vibrational strong coupling to control chemical reactions and dynamics. By using both FTIR and 2D-IR along with simulations, we were able to help solve some of current problems and learn more about the unique features of vibrational polaritons, including spatially inhomogeneous coupling. Using robust model systems $W(CO)_6$ and MCMT it was possible to demonstrate that both geometric and amplitude methods to extract the frequency-frequency correlation function (FFCF) are feasible and yield essentially identical dynamics for most of molecules. This finding established the groundwork for using the amplitude method to investigate spectral diffusion in a polaritonic system. By using the combination of the fact that polariton transitions are immune to inhomogeneous broadening, and the reliability of the amplitude-based FFCF extraction method, we are able to isolate the polariton 2D-IR spectrum. This approach reveals the polariton energy ladder, which is an essential first step in characterizing vibrational structure and polariton dynamics. Lastly, extension to the collinear geometry enables access to different polariton hybridization within the energy dispersion curve, with preliminary hints that the dynamics depend on the degree of hybridization.

Within chemistry, the polariton field is still in its infancy, and it is fortunate that we can adopt some of the basic theory from solid state microcavity polaritonics. Nevertheless, there are still some of the problems we have to face when study molecular vibrational polaritons. Even though we have demonstrated a simple way for doing the background correction, but it is not general enough. For example, it is not that useful for the system that has no appreciable spectral diffusion. So, it is better if we can avoid the background correction altogether. One of the ways to suppress the background is to increase the coupling strength, aiming for a larger Rabi splitting, so that the overlap between bare molecule and polariton peak pairs will decrease. Both increasing the concentration and increasing the reflectivity of the cavity mirrors can help, but for most cases it is not easy to increase the concentration due to limited solubility. So, increasing the mirror's reflectivity, and hence the cavity's Q-factor, is a likely path forward. There is a drawback, however, because high reflectivity mirrors would make transmission measurements impractical. Reflection measurements can be implemented but one must solve the complication caused by the interference between the directly reflected probe (from the first mirror) and the probe that traveled along with the signal inside cavity.

Theoretically speaking, the coupling should only be based on the frequency of vibrational modes not on the specific species involved. In order to understand the collective coupling nature of polaritons, one could potentially choose to couple with the solvent which has a mode shared the frequency with the reactant and study how this will change the dynamics of the reaction relevant peaks by using 2D-IR. Examples of this effect have been reported in the context of chemical reaction modification[14], but not yet in the domain of ultrafast dynamics. This work is indeed ongoing in our lab.

There are many more things one can investigate that have both fundamental and applied aspects. For example, including spatially resolved measurements could help us to better understand polariton's delocalization and long-range energy transfer. Spatial organization is an essential design principle in biology, but it remains elusive in most chemistry. By coupling optical cavities of extended and potentially arbitrary cavity architectures, polaritonics has the potential to establish spatially-controlled chemical reactivity and dynamics. It could be particularly interesting to use a three-dimensional rectangular waveguide, for example, instead of two-dimensional mirrors as the optical cavity. By having three different cavity modes could help to utilize the orientational dependent coupling nature and to have different products and reaction rates along each dimension.

Bibliography

[1] N. G. Basov, A. N. Oraevsky, and A. V. Pankratov, in *Chemical and Biochemical Applications of Lasers*, edited by C. B. Moore (Academic Press, 1974), pp. 203.

[2] N. Bloembergen, and A. H. Zewail, The Journal of Physical Chemistry **88** (1984) 5459.

[3] in *Quantum Control of Molecular Processes*2011), pp. 83.

[4] D. J. Tannor, R. Kosloff, and S. A. Rice, The Journal of Chemical Physics **85** (1986) 5805.

[5] M. Shapiro, and P. Brumer, The Journal of Chemical Physics **98** (1993) 201.

[6] D. J. Tannor, and S. A. Rice, The Journal of Chemical Physics **83** (1985) 5013.

[7] A. K. Tiwari, D. Dey, and N. E. Henriksen, Physical Review A **89** (2014) 023417.

[8] A. Assion *et al.*, Science **282** (1998) 919.

[9] F. J. Garcia-Vidal, C. Ciuti, and T. W. Ebbesen, Science **373** (2021)

[10] J. Lather *et al.*, Angew Chem Int Ed Engl **58** (2019) 10635.

[11] E. Lorchat *et al.*, ACS Photonics **5** (2018) 5047.

[12] D. Okada *et al.*, Nano Lett **18** (2018) 4396.

[13] A. Thomas *et al.*, Nanophotonics **9** (2020) 249.

[14] A. Thomas *et al.*, Science **363** (2019) 615.

[15] R. P. Feynman, F. L. Vernon, and R. W. Hellwarth, Journal of Applied Physics **28** (1957) 49.

[16] M. Gross *et al.*, Physical Review Letters **43** (1979) 343.

[17] in *Semiconductor Cavity Quantum Electrodynamics* (Springer Berlin Heidelberg, Berlin, Heidelberg, 2000), pp. 25.

[18] H. Deng, H. Haug, and Y. Yamamoto, Reviews of Modern Physics **82** (2010) 1489.

[19] B. Zhang *et al.*, Light: Science & Applications **3** (2014) e135.

[20] S. Hiura H, A., ChemRxiv (2021)

[21] A. Sau *et al.*, Angewandte Chemie International Edition **60** (2021) 5712.

[22] R. M. A. Vergauwe *et al.*, Angewandte Chemie International Edition **58** (2019) 15324.

[23] B. Munkhbat *et al.*, Science Advances **4** (2018) eaas9552.

[24] J. Galego, F. J. Garcia-Vidal, and J. Feist, Nat Commun **7** (2016) 13841.

[25] M. V. Imperatore, J. B. Asbury, and N. C. Giebink, J Chem Phys **154** (2021) 191103.

[26] G. D. Wiesehan, and W. Xiong, The Journal of Chemical Physics **155** (2021) 241103.

[27] J. Galego *et al.*, Physical Review X **9** (2019) 021057.

[28] J. A. Campos-Gonzalez-Angulo, and J. Yuen-Zhou, The Journal of Chemical Physics **152** (2020) 161101.

[29] J. d. Pino, J. Feist, and F. J. Garcia-Vidal, New Journal of Physics **17** (2015) 053040.

[30] M. Du, and J. Yuen-Zhou, Physical Review Letters **128** (2022) 096001.

[31] A. D. Bristow *et al.*, J Phys Chem B **115** (2011) 5365.

[32] T. Byrnes, N. Y. Kim, and Y. Yamamoto, Nature Physics **10** (2014) 803.

[33] J. Flick *et al.*, Proc Natl Acad Sci U S A **114** (2017) 3026.

[34] J. O. Tollerud, C. R. Hall, and J. A. Davis, Opt Express **22** (2014) 6719.

[35] B. Xiang *et al.*, J Phys Chem A **123** (2019) 5918.

[36] A. D. Dunkelberger *et al.*, Nature Communications **7** (2016) 13504.

[37] B. Xiang *et al.*, Science Advances **5** (2019) eaax5196.

[38] A. B. Grafton *et al.*, Nature Communications **12** (2021) 214.

[39] T. B. Norris *et al.*, Physical Review B **50** (1994) 14663.

[40] D. M. Jonas, Annu Rev Phys Chem **54** (2003) 425.

[41] S. Mukamel, *Principles of nonlinear optical spectroscopy* (Oxford University Press , New York, 1995), Oxford series in optical and imaging sciences ; 6,

[42] J. P. Ogilvie, and K. J. Kubarych, in *Advances In Atomic, Molecular, and Optical Physics* (Academic Press, 2009), pp. 249.

[43] R. W. Boyd, in *Nonlinear Optics (Third Edition)*, edited by R. W. Boyd (Academic Press, Burlington, 2008), pp. 277.

[44] M. Khalil, N. Demirdöven, and A. Tokmakoff, The Journal of Physical Chemistry A **107** (2003) 5258.

[45] P. Hamm, and M. Zanni, *Concepts and Methods of 2D Infrared Spectroscopy* (Cambridge University Press, Cambridge, 2011),

[46] R. W. Boyd, in *Nonlinear Optics (Third Edition)*, edited by R. W. Boyd (Academic Press, Burlington, 2008), pp. 1.

[47] E. E. Fenn, and M. D. Fayer, J Chem Phys **135** (2011) 074502.

[48] P. L. Kramer *et al.*, J Chem Phys **142** (2015) 184505.

[49] K. Kwak *et al.*, J Chem Phys **127** (2007) 124503.

[50] K. Kwak, D. E. Rosenfeld, and M. D. Fayer, J Chem Phys **128** (2008) 204505.

[51] S. M. Gallagher Faeder, and D. M. Jonas, The Journal of Physical Chemistry A **103** (1999) 10489.

[52] S. T. Roberts, J. J. Loparo, and A. Tokmakoff, J. Chem. Phys. **125** (2006) 084502.

[53] K. C. Robben, and C. M. Cheatum, The Journal of Physical Chemistry B **125** (2021) 12876.

[54] Y. Song *et al.*, The Journal of Chemical Physics **142** (2015) 212410.

[55] D. Paleček *et al.*, Science Advances **3** (2017) e1603141.

[56] S. S. Senlik, V. R. Policht, and J. P. Ogilvie, The Journal of Physical Chemistry Letters **6** (2015) 2413.

[57] Y. Song *et al.*, Rev Sci Instrum **90** (2019) 013108.

[58] A. Weiner, S. De Silvestri, and E. Ippen, J. Opt. Soc. Am. B-Opt. Phys. **2** (1985) 654.

[59] in *Ultrafast Optics*2009), pp. 85.

[60] P. Y. Amnon Yariv, *Optical Waves in Crystals: Propagation and Control of Laser Radiation* 2002),

[61] J. A. Myers *et al.*, Opt. Express **16** (2008) 17420.

[62] C. R. Baiz, D. Schach, and A. Tokmakoff, Opt. Express **22** (2014) 18724.

[63] in *Semiconductor Optics* (Springer Berlin Heidelberg, Berlin, Heidelberg, 2005), pp. 91.

[64] T. B. Norris, in *Confined Electrons and Photons: New Physics and Applications*, edited by E. Burstein, and C. Weisbuch (Springer US, Boston, MA, 1995), pp. 503.

[65] F. Herrera, and J. Owrutsky, J Chem Phys **152** (2020) 100902.

[66] E. M. Purcell, H. C. Torrey, and R. V. Pound, Physical Review **69** (1946) 37.

[67] R. B. Balili, International Journal of Modern Physics: Conference Series **17** (2012) 159.

[68] H. Yokoyama, Y. Nambu, and T. Kawakami, in *Confined Electrons and Photons: New Physics and Applications*, edited by E. Burstein, and C. Weisbuch (Springer US, Boston, MA, 1995), pp. 427.

[69] E. T. Jaynes, and F. W. Cummings, Proceedings of the IEEE **51** (1963) 89.

[70] M. Tavis, and F. W. Cummings, Physical Review **188** (1969) 692.

[71] R. Houdré, R. P. Stanley, and M. Ilegems, Physical Review A **53** (1996) 2711.

[72] J. M. Manceau *et al.*, Physical Review B **96** (2017) 235301.

[73] I. Diniz *et al.*, Physical Review A **84** (2011) 063810.

[74] S. Pau *et al.*, Solid State Communications **98** (1996) 781.

[75] W. Ahn *et al.*, ACS Photonics **5** (2018) 158.

[76] N. F. Ramsey, Physical Review **78** (1950) 695.

[77] C. H. Brito Cruz *et al.*, Chemical Physics Letters **132** (1986) 341.

[78] W. P. de Boeij, M. S. Pshenichnikov, and D. A. Wiersma, Chemical Physics **233** (1998) 287.

[79] M. Cho *et al.*, The Journal of Physical Chemistry **100** (1996) 11944.

[80] Y. Tanimura, and S. Mukamel, J. Chem. Phys. **99** (1993) 9496.

[81] M. Cho, *Two-Dimensional Optical Spectroscopy* (CRC Press, Boca Raton, 2009),

[82] J. Hybl, Y. Christophe, and D. Jonas, Chem. Phys. **266** (2001) 295.

[83] J. Hybl *et al.*, Chem. Phys. Lett. **297** (1998) 307.

[84] R. Kubo, *A Stochastic Theory of Line Shape* (John Wiley& Sons Inc., 1969), Vol. XV, Adv. Chem. Phys., 101-127.

[85] F. Bloch, Phys. Rev. **70** (1946) 460.

[86] A. G. Redfield, Adv. Magn. Opt. Reson. **1** (1965) 1.

[87] R. Loring, and S. Mukamel, J. Chem. Phys. **83** (1985) 2116.

[88] K. Lazonder, M. Pshenichnikov, and D. Wiersma, Opt. Lett. **31** (2006) 3354.

[89] D. Jonas, Annu. Rev. Phys. Chem. **54** (2003) 425.

[90] K. Okumura, A. Tokmakoff, and Y. Tanimura, Chem. Phys. Lett. **314** (1999) 488.

[91] K. Kwak, D. Rosenfeld, and M. Fayer, J. Chem. Phys. **128** (2008) 204505.

[92] K. Kwak *et al.*, J. Chem. Phys. **127** (2007) 124503.

[93] S. K. Karthick Kumar, A. Tamimi, and M. D. Fayer, J Chem Phys **137** (2012) 184201.

[94] S. Woutersen *et al.*, The Journal of Chemical Physics **117** (2002) 6833.

[95] M. Cowan *et al.*, Nature **434** (2005) 199.

[96] E. Hahn, Phys. Rev. **80** (1950) 580.

[97] K. R. Daley, and K. J. Kubarych, J Phys Chem B **121** (2017) 10574.

[98] D. G. Osborne *et al.*, J. Phys. Chem. B **117** (2013) 15407.

[99] J. T. King *et al.*, J. Phys. Chem. B **116** (2012) 5604.

[100] J. T. King, and K. J. Kubarych, J. Am. Chem. Soc. **134** (2012) 18705.

[101] J. T. King, M. R. Ross, and K. J. Kubarych, J. Phys. Chem. B **116** (2012) 3754.

[102] J. T. King, M. R. Ross, and K. J. Kubarych, Phys Rev Lett **108** (2012) 157401.

[103] L. M. Kiefer, and K. J. Kubarych, Coord. Chem. Rev. **372** (2018) 153.

[104] L. M. Kiefer, and K. J. Kubarych, Chem. Sci. **9** (2018) 1527.

[105] T. Mančal *et al.*, J. Chem. Phys. **132** (2010) 184515.

[106] D. G. Osborne, and K. J. Kubarych, J. Phys. Chem. A **117** (2013) 5891.

[107] I. A. Nilsen *et al.*, J. Chem. Phys. **141**, 134313 (2014)

[108] J. A. Dunbar *et al.*, J. Phys. Chem. B **119** (2015) 6271.

[109] N. Belabas, and D. Jonas, J. Opt. Soc. Am. B **22** (2005) 655.

[110] M. Yetzbacher *et al.*, J. Chem. Phys. **126** (2007) 044511.

[111] B. Cho *et al.*, J. Phys. Chem. A **113** (2009) 13287.

[112] B. Xiang *et al.*, Proc. Natl. Acad. Sci. U. S. A. **115** (2018) 4845.

[113] B. Xiang *et al.*, Science Advances **5**, aax5196 (2019)

[114] B. Xiang *et al.*, Science **368** (2020) 665.

[115] Z. M. Yang, B. Xiang, and W. Xiong, ACS Photonics **7** (2020) 919.

[116] B. Xiang *et al.*, J. Phys. Chem. A **123** (2019) 5918.

[117] P. Tekavec *et al.*, Opt. Lett. **34** (2009) 1390.

[118] S. H. Shim, and M. T. Zanni, Phys Chem Chem Phys **11** (2009) 748.

[119] H. S. Tan, J. Chem. Phys. **129**, 124501 (2008)

[120] D. L. Lichtenberger, and G. E. Kellogg, J. Am. Chem. Soc. **108** (1986) 2560.

[121] S. Shim *et al.*, Proc. Natl. Acad. Sci. U. S. A. **104** (2007) 14197.

[122] M. Khalil, N. Demirdoven, and A. Tokmakoff, J. Phys. Chem. A **107** (2003) 5258.

[123] J. T. King, C. R. Baiz, and K. J. Kubarych, J. Phys. Chem. A **114** (2010) 10590.

[124] J. T. King, J. M. Anna, and K. J. Kubarych, Phys. Chem. Chem. Phys. **13** (2011) 5579.

[125] O. Golonzka *et al.*, J. Chem. Phys. **115** (2001) 10814.

[126] A. A. Low, and M. B. Hall, Int. J. Quantum Chem. **77** (2000) 152.

[127] P. J. Fitzpatrick *et al.*, Inorg. Chem. **20** (1981) 2852.

[128] T. A. Albright, P. Hofmann, and R. Hoffmann, J. Am. Chem. Soc. **99** (1977) 7546.

[129] P. Portius *et al.*, Organometallics **38** (2019) 4288.

[130] P. A. Eckert, and K. J. Kubarych, The Journal of Chemical Physics **151** (2019) 054307.

[131] P. Hamm, and M. T. Zanni, *Concepts and Methods of 2D Infrared Spectroscopy* (Cambridge University Press, New York, 2011),

[132] H. Deng *et al.*, Science **298** (2002) 199.

[133] S. Kéna-Cohen, and S. R. Forrest, Nature Photonics **4** (2010) 371.

[134] Y. B. Sun *et al.*, Nat. Phys. **13** (2017) 870.

[135] J. A. Hutchison *et al.*, Angew. Chem.-Int. Edit. **51** (2012) 1592.

[136] A. Thomas *et al.*, Angew. Chem.-Int. Edit. **55** (2016) 11462.

[137] Y. T. Pang *et al.*, Angew. Chem.-Int. Edit. **59** (2020) 10436.

[138] R. M. A. Vergauwe *et al.*, Angew. Chem.-Int. Edit. **58** (2019) 15324.

[139] J. Lather, and J. George, J. Phys. Chem. Lett. **12** (2021) 379.

[140] A. D. Dunkelberger *et al.*, Nat. Commun. **7**, 13504 (2016) 13504.

[141] A. D. Dunkelberger *et al.*, J. Phys. Chem. A **122** (2018) 965.

[142] A. D. Dunkelberger *et al.*, ACS Photonics **6** (2019) 2719.

[143] B. Xiang *et al.*, J. Phys. Chem. A **123** (2019) 5918.

[144] B. Xiang *et al.*, Science Advances **5**, aax5196 (2019) eaax5196.

[145] B. Xiang *et al.*, Science **368** (2020) 665.

[146] B. Xiang *et al.*, Science Advances **7**, eabf6397 (2021) eabf6397.

[147] B. Xiang, and W. Xiong, J. Chem. Phys. **155**, 050901 (2021) 050901.

[148] A. Shalabney *et al.*, Nat. Commun. **6**, 5981 (2015) 5981.

[149] L. A. Martinez-Martinez *et al.*, ACS Photonics **5** (2018) 167.

[150] R. F. Ribeiro *et al.*, Chem. Sci. **9** (2018) 6325.

[151] J. A. Campos-Gonzalez-Angulo, R. F. Ribeiro, and J. Yuen-Zhou, Nat. Commun. **10**, 4685 (2019) 4685.

[152] M. Du, R. F. Ribeiro, and J. Yuen-Zhou, Chem **5** (2019) 1167.

[153] J. Yuen-Zhou, and V. M. Menon, Proc. Natl. Acad. Sci. U. S. A. **116** (2019) 5214.

[154] M. R. Wasielewski *et al.*, Nat. Rev. Chem. **4** (2020) 490.

[155] T. E. Li, A. Nitzan, and J. E. Subotnik, J. Chem. Phys. **152** (2020) 234107.

[156] T. E. Li, J. E. Subotnik, and A. Nitzan, Proc. Natl. Acad. Sci. U. S. A. **117** (2020) 18324.

[157] T. E. Li, A. Nitzan, and J. E. Subotnik, J. Chem. Phys. **154**, 094124 (2021) 094124.

[158] X. Y. Li, A. Mandal, and P. F. Huo, Nat. Commun. **12**, 1315 (2021) 1315.

[159] D. Sidler *et al.*, J. Phys. Chem. Lett. **11** (2020) 7525.

[160] A. G. Avramenko, and A. S. Rury, J. Phys. Chem. Lett. **11** (2020) 1013.

[161] E. T. Jaynes, and F. W. Cummings, Proceedings of the Ieee **51** (1963) 89.

[162] M. Tavis, and F. W. Cummings, Phys. Rev. **188** (1969) 692.

[163] I. Vurgaftman *et al.*, J. Phys. Chem. Lett. **11** (2020) 3557.

[164] F. Herrera, and F. C. Spano, Phys. Rev. A **95**, 053867 (2017) 053867.

[165] V. F. Crum, S. R. Casey, and J. R. Sparks, Phys. Chem. Chem. Phys. **20** (2018) 850.

[166] A. B. Grafton *et al.*, Nat. Commun. **12**, 214 (2021) 214.

[167] J. F. Brookes *et al.*, J. Phys. Chem. A **117** (2013) 6234.

[168] F. Hernandez, and F. Herrera, J. Chem. Phys. **151** (2019) 144116.

[169] R. Duan *et al.*, J. Chem. Phys. **154**, 174202 (2021) 174202.

[170] M. J. Nee *et al.*, J. Chem. Phys. **129**, 084503 (2008) 084503.

[171] C. A. DelPo *et al.*, J. Phys. Chem. Lett. **11** (2020) 2667.

[172] S. X. Yan, and H. S. Tan, Chem. Phys. **360** (2009) 110.

[173] F. D. Fuller *et al.*, Nat. Chem. **6** (2014) 706.

[174] R. Chikkaraddy *et al.*, Nature **535** (2016) 127.

[175] B. Cohn *et al.*, J. Phys. Chem. Lett. **12** (2021) 7060.

[176] T. Chervy *et al.*, ACS Photonics **5** (2017) 217.

[177] J. George *et al.*, Phys Rev Lett **117** (2016) 153601.

[178] D. Hagenmüller *et al.*, ACS Photonics **6** (2019) 1073.

[179] M. Seidel *et al.*, ACS Photonics **6** (2019) 1823.

[180] J. A. Campos-Gonzalez-Angulo, R. F. Ribeiro, and J. Yuen-Zhou, Nat Commun **10** (2019) 4685.

[181] S. Kéna-Cohen, and J. Yuen-Zhou, ACS Central Science **5** (2019) 386.

[182] X. Li, A. Mandal, and P. Huo, Nat Commun **12** (2021) 1315.

[183] F. C. Spano, J Chem Phys **142** (2015) 184707.

[184] T. M. Autry *et al.*, Phys Rev Lett **125** (2020) 067403.